HIGH-RESOLUTION GRAIN-SIZE DISTRIBUTIONS: INSIGHT INTO TEPHRA DISPERSAL AND SEDIMENTATION DURING PLINIAN ERUPTIONS

by

JOSHUA WIEJACZKA

A DISSERTATION

Presented to the Department of Earth Sciences
and the Division of Graduate Studies of the University of Oregon
in partial fulfillment of the requirements
for the degree of
Doctor of Philosophy

September 2023

DISSERTATION APPROVAL PAGE

Student: Joshua Wiejaczka

Title: High-Resolution Grain-Size Distributions: Insight into Tephra Dispersal and Sedimentation during Plinian Eruptions

This dissertation has been accepted and approved in partial fulfillment of the requirements for the Doctor of Philosophy degree in the Department of Earth Sciences by:

Prof. Thomas Giachetti	Chairperson and Advisor
Prof. James Watkins	Core Member
Prof. Josef Dufek	Core Member
Dr. Larry Mastin	Core Member
Prof. Eric Corwin	Institutional Representative

and

Krista Chronister	Vice Provost for Graduate Studies

Original approval signatures are on file with the University of Oregon Division of Graduate Studies.

Degree awarded September 2023

© 2023 Joshua Wiejaczka
This work is licensed under a Creative Commons
Attribution (United States) License.

DISSERTATION ABSTRACT

Joshua Wiejaczka

Doctor of Philosophy

Department of Earth Sciences

September 2023

Title: High-Resolution Grain-Size Distributions: Insight into Tephra Dispersal and Sedimentation during Plinian Eruptions

Detailed field studies of past eruptions contribute to constraining the input parameters used to forecast tephra dispersion and mitigate potentially fatal volcanic hazards. It is thus of the utmost importance to understand the relationships between the characteristics of tephra deposits and these input Eruption Source Parameters (ESPs). In this dissertation, I determine the ESPs for the ~7.7 ka Cleetwood eruption of Mount Mazama (Crater Lake/giiwas, Oregon, USA). This eruption is an important historic eruption because it immediately preceded the climactic caldera-forming eruption, at the same location, and is similar to the only observed silicic volcanic eruptions that have transitioned from explosive to effusive activity (2008 Chaitén and 2011-2012 Cordón Caulle, [Chile]). The Cleetwood eruptive sequence consisted of two consecutive VEI 4 eruptions: the main lower Cleetwood unit and smaller upper Cleetwood units, in order from oldest to youngest. The lower Cleetwood phase alone, produced a ~14.4 km plume and emplaced ~0.85 km^3 of tephra. Altogether, the explosive phase of the Cleetwood eruption deposited ~1.1 km^3 (non-DRE) of material and transitioned to an effusive stage that emplaced a ~0.6 km^3 rhyodacitic lava flow. Furthermore, I develop a novel approach which combines laser diffraction and dynamic image analysis to produce a continuous set of high-resolution grain-size distributions (HR-GSDs) for samples spanning a range of sizes of ejected tephra from less than a micron to a few centimeters. Through this approach, I show the ability for these HR-GSDs to provide insights into magma fragmentation and tephra transport. Next, through detailed wind analysis and the use of these ESPs as the inputs for Tephra2, a volcanic ash transport and dispersal model, I estimate the geometry and dimensions of the volcanic plume that emplaced the lower Cleetwood unit. Here, I show the standard version of Tephra2, which uses a vertical line source, does well to reproduce mass loads and grain-size distributions separately but fails to fit

both simultaneously with a single set of empirical inputs. To overcome this, I adapt Tephra2 outputs to simulate deposition via an umbrella cloud. Applying this adaptation and a grid search approach over reasonable plume heights and umbrella cloud geometries gives the best results for a plume with a 4x40 km^2 elliptical geometry. This approach improves overall GSDs without degrading mass loads. Lastly, I combine detailed componentry and HR-GSDs on samples I collected from the products of hybrid phase of the 2011-2012 eruption at Cordón Caulle. This analysis suggests that ash sintering after fragmentation produced a dense plug that obstructed the shallow conduit. This caused the system to re-pressurize and subsequently shatter pieces of the plug during the next explosive event. This pattern continued until permeable outgassing dominated over re-pressurization, facilitating the transition to a solely effusive stage.

CURRICULUM VITAE

NAME OF AUTHOR: Joshua Wiejaczka

GRADUATE AND UNDERGRADUATE SCHOOLS ATTENDED:

University of Oregon, Eugene, Oregon, USA
SUNY New Paltz, New Paltz, New York, USA
CUNY Hunter College, New York, New York, USA
SUNY Ulster, Stone Ridge, New York, USA

DEGREES AWARDED:

Doctor of Philosophy, Earth Sciences, 2023, University of Oregon
Bachelor of Science, Geology, 2016, SUNY New Paltz
Bachelor of Arts, Music, CUNY Hunter College
Associate of Arts, SUNY Ulster

AREAS OF SPECIAL INTEREST:

Volcanology
Data Science

PROFESSIONAL EXPERIENCE:

Graduate Research Assistant, University of Oregon, 2017-2023

Undergraduate Research Assistant, SUNY New Paltz, 2012-2013

GRANTS, AWARDS, AND HONORS:

Smith Scholarship, University of Oregon, 2022

Smith Scholarship, University of Oregon, 2021

Weiser Scholarship, University of Oregon, 2020

Jack Kleinman Grant for Volcano Research, Community Foundation for SW WA, 2020

Jay McMurray Scholarship, University of Oregon, 2019

Summer Research Fellowship, University of Oregon, 2018

Outstanding Graduate Honors, SUNY New Paltz, 2016

PUBLICATIONS:

Wiejaczka, J., & Giachetti, T. (2022). Using Eruption Source Parameters and High-Resolution Grain-Size Distributions of the 7.7 ka Cleetwood Eruption of Mount Mazama (Oregon, United States) to Reveal Primary and Secondary Eruptive Processes. Frontiers in Earth Science, 460. https://doi.org/10.3389/feart.2022.853021

Giachetti, T., Trafton, K. R., **Wiejaczka, J.**, Gardner, J. E., Watkins, J. M., Shea, T., et al. (2021). The Products of Primary Magma Fragmentation Finally Revealed by Pumice Agglomerates. Geology 49 (11), 1307–1311. doi:10.1130/G48902.1

ACKNOWLEDGMENTS

I wish to express sincere appreciation to T. Giachetti, J.M. Watkins, J. Dufek, L.G. Mastin, K.V. Cashman, T. Shea, C.R. Bacon, S.R. Young, and J.E. Gardner for their insights, feedback, and guidance throughout the duration of this research. I thank C. McDermott for her time as our archeological and wildfire monitor while working in the Fremont-Winema National Forest. In addition, special thanks are due to my coauthors and collaborators, namely P. Ruprecht, H. Winslow, D. Lobos, and P.R. Phelps for their hard work on Cordón Caulle. Thanks to A.R. Van Eaton and H.M.N. Wright for their help during laser diffraction analysis at the Cascades Volcano Observatory. Thanks to the University of Oregon 2022 field camp for all of their help on excavating the MEGA PIT. I'm also thankful for the friends I met here at the University of Oregon, especially T. Newton, B. McVey, C. Obeidy, K. Gardner, M. Koeneke, A. Broz, M. Cascante, M. Hudak, and D. Zakharov.

This work was supported in part by the National Science Foundation grant EAR-1725207, the Jack Kleinman Memorial Fund for Volcano Research, and scholarships from the Department of Earth Science at the University of Oregon.

DEDICATION

“Yeah, this thesis is dedicated
To all the teachers that told me I'd never amount to nothin'
To all the people that lived above the buildings that I was hustlin' in front of
Called the police on me when I was just tryin' to make some money to feed my doggo
And all the students in the struggle
You know what I'm sayin'?
It's all good, baby baby”

TABLE OF CONTENTS

LIST OF FIGURES

Figure Page

Chapter II

Chapter III

Figure Page

Chapter IV

LIST OF TABLES

Table Page

Chapter II

Chapter III

Chapter IV

CHAPTER I

INTRODUCTION

Tephra fallout during volcanic eruptions poses a wide spectrum of hazards that can have significant impacts on human health, infrastructure, and the environment. The accuracy of volcanic ash transport and dispersal models to forecast tephra accumulation to downwind communities largely depends on the input eruption source parameters such as the erupted mass, the geometry and dimensions of the volcanic plume, and the size and density distribution of the ejected granular material. These parameters are challenging to constrain in real time and often rely on data obtained from detailed field studies of analogous historic eruptions. It is thus paramount to understand the relationships between eruption source parameters and the characteristics of tephra deposits. In Chapter II, I calculate the eruption source parameters for the ~7.7 ka Cleetwood eruption of Mount Mazama (Crater Lake/giiwas, Oregon, USA) using new data collected in the field. I also develop and apply a novel approach combining laser diffraction and dynamic image analysis to produce high-resolution grain-size distributions for tephra samples spanning the range of sizes of the ejected tephra, from less than a micron to several centimeters. The ~7.7 ka Cleetwood eruptive sequence consisted of two consecutive VEI 4 eruptions: the lower and upper Cleetwood units, respectively, with the lower Cleetwood being the most intense, producing a ~19 km plume which deposited 0.98 km^3 of tephra. Altogether, the Cleetwood eruption emplaced ~1.10 km^3 (non-DRE) of tephra from at least one, but no more than two, plumes, and was followed by a continuous transition to an effusive stage which emplaced a ~0.6 km^3 rhyodacitic lava flow. The Cleetwood eruption is a significant historic eruption because 1) it immediately preceded the climactic caldera-forming eruption of Mount Mazama, one of the largest eruptions of the Holocene, and 2) it is similar, both in terms of magma chemistry and sedimentological characteristics, to the only two witnessed volcanic eruptions of highly silicic magma that have transitioned from an explosive to an effusive phase (2008 Chaitén [Chile]; 2011-2012 Cordón Caulle, [Chile]). Results from high-resolution cumulative grain-size distributions show two systematic breaks in slope from a power-law relationship at ~0.125 mm and ~0.510 mm, creating three individual segments that can all be fit by a power-law relationship, regardless of eruptive phase or location within the deposit. I show that the slope, or fractal dimension, of the first segment (particles <0.125 mm) can be used to

determine the potential energy of fragmentation. The shallow slope of the second segment (0.125 mm< particles <0.51 mm) is due to particle rafting, which was discovered thanks to detailed componentry. Finally, the third segment reflects the loss of coarse ash and lapilli with distance from the vent. This chapter shows that combining eruption source parameters, detailed componentry, and high-resolution grain-size distributions from individual locations within a deposit provide insights into magma fragmentation, tephra transport, and the evolution of silicic eruptions with time.

The excellent medial deposit preservation of the Cleetwood tephra deposit due to the rapid capping by the subsequent climactic caldera-forming eruption, makes this eruption a unique natural laboratory to explore the ability for volcanic ash transport and dispersal models to accurately reproduce both mass loads and grain-size distributions at individual locations. Furthermore, the overall coarse nature of the medial deposit allows for modeling this region without having to account for transport modifiers such as ash aggregation. In the work presented in Chapter III, I re-evaluate the eruption source parameters for the lower Cleetwood unit following the excavation of a new, 5-meter-deep outcrop. I further include a high-resolution total grain-size distribution and perform a detailed wind analysis above Crater Lake. I use these updated eruption source parameters and wind analysis as inputs in the Tephra2 volcanic ash transport and dispersal model to estimate the geometry and dimensions of the volcanic plume. I compare model results with those obtained through detailed field analysis, using both the mass load and the grain-size distributions as constraints on the model results. Re-evaluation of the lower Cleetwood unit shows a ~14.4 km plume depositing a mass of ~4.5×10^{11} kg of tephra, which has a coarse total grain-size distribution with a median grain-size of 3.84 mm. The wind analysis suggests that the Cleetwood eruption probably began sometime between late summer and mid-spring. Using a grid search approach, I show that the classic version of Tephra2 that uses a vertical line as a source reproduces well mass loads and grain-size distributions independently with two sets of parameters, but fails to give good fits for both simultaneously with a single set of empirical inputs. To nicely fit grain-size distributions, an extremely large diffusion coefficient needs to be used, a parameter dictating how fast particles can diffuse in the atmosphere. This very large value suggests that accounting for the probable umbrella shape of the lower Cleetwood plume is critical to use volcanic ash transport and dispersal models in an

insightful manner. To test this hypothesis, I adapt Tephra2 by post-treating the output to mimic a deposition via an umbrella cloud, rather than a single, vertical line. Applying a grid search over possible umbrella cloud geometries and plume heights gives the best results with a plume having a 4x40 km^2 elliptical geometry. This oval geometry resembles those seen during the 2014 eruption at Kelud (Indonesia) and the 2015 eruption at Calbuco (Chile), albeit more elongated. With this plume geometry, both the twenty-five mass loads and high-resolution grain-size distributions collected from the field can be nicely fit by Tephra2. This chapter highlights the importance of using high-resolution grain-size distributions to constrain wind conditions and plume geometry for unwitnessed eruptions and demonstrates the possibility to forecast proximal and medial deposits with an analytical, fast-calculating volcanic ash transport and dispersal model.

Prior to the 2008 eruption of Chaitén (Chile) and the subsequent 2011-2012 eruption of Cordón Caulle (Chile), no eruption of rhyodacitic/rhyolitic magma had been observed in modern history. Both eruptions showed an overall transition from explosive to effusive activity. At Cordón Caulle, direct observations captured the transport of tephra to the surface through fractures within the simultaneously erupting obsidian flow. In Chapter IV, I combine detailed componentry and high-resolution grain-size distributions of the products of the hybrid phase of the 2011-2012 eruption of Cordón Caulle I collected in 2022. The aim of this study is to constrain the physical mechanisms by which the Cordón Caulle eruption shifted from a hybrid explosive/effusive activity to an exclusively effusive one. Stratigraphic analysis of the hybrid phase shows the repeating occurrence of reversely graded couplets that alternate between lapilli-dominated and fine ash-dominated. Detailed componentry analysis reveals the absence of lithics as a major component, and that the tephra is always ultra-dominated by pumice and obsidian pyroclasts. There is a net increase in the intermediate components (banded pumices, broken pieces of the flow) and crystals at the expense of pumice towards the end of the eruption. These deposit and component characteristics suggest that ash sintering along the upper part of the plumbing system after fragmentation produced a dense plug that obstructed the shallow conduit, causing the system to repressurize and subsequently shatter parts of the plug with each explosive event. This progressive increase in dense components may signify the catalyst for the eventual cessation of explosive activity. This research on the physical and component characterization of

tephra from the hybrid phase of the 2011-2012 eruption of Cordón Caulle remains in progress. Further textural analysis and direct comparison with effusive products from the same eruption is needed to continue to explore how these eruptions transitions from explosive to hybrid to purely effusive activity.

CHAPTER II

USING ERUPTION SOURCE PARAMETERS AND HIGH-RESOLUTION GRAIN-SIZE DISTRIBUTIONS OF THE 7.7 KA CLEETWOOD ERUPTION OF MOUNT MAZAMA (OREGON, USA) TO REVEAL PRIMARY AND SECONDARY ERUPTIVE PROCESSES

From Wiejaczka J and Giachetti T (2022) Using Eruption Source Parameters and High-Resolution Grain-Size Distributions of the 7.7 ka Cleetwood Eruption of Mount Mazama (Oregon, United States) to Reveal Primary and Secondary Eruptive Processes. Front. Earth Sci. 10:853021. doi: 10.3389/feart.2022.853021

1 Introduction

Volcanic plumes and tephra fallout from explosive eruptions are the most far reaching of the volcanic hazards and have the potential to cause fatalities, disrupt the global economy, and affect climate (McCormick et al., 1995; Robock 2000; Sigl et al., 2015; Choumert-Nkolo et al., 2021). Tephra dispersion and sedimentation models are used before and during an eruption to forecast and mitigate impacts to air traffic and communities in the path of an evolving volcanic ash cloud (Bonadonna et al., 2005; Schwaiger and Mastin, 2012). The accuracy of these forecasts largely depends on that of input eruption source parameters (ESPs) such as plume height (H_t), erupted volume (V), mass eruption rate (MER), and the Total Grain-Size Distribution (TGSD) of particles ejected by a volcano into the atmosphere. These initial eruption source parameters are challenging to constrain in real time and thus rely on information obtained from detailed field studies of analogous eruptions. The construction of isopach and isopleth maps and the collection of individual grain size distributions, which are all needed to calculate ESPs, are at times challenging, in part because proximal deposits are usually too thick to be accurately measured and described, and distal deposits are often missing. It is thus crucial to better understand the relationships between eruption source parameters and the characteristics of the deposit (e.g., thickness and grain size distribution as a function of location compared to the vent and main dispersal axis).

The TGSD of a given eruption evolves with time from fragmentation in the conduit to final deposition on the Earth's surface. The primary products of magma fragmentation exhibit cumulative grain-size distributions (i.e., the 'primary TGSD') that can be fit with a power-law relationship, $(N > d) = \lambda d^{-D}$, where N is the number density of particles, d is the equivalent

particle diameter, λ is a scaling factor, and *D* is the power-law exponent or fractal dimension (Kaminski and Jaupart, 1998; Kueppers et al., 2006; Giachetti et al., 2021). Experimental fragmentation of volcanic products in particular yields *D* values that are always <3 and mostly around 2.5±0.3 (Turcotte, 1997; Kaminski and Jaupart, 1998; Kueppers et al., 2006, Perugini and Kueppers 2012). Kueppers et al. (2006) further showed that the fractal dimension of the size distributions of the products of experimental magma fragmentation by rapid decompression is positively correlated with the potential energy for fragmentation, and thus that *D* reflects the explosivity of an eruption. After fragmentation in the conduit, the primary TGSD evolves due to processes that can either increase (e.g., expansion, amalgamation and sintering; Rust and Cashman, 2011; Giachetti et al., 2021) or decrease (e.g., disruption, attrition, comminution, abrasion; Dufek and Manga, 2008; Dufek et al., 2012; Kueppers et al., 2012; Jones and Russel, 2017) the size of pyroclasts, making the TGSD one of the most difficult ESPs to constrain (Pioli et al 2019). This overprinting of post fragmentation processes on the 'final TGSD' of tephra makes the primary TGSD, and thus the potential energy for fragmentation, challenging to determine. Additionally, the TGSD that needs to be implemented in tephra dispersion and deposition models (e.g., Tephra2, Bonadonna et al., 2005; FALL3D, Folch et al., 2020; NAME, Jones et al., 2007; Ash3D, Schwaiger and Mastin, 2012), and its evolution with time and space, are poorly constrained because both the location and extent of secondary fragmentation in the conduit and/or the plume remain unclear. Provided the processes that affect the final TGSD can be disentangled, the latter can be used to gain information such as the depth and mechanisms of fragmentation, eruption column heights, the state of the magma at fragmentation, and the energy released by explosive fragmentation (Perugini and Kueppers, 2012; Kueppers et al., 2006; Rossi et al., 2019).

The final TGSD of an explosive eruption, later simply referred to as 'TGSD', is interpolated from individual grain-size distributions (GSDs) of the tephra deposit measured after the eruption at multiple locations (e.g., Murrow et al., 1980; Walker 1980,1981a,1981c; Sparks et al., 1981; Carey and Sigurdsson 1982; Parfitt 1998; Bonadonna and Houghton 2005; Costa et al., 2016; Pioli et al., 2019). Due to secondary fragmentation and transport-related processes, individual GSDs vary from location to location and differ from both the final TGSD (Pioli et al., 2019; Mele et al., 2020) and the primary TGSD (Kaminski and Jaupart, 1998; Dufek et al., 2012; Giachetti et al., 2021). How these GSDs vary with direction, distance from the vent, and ESPs

can illuminate processes that occur during transport and affect particles differently depending on their size, density, and shape (e.g., ash aggregation; Rose and Durant, 2011; Saxby et al., 2018; Rossi et al., 2021). It might thus be possible to glean information about both primary and secondary eruptive processes by comparing detailed GSDs of a single deposit obtained at different locations.

In this study, we calculate ESPs for the ~7.7 ka Cleetwood eruption of Mount Mazama (Crater Lake/giiwas, Oregon, USA; Young 1990), which immediately preceded the climactic caldera-forming eruption of the same volcano, one of the largest eruptions of the Holocene (Bacon, 1983; Buckland et al., 2021). Additionally, we apply a novel approach to produce high-resolution grain-size distributions of tephra samples over the range 0.00035-35 mm, by combining laser diffraction and dynamic image analysis techniques. Together with ESPs and detailed componentry, the high-resolution of these grain-size distributions from individual locations within the Cleetwood deposit provides insight into magma fragmentation, tephra transport, and how the Cleetwood eruption evolved over time.

2 Geologic Background

Located in Oregon in western North America, Mount Mazama is one of the major stratovolcanoes making up the Cascade Volcanic Arc. Mount Mazama is especially known for the approximately 8×10 km^2 diameter caldera that formed during the ~7.7 ka climactic eruption and which now contains Crater Lake (referred to as giiwas by the Klamath tribes) within it. The Mazama edifice began forming ~420 ka ago with the emplacement of basaltic andesite to dacitic lava flows. Mainly effusive activity continued until ~27 ka ago with andesitic and dacitic compositions being volumetrically dominant (Bacon, 1983). The eruption of a rhyodacitic lava flow ~27 ka ago marked the first eruption from the magma chamber that would later serve the climactic caldera-forming eruption (Bacon and Lamphere, 2006). The climactic eruption was preceded by two Plinian eruptions, Llao Rock and Cleetwood. The ~7.9 ka Llao Rock eruption deposited a tephra fall unit of 2.27 km^3 (non-DRE) followed by a rhyodacitic lava flow of ~0.5 km^3 (Bacon, 1983; Young, 1990). The Cleetwood eruption (described in detail below) followed and began with a Plinian phase that erupted a total of 1.54 km^3 (non-DRE) of pyroclastic fall material according to Young (1990). Explosive activity then transitioned to an effusive stage, with no apparent break, extruding a rhyodacitic lava flow with a minimum volume of ~0.6 km^3

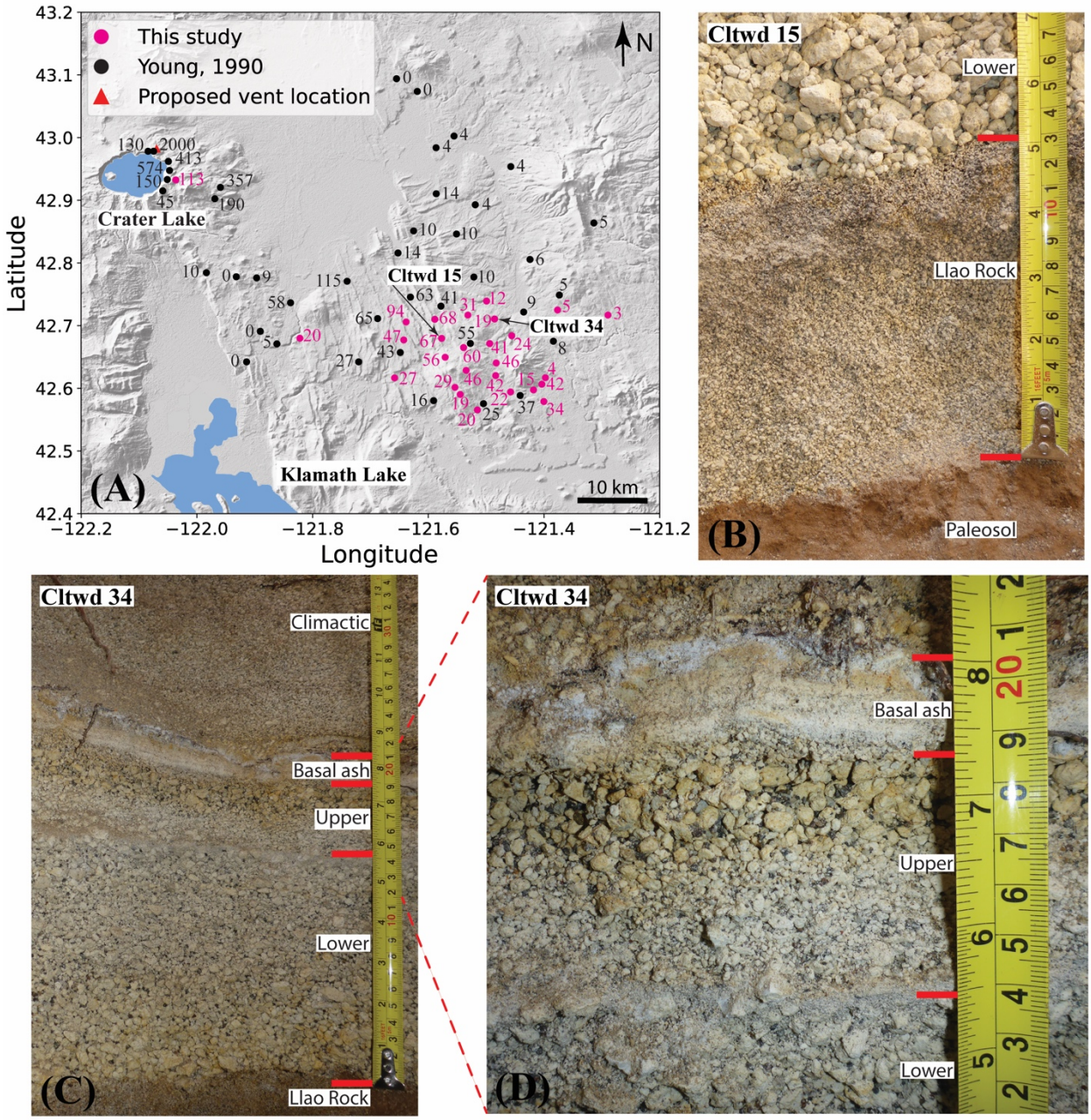

Figure 1. (A) Location of collected samples with total Cleetwood eruption thicknesses (cm) from this study, in pink, and Young (1990), in black. Proposed vent location from Bacon (1983) and background is global earth relief (Tozer et al., 2019). **(B)** Photograph showing all of Llao Rock and the contact between Llao Rock and the lower Cleetwood unit at location Cltwd 15. Note the drastic increase in size of pyroclasts from Llao Rock to the lower Cleetwood. **(C)** Stratigraphic sequence showing lower Cleetwood, upper Cleetwood, and the overlying Climactic deposit at location Cltwd 34. Llao Rock is not present at this location. **(D)** Closeup photograph showing the end of the lower Cleetwood, upper Cleetwood, and the Basal ash layer, which marks the beginning of the Climactic deposit (Young, 1990). Note the gray fine ash layer defining the boundary between the lower and upper Cleetwood units. Measuring tape is in both inches (left) and centimeters (right).

(Bacon, 1983). Although the exact timing of the Cleetwood eruption is still unclear, the back-flowing of the Cleetwood flow into the caldera and the fact that pumice from the climactic eruption are oxidized and welded to the top of the Cleetwood flow suggest that it occurred within weeks to no more than 100 years before the onset of the climactic eruption (Bacon, 1983; Kamata et al., 1992). The climactic caldera-forming eruption of Mount Mazama occurred 7633 ± 49 cal yr BP (Egan et al., 2015) in two distinct but continuous phases and erupted ~176 km^3 of tephra (61 km^3 DRE; Buckland et al., 2020). The first phase consisted of a single-vent Plinian eruption followed by column collapse and the emplacement of the Wineglass Welded Tuff ignimbrite. The second, ring-vent phase produced a voluminous ash-flow and led to the formation of the caldera (Bacon, 1983; Young, 1990). The products forming four volcanic edifices were erupted after the caldera formed, with the extrusion of a 0.074 km^3 unnamed dome ~4.8 ka ago being the most recent volcanic activity at Crater Lake (Bacon et al., 2002).

2.1 The Cleetwood Eruption

To the best of our knowledge, all currently available information concerning the physical characteristics of the Cleetwood eruption of Mount Mazama comes from the works of Bacon (1983), Young (1990), Bourgeois (1998), and Wearn (2002). A summary of these studies related to the main deposit features and eruptive parameters is provided here.

The vent associated with the Cleetwood deposit is allegedly located near Cleetwood Cove in the low hills NE of the Crater Lake Rim Drive (Bacon, 1983) (Figure 1). At ~35 km ESE of this vent, the Cleetwood tephra deposit is still >1 m thick and exhibits two units, the main/lower Cleetwood, herein referred to as lower, and the thinner upper Cleetwood, following Young's nomenclature (Young, 1990). The lower Cleetwood unit (1.15 km^3 non-DRE; Young, 1990) is characterized by strong normal grading and presents two distinct normally graded packages in thicker sections. The break within the lower Cleetwood unit does not affect the overall normal grading of the unit and does not represent a significant pause in eruptive activity (Young, 1990). The upper Cleetwood unit (0.39 km^3 non-DRE; Young, 1990) is characterized by strong reverse grading, with a grey ash layer at the base that rapidly grades into coarser material primarily composed of pumice and obsidian pyroclasts. Due to the nature of proximal deposits and their tendency to obscure characteristics created from changes in eruption dynamics, the lower and upper Cleetwood units are indistinguishable at exposures on the caldera walls (Cleetwood Cove,

Wineglass, and Skell Head; Young, 1990; Bourgeois, 1998). The Cleetwood fall deposit is ~20 m thick at Cleetwood Cove, where individual lithic blocks can reach up to 1 m in diameter. This location contains alternating layers of lapilli/blocks and ash that decrease in thickness upwards through the section. The ash layers have been interpreted as intra-Plinian pyroclastic flows (Young, 1990).

The Cleetwood deposit is poor in finer material. In medial deposits where two distinct packages are present, lithic content is highest at the base of both packages and generally decreases with stratigraphic height. The abundance of lithics at these two positions within the stratigraphy suggests vent initiation and clearance (Young, 1990). Obsidian pyroclasts are the most abundant in the upper Cleetwood unit and generally increase with stratigraphic height at proximal exposures. The general decrease in lithics and increase in obsidian pyroclasts with time suggests a conduit that is progressively annealed with obsidian. This annealed obsidian is later eroded during the final explosive phase (Young, 1990; Bourgeois, 1998; Wearn, 2002). Observations at proximal locations suggest that the eruption column was sustained through time (Bourgeois, 1998), although the normally graded lower Cleetwood unit and the reversely graded upper Cleetwood unit indicate fluctuations in column height. The Cleetwood eruption is estimated to have an initial column height of 30 ± 5 km and an average mass eruption rate of $(2\pm1)\times10^{8}$ kg s^{-1} (Young, 1990). Explosive activity then transitioned to an effusive stage, with no apparent break, and extruded a ~0.6 km^3 rhyodacitic lava flow. ESPs and the continuity of the Cleetwood eruption are reevaluated herein.

3 Methods

3.1 Field

Field work was conducted in 2018 and 2021 on the Cleetwood tephra fall deposit, 6 km to 71 km southeast of the proposed vent location (Figure 1). Twenty-eight pits were dug by hand until the bottom of the Cleetwood tephra deposit was reached. At each location, the deposit was divided into subunits based on visible changes in grading, particle size, color, and/or componentry, if applicable. Subunits were then described in detail, measured for their thickness, photographed, and several hundred grams to a few kilograms of each subunit were collected. Sampling the Cleetwood deposit itself was sometimes challenging due to the massive amount of

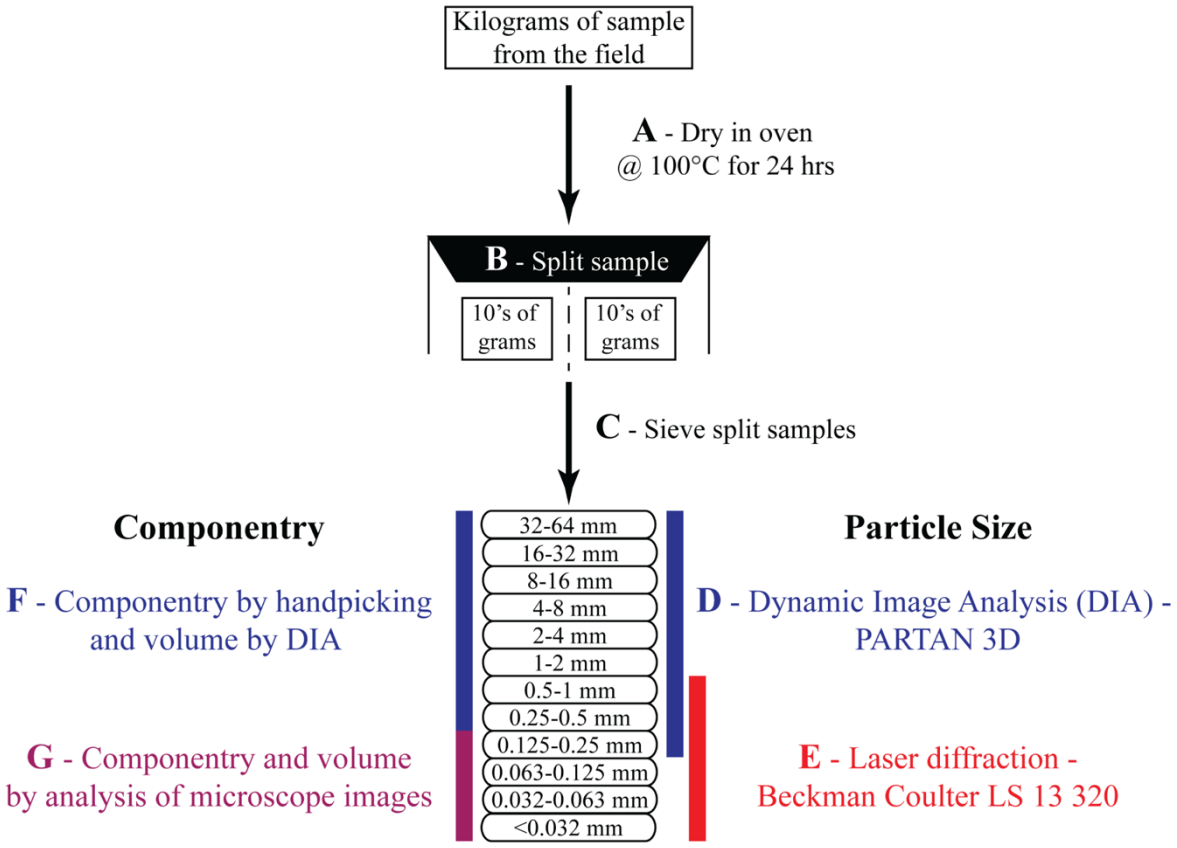

Figure 2. Summary of the workflow steps of our study. **(A)** All samples collected from the field were dried in an oven at 100° C for 24 hrs to remove adsorbed water. **(B)** Samples were then split into workable aliquots of tens of grams each. **(C)** Split samples were manually sieved into twelve discrete size fractions. **(D)** Dynamic image analysis was performed on size fractions 0.125-0.25 mm and larger. **(E)** Laser diffraction analysis was performed on size fractions 0.5-1 mm and smaller. **(F)** Componentry for particles in size fractions 0.25-0.5 mm and larger was determined via handpicking under a stereo microscope and analyzing particle volumes using DIA. **(G)** Componentry and volume of particles in size fractions 0.125-0.25 mm and smaller were determined via microscope images.

tephra produced by the climactic eruption of Mount Mazama that lie atop the Cleetwood tephra fall, reaching up to 2.3 meters in this field area depending on sampling location.

3.2 Laboratory Analyses

All samples collected at the 28 locations visited were analyzed for mass distribution by sieving and weighing. Samples from three locations, Cltwd 5, Cltwd 17, and Cltwd 18, respectively located at 46 km, 56 km, and 66 km from the proposed vent and roughly on the main dispersal axis of the Cleetwood eruption, were further analyzed for high-resolution grain-

size distributions. Componentry was realized on all samples collected at Cltwd 5. We encourage the reader to use Figure 2 to follow our analytical protocol described thereafter.

3.3 High-Resolution Grain-Size Distribution

3.3.1 Individual Analysis

Tephra samples from each subunit were first dried in a convection oven at 100 ˚C for 24 hr to remove adsorbed water (Figure 2A). Bulk samples (kilograms) were split into workable aliquots (10's of grams) using a Humboldt testing equipment sample splitter (Figure 2B). Each aliquot was then manually sieved into twelve discrete sieve size fractions: 0-0.032 mm, 0.032-0.063 mm, 0.063–0.125 mm, 0.125–0.25 mm, 0.25–0.5 mm, 0.5–1 mm, 1–2 mm, 2–4 mm, 4–8 mm, 8–16 mm, 16-32 mm and 32-64 mm (i.e., every phi size from -5 to 5; Figure 1C). Each size fraction was then weighed using a high-precision balance before high-resolution particle size analysis. Sieving was carried out before size analysis to 1) prevent larger particles from obscuring smaller ones during the analysis, which improves accuracy and precision of data collected via both Dynamic Image Analysis (DIA) and laser diffraction techniques, and 2) to allow for the measurement of the average density of the bulk tephra fall deposit at each size fraction, which is needed to convert masses to volumes and vice versa.

The size of each particle from each size fraction >0.125 mm was measured via DIA using a Microtrac PARTAN 3D particle size and shape analyzer at the University of Oregon (Figure 1D; Trafton and Giachetti, 2021). In this apparatus, particles travel along a vibrating tray and fall and rotate in front of a LED backlit screen. Once in freefall, a high-speed, high-resolution camera (100 fps, 15 μm px^{-1}) tracks and records images of all individual particles, taking up to twelve images of each particle. Unlike other DIA instruments, the Microtrac PARTAN 3D uses multiple images of individual particles to measure their size and shape. Using multiple images of individual particles to determine these parameters is critical given the multitude and often extreme shapes of volcanic particles (Riley et al., 2003; Liu et al., 2015). The PARTAN 3D theoretically allows for the measurement of particles from 0.035 to 35 mm, but we found the analysis of volcanic ash <0.125 mm cumbersome and poorly reproducible due to static attraction between particles forming aggregates and thus did not analyze particles <0.125 mm with this instrument. For each particle analyzed, the PARTAN 3D provides, amongst other parameters, the particle size (volume, equivalent diameter) and shape parameters (e.g., form factor, axial ratio,

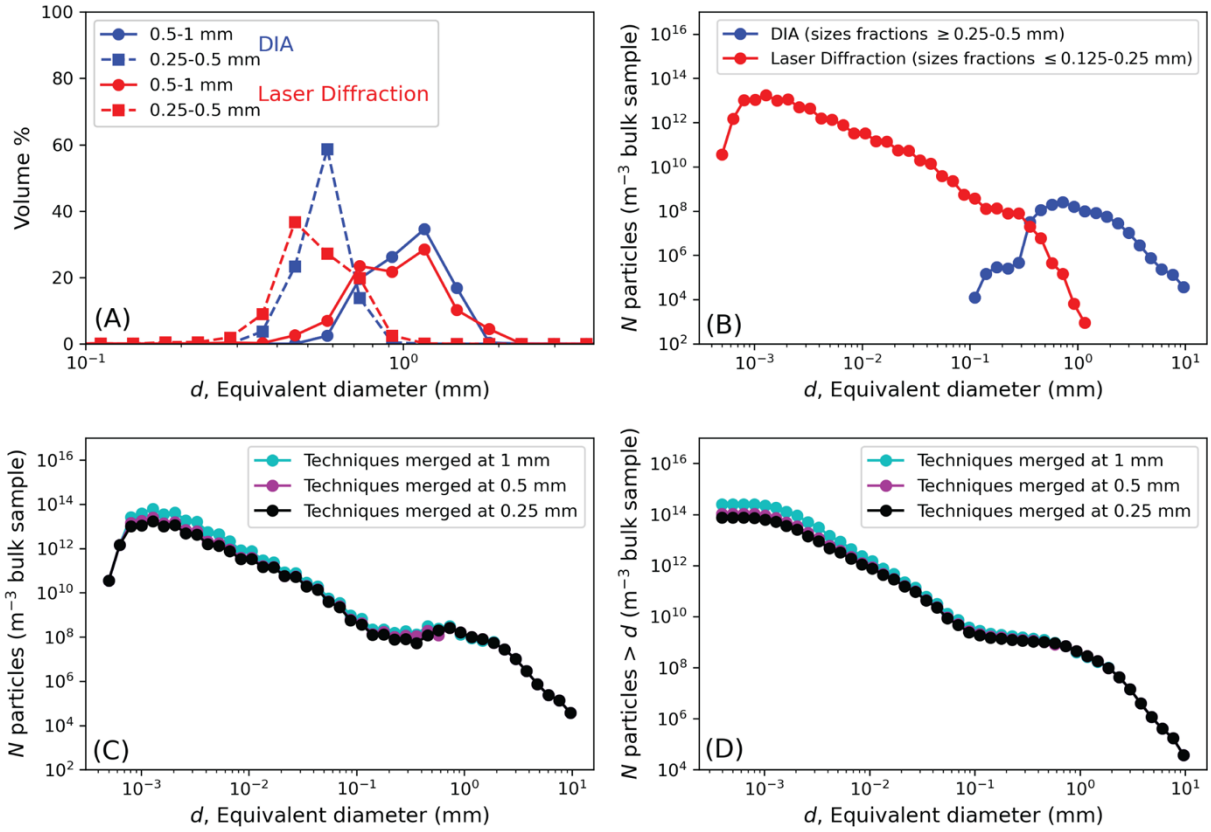

Figure 3. (A) Volume % as a function of equivalent diameter, *d*, for DIA and laser diffraction analyses of two identical size fractions (0.25-0.5 and 0.5-1 mm). Note that for the size fraction 0.25-0.5 mm, the volume % peak for DIA occurs at larger sizes compared to the laser diffraction technique, due to the way the volume of particles is measured (spherical assumption in laser diffraction, whereas shape is measured and thus taken into account using DIA). **(B)** Number density of particles per cubic meter of bulk sample, *N*, as a function of their equivalent diameter, *d*, showing the overlap between laser diffraction and dynamic image analysis (DIA) data. Each curve is an amalgamation of data obtained for several size fractions using a single technique. Sample used here is Cltwd 5A. **(C-D)** Number density, *N*, and cumulative number density ($N > d$) of particles per cubic meter of tephra plotted as a function of equivalent diameter, *d*. These graphs illustrate the impact of choosing different cutoffs (0.25, 0.5, or 1 mm) when merging data from DIA and laser diffraction. Note that the break in slope occurs at the same position regardless of the cutoff and thus is not an artifact of data combination.

solidity, convexity), thus creating a list of hundreds to hundreds of thousands of lines for each size fraction. Altogether, 10^4-10^6 particles >0.125 mm were individually analyzed per sample using this technique. This method is non-destructive and multiple analyses of individual batches of particles show very good reproducibility for particles >0.125 mm. Only size measurements, not shape, were used in this study.

Size measurements on aliquots of particles 0–1 mm were carried out using laser diffraction on a Beckman Coulter LS 13 320 at the USGS Cascades Volcano Observatory (Figure 2E; Blott et al., 2006). Although this method does not output an exact number of particles analyzed, we estimate that ~10^5–10^7 particles from each subunit were measured using this technique based on the volume of aliquots used and size distributions obtained. This instrument provides information on particle size in the form of volume fraction as a function of an equivalent diameter, in 93 logarithmic bins regularly spaced from 0.00038 to 2 mm. It does not provide information on particle shape, but rather assumes that particles are spherical to calculate their equivalent diameter.

3.3.2 Combining Datasets

Size data for size fractions 0.125–0.25 mm, 0.25–0.5 mm, and 0.5–1 mm were obtained using both DIA and laser diffraction (Figure 2D-E, Figure 3), allowing for a comparison and combination of the two datasets. Because the PARTAN 3D gives the size of individual particles whereas laser diffraction provides volume fractions, some conversions and re-binning of the data need to be performed before comparing and combining the datasets. In this study, results are sorted and presented in 50 logarithmic bins from 0.00035 to 35 mm, and both the distributions of mass and number density of particles as a function of their size are used.

Data collected by laser diffraction for each size fraction were first converted from volume percent to an actual volume using the mass and density of the size fraction. For each size fraction of each sample, the bulk density of the tephra sample was calculated by dividing the mass of all particles, obtained using a high-precision balance, by the volume they represent. For each of the size fractions 0.125–0.25 mm, 0.25–0.5 mm, and 0.5–1 mm, that volume is the sum of the volumes of all particles analyzed by DIA within that size fraction. For size fractions 0-0.032 mm, 0.032-0.063 mm, and 0.063-0.125 mm, density of the bulk tephra was determined directly using helium pycnometry (Micromeritics AccuPyc II 1340), assuming all particles at these sizes are vesicle-free, which was confirmed by observation under the microscope. Next, the number of particles for each bin was calculated by assuming spherical particles (as assumed when using laser diffraction technique) and dividing the total volume of each bin by the volume of a single particle with a diameter equal to the middle of the bin (Figure 3B). For DIA, individual particles are analyzed, and the number of particles per bin was thus obtained directly. Number of particles

per cubic meter of tephra was then calculated by dividing the number of particles per bin by the total volume of the sample analyzed. Finally, to produce a single distribution, we use laser diffraction data obtained on all size fractions 0-0.25 mm and DIA data for all size fractions >0.25 mm (Figure 3C). Note that we present the data as cumulative number density in most plots (Figure 3D). We refer to these individual Grain Size Distributions as GSDs in the paper.

3.4 Componentry

Previously split samples (10's of grams) for each discrete size fraction were further split into aliquots of a few grams using a SOILTEST sample splitter to be analyzed for componentry. For size fractions ≥ 0.25 mm, all particles of the aliquot were handpicked and sorted into one of the following components using a stereomicroscope: pumice, banded pumice, obsidian pyroclast, lithic, and loose crystal (Supplementary Figure 1). Once separated, all particles of each component were analyzed using the Microtrac PARTAN 3D to measure the relative volume of all components in each size fraction. For size fractions 0.063-0.125 mm and 0.125-0.25 mm, images of the bulk sample were taken with a Leica M80 stereo microscope and individual particles were outlined based on type. The area of particle outlines from each component category was then calculated using the Fiji (ImageJ) image processing package (Schindelin et al., 2012), and particle volumes were calculated assuming a spherical shape. Upon visual inspection under the stereo microscope, all particles below 0.063 mm were classified as pumice. Altogether, 1,315-2,856 particles from each subunit were sorted.

3.5 Eruption Source Parameters

3.5.1 Erupted Volume

Isopach maps were constructed using field data from this study and work done by Young (1990). Isolines were manually drawn on Adobe Illustrator, and the area enclosed by each isoline was then calculated using the Fiji (ImageJ) image processing package. Airfall volume was calculated using *TephraFits* (Biass et al., 2019), which allows the user to best fit thickness (T, in cm) as a function of the square root of area ($\sqrt{A}$, in km) enclosed by each isoline using an exponential (Fierstein and Nathenson 1992; Bonadonna and Houghton 2005), a power-law (Bonadonna and Houghton 2005), or a Weibull (Bonadonna and Costa 2012) equation. To assess the uncertainty in our volume calculations we also ran *TephraFits* in probabilistic mode, which uses the stochastic methodology of Biass et al. (2014). We applied a 10% uncertainty to both our

thickness and area measurements in accordance with the uncertainties associated with isopach construction as quantified in the literature (Le Pennec et al., 2013; Engwell et al. 2013; Klawonn et al., 2014a, b). For statistical significance we performed a Monte Carlo simulation of 100,000 runs. Volumes are then reported as a median value with a confidence interval of 5^{th}-95^{th} percentiles.

3.5.2 Plume Height and Mass Eruption Rate

The maximum lithic (ML) size at each location was determined by averaging the diameter of the three largest clasts measured using digital calipers. Maximum lithic isopleth maps were then constructed using data from this study and the data from Young (1990), when possible. The same method for drawing isopach maps was used to construct the ML isolines (see above). Downwind and crosswind distances were then calculated using Fiji. Plume height, H_t (km), was calculated using the models of Carey and Sparks (1986) and Rossi et al. (2019) hereafter referred to as *CS86* and *R2019*, respectively. The mass eruption rate (*MER*, in kg/s) was then calculated using the model of Mastin (2014), where $MER = 140 \times H_t^{4.15}$ and H_t is the plume height expressed in km.

3.5.3 Total Grain-Size Distribution (TGSD)

The TGSD was determined by applying the Voronoi tessellation method of Bonadonna and Houghton (2005) to the 24 sieved-mass GSDs for all sample locations containing the lower Cleetwood unit. This method divides a tephra deposit into Voronoi polygons in which all interior points are closer to, and best represented by, a central sample point (centroid). The TGSD is then calculated by multiplying the GSD of the centroid by the mass fraction of its Voronoi polygon and summing all weighted GSDs. TGSD is presented herein as a cumulative number density. To determine the number density for a given grain-size, the mass (wt.%) of each phi size (-5 to 5) was first converted to a volume using a density model (Supplementary Table 1). Following Bonadonna and Phillips (2003), this model assumes a constant density of 2,380 kg/m^3 (i.e., the density of the glass as determined via helium pycnometry of crushed pumices) for particles smaller than 0.063 mm, a constant density of 455 kg/m^3 for particles larger than 2 mm, calculated by dividing the mass of all particles > 2 mm by their volume determined via DIA, and a linear increase in density between these bounds. Next, the number of particles was calculated

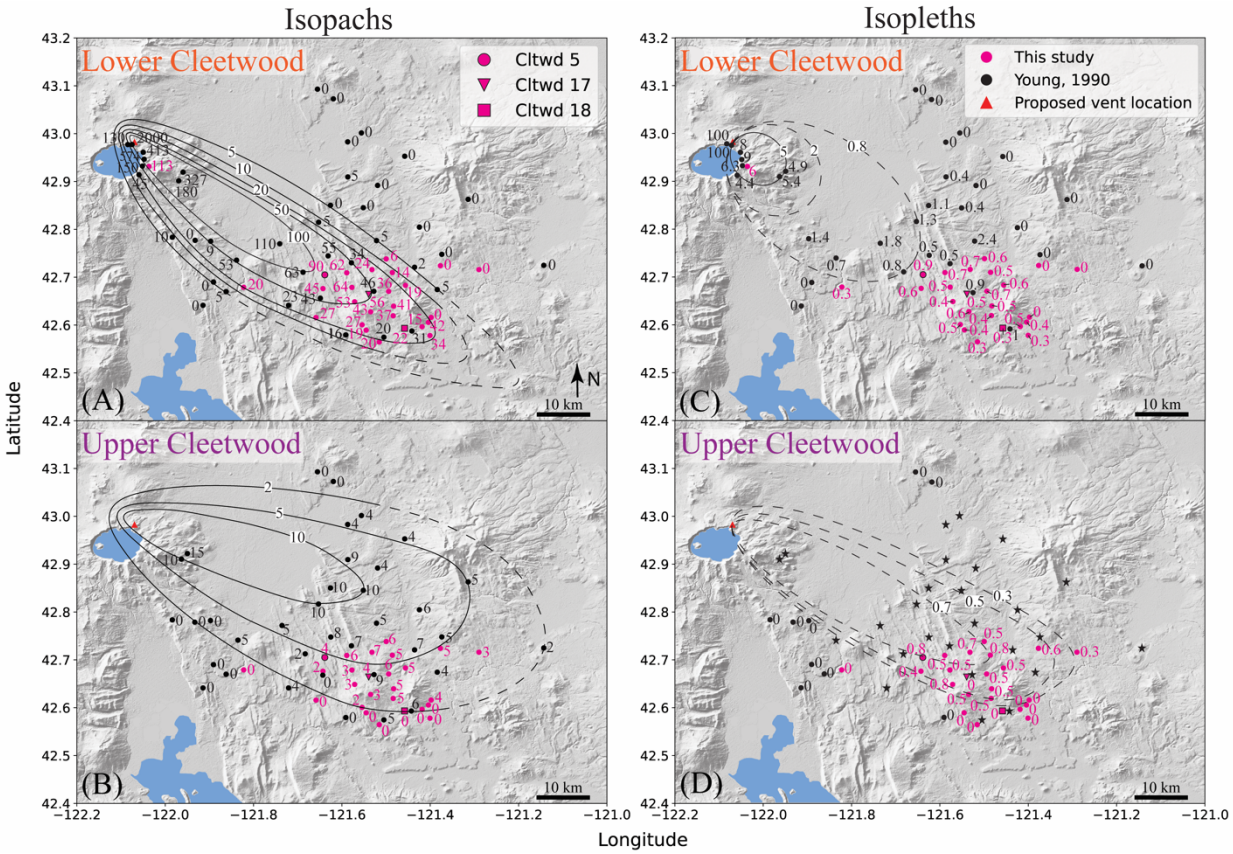

Figure 4. (A-B) Isopach maps for the lower and upper units of the Cleetwood eruption, respectively. **(C-D)** Maximum lithic (ML) isopleth maps for the lower and upper Cleetwood units, respectively. Stars on the upper Cleetwood isopleth map represent locations where the upper Cleetwood is present, but no ML data is available. All isolines are notated in centimeters. Background is global earth relief (Tozer et al., 2019).

by assuming spherical particles and dividing the total volume of each phi size by the volume of a single particle with a diameter equal to the mid interval between phi sizes. Finally, number density (m^{-3}) was calculated by dividing the number of particles per bin by the total volume of all phi sizes (-5 to 5).

4 Results

4.1 Field Observations and Measurements

Twenty-eight pits were dug by hand to the ESE of Crater Lake (Figures 1 and 4), covering the proximal and medial parts of the Cleetwood fall deposit. The Cleetwood and overlying Climactic deposits at these locations range from 2.5-113 cm and 12-232 cm in thickness, respectively.

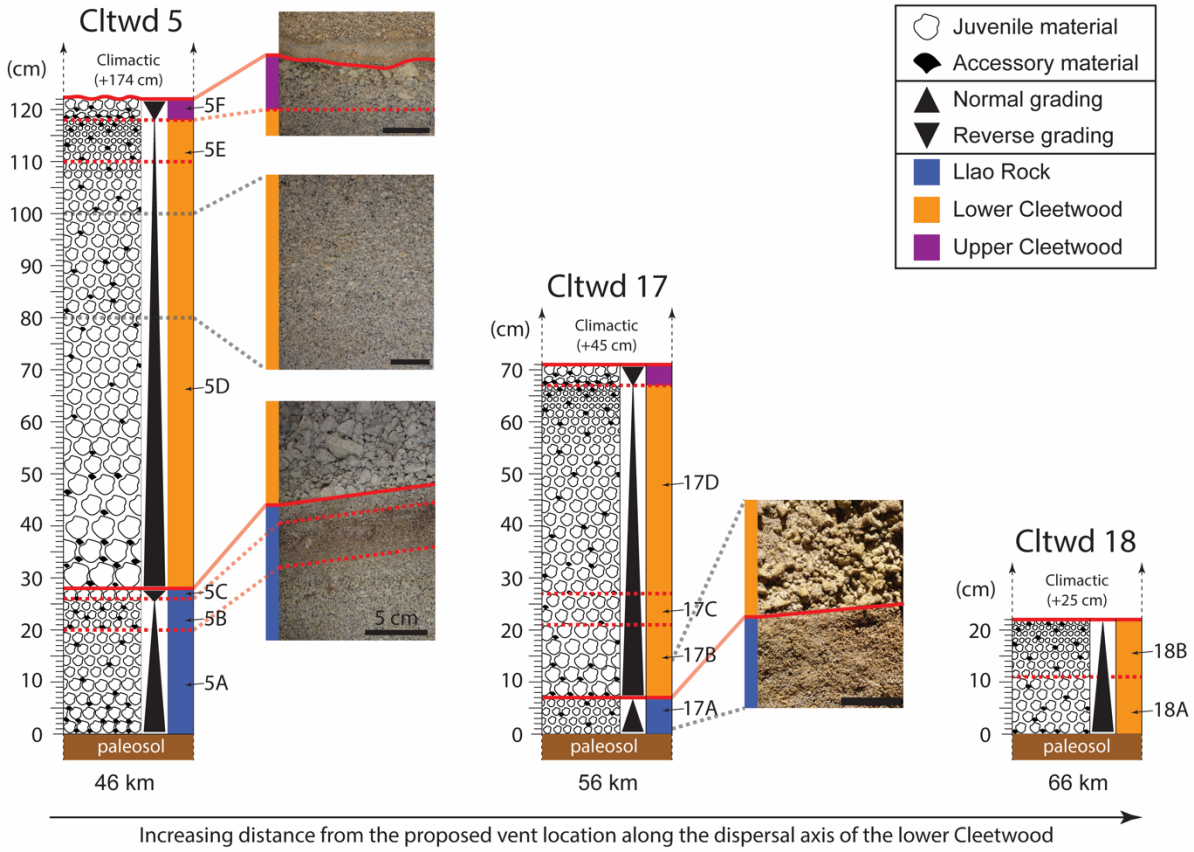

Figure 5. Stratigraphic columns for locations Cltwd 5, 17, and 18, all located on the main dispersion axis of the lower Cleetwood unit and at distances of 46 km, 56 km, and 66 km from the proposed vent, respectively (see Fig. 3). Solid red lines indicate sharp contacts between phases, whereas the dashed red lines divide areas within phases that were subsampled. Scale bar is 5 cm in all photographs. **Cltwd 5** exhibits Llao Rock and the two phases of the Cleetwood eruption. Llao Rock makes sharp contact with the paleosol, and three distinct subunits (A, B, C) are observed; subunit A (20 cm) normally grades into subunit B (6 cm) which then reversely grades into the uppermost subunit C (3 cm). Llao Rock and the lower Cleetwood make sharp contact. The lower Cleetwood unit (90 cm) is present as a normally graded unit. The upper Cleetwood unit (4 cm) is reversely graded, a characteristic seen at all locations where it is found. At **Cltwd 17,** Llao Rock and both Cleetwood phases are also observed. Llao Rock (7 cm) makes sharp contact with the paleosol but does not exhibit the three distinct subunits seen at Cltwd 5, it is normally graded. Llao Rock and the lower Cleetwood make sharp contact with each other. The lower Cleetwood normally grades until the upper Cleetwood unit. At **Cltwd 18**, only the lower Cleetwood (22 cm) is present and found as one normally graded unit that makes sharp contact with the paleosol at its base. At these three locations, the Cleetwood fall deposit is overlayed by 25-174 cm of climactic fall deposit.

Table 1: Fractal dimension values of cumulative grain-size distributions, D, for deposits present at locations Cltwd 5, 17 and 18 (Figure 2; Figure 4), together with the r^2 value of the fit. D1, D2, and D3 respectively correspond to the best fits of segments S1 (<0.125 mm), S2 (0.125-0.510 mm), and S3 (>0.510 mm) of the cumulative size distribution (see Figure 6B).

Location	Phase	D1	D1 r^2	D2	D2 r^2	D3	D3 r^2
Cltwd 5	Llao	2.25	0.99	0.38	0.98	3.87	0.97
Cltwd 5	Lower	2.62	0.99	0.34	0.99	2.95	0.99
Cltwd 5	Upper	2.70	0.98	0.67	1.00	2.71	0.98
Cltwd 17	Llao	2.08	0.99	0.61	0.97	4.65	0.95
Cltwd 17	Lower	2.58	0.99	0.40	0.99	3.10	0.99
Cltwd 18	Lower	2.47	0.99	0.63	0.99	3.32	0.99

The lower Cleetwood unit makes up most of the Cleetwood fall deposit and is 90 cm thick at Cltwd 5 (Figure 4A; Figure 5). The dispersal axis of the lower Cleetwood unit trends to the SE. This phase is characterized by a single, normally graded unit at all locations. Pumices, which make up most of the deposit of the lower Cleetwood, are white-grey and reach up to 5 cm in diameter at the base of the deposit in medial locations. The base of the lower Cleetwood contains ~15% lithics.

The upper Cleetwood unit is present up to ~80 km ESE of the proposed vent location (Figure 4C). Its dispersal axis trends to the ESE and is the widest of the two phases. At medial locations directly East of the vent, the upper Cleetwood is the only phase present. The deposit of the upper Cleetwood is characterized by a strong reverse grading (Figure 4) and a thin grey ash layer marks the boundary between the lower and upper units at medial locations SE of the vent. The contact between the lower and upper units is sharp with no visible signs of erosion. Obsidian pyroclasts are visibly more abundant within the upper Cleetwood compared to the other phase.

Overall, the dispersal axes of the lower and upper units seem to indicate a slight shift in the dominant wind direction from SE to ESE during the Cleetwood eruptive sequence (Figure 4A-B).

4.2 Individual Grain-Size Distribution

For locations where phases are divided into subunits (e.g., lower Cleetwood at Cltwd 5: 5D, and 5E), the thickness fraction of each subunit was used as a weight to calculate the GSD of the whole phase at that location using the individual GSDs of all subunits. Cumulative GSDs of

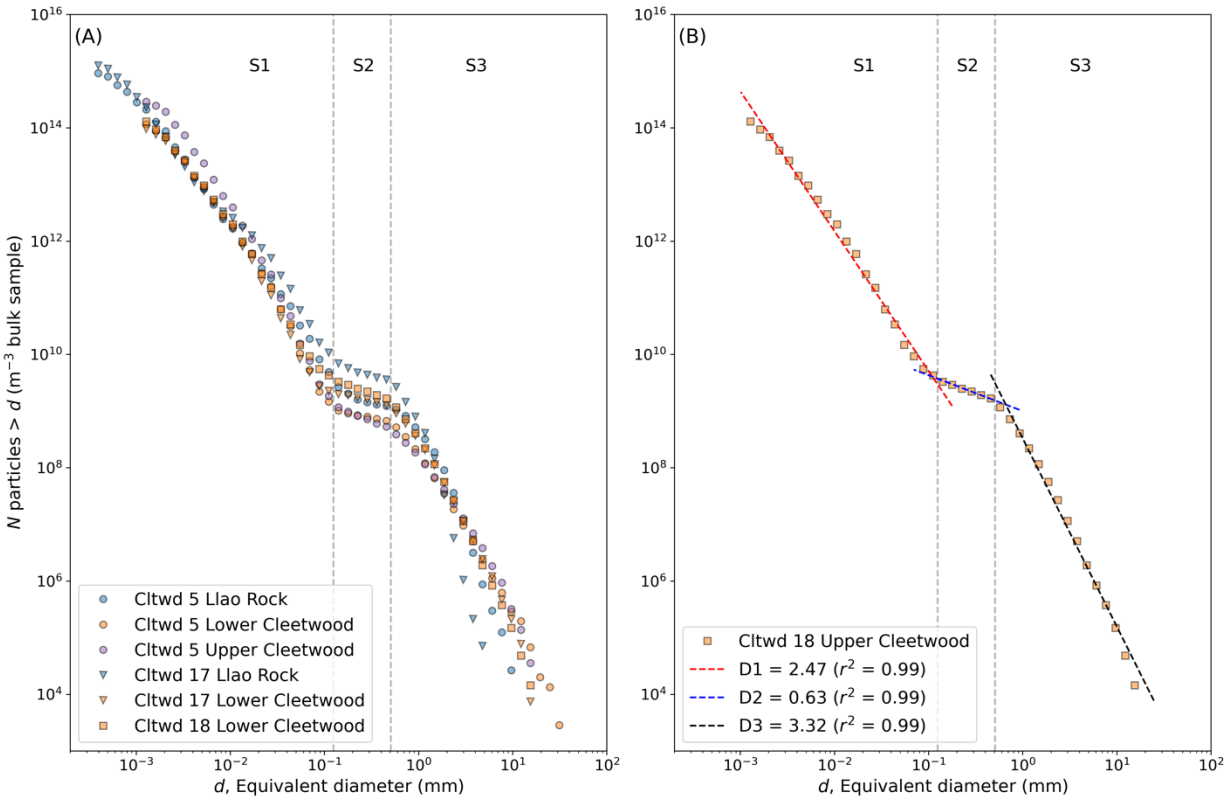

Figure 6. (A) Cumulative number density, *N*, versus equivalent diameter, *d*, for Llao Rock, lower, and upper Cleetwood units at Cltwd 5, Llao Rock and the lower Cleetwood at Cltwd 17, and the lower Cleetwood unit at Cltwd 18. **(B)** Cumulative number density, *N*, versus equivalent diameter, *d*, for the lower Cleetwood unit at Cltwd 18. Breaks in slope at ~0.125 mm and ~0.510 mm create three individual segments S1, S2, and S3, which are observed in all distributions (see A). Fractal dimensions (D1, D2, and D3) are obtained by fitting each corresponding segment with a power law, $N{>}d = \lambda d^{-D}$, where *N* is the number density of particles greater than size *d*, *D* is the fractal dimension, and λ is a scaling factor.

all units at Cltwd 5, Cltwd 17, and Cltwd 18 (~46, 56, and 66 km away from the vent) are similar in shape; they show two systematic breaks in slope from a power-law relationship at ~0.125 mm and ~0.510 mm (Figure 6A), creating three individual segments hereafter named S1, S2, and S3 (Figure 6B). Each segment can be fit by a power-law relationship, $N{>}d = \lambda d^{-D}$, where *D* is the fractal dimension of the segment of the distribution considered. For all units, *D1* values, which correspond to particles <0.125 mm (Table 1), range from 2.1-2.7. For a given phase, *D1* does not vary with distance from the vent. Values of *D2*, which correspond to particles ~0.125-0.510 mm in size, are the lowest of all *D*s for all units and range from 0.3-0.7. *D2* values slightly increase with distance from the vent for a given phase. Values of *D3*, for particles >0.510 mm, vary the

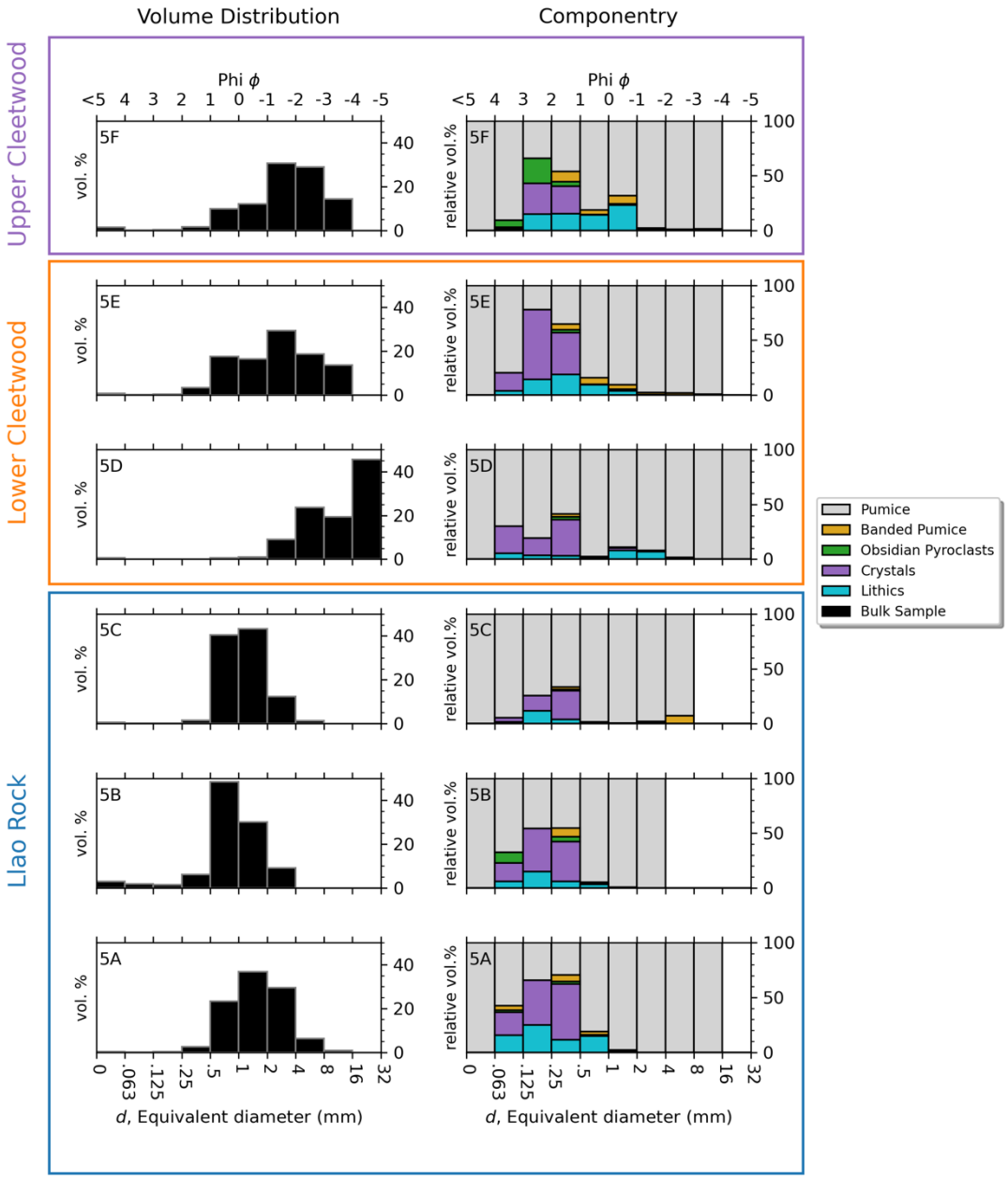

Figure 7. Volume percent of bulk samples (left) and relative volume percent of individual components within each size fraction (right), plotted as a function of equivalent diameter, *d*, for all subunits at location Cltwd 5. Subunits 5A, 5B, and 5C compose Llao Rock, 5D and 5E make up the lower Cleetwood, and the upper Cleetwood unit is defined solely by subunit 5F.

most (2.7-4.7) and increase with distance from the vent for a given unit. Note that the breaks in slope observed on all GSDs are also visible on the DIA and laser diffraction data when considered individually (Figure 3B), and thus were not artificially created following the combination of the two datasets.

Table 2: Best fit and probabilistic fitting parameters and erupted volumes obtained using *TephraFits* (Biass et al., 2019) for the two different phases of the Cleetwood eruption.

	Lower Cleetwood	**Upper Cleetwood**
Exponential Volume (km^3)	0.99 (r^2 = 0.99)	0.21 (r^2 = 0.99)
Power-law Volume (km^3)	0.97 (r^2 = 0.90)	0.22 (r^2 = 0.95)
Weibull Volume (km^3)	0.99 (r^2 = 0.99)	0.17 (r^2 = 0.99)
k_1	-0.1198	-0.0564
k_2	-0.1357	-
$T0_1$	728.67	33.0807
$T0_2$	1.09E+03	-
m	3.3609	1.7886
CPl	1.46E+06	2.38E+03
Θ	253.06	13.61
λ	17.15	35.10
n	1.50	1.91
Exponential Volume (km^3)	1.04 ± 0.18	0.21 ± 0.02
Power-law Volume (km^3)	1.00 ± 0.15	0.22 ± 0.02
Weibull Volume (km^3)	1.00 ± 0.24	0.19 ± 0.04
Error sqrt(A) (%)	10	10
Error thickness (%)	10	10
Error distal integration limit (%)	20	20

4.3 Componentry

Detailed componentry was realized on samples collected at Cltwd 5, a location ~46 km SE of the proposed vent, on the main dispersal axis of the lower Cleetwood (Figures 4 and 7). In all layers, pumice accounts for at least 92% of the sample's volume. In Llao Rock, pumice is the dominant component at all size fractions, although the proportion of lithics and crystals combined in subunits 5A and 5B reach 30-60 vol.% at sizes 0.063-0.5 mm. The proportion of non-pumice components decreases slightly from 5A to 5B and more significantly from 5B to 5C, with loose crystals being the dominant non-juvenile component in size fractions 0.063-0.5 mm, followed by lithics. The lower Cleetwood unit is divided into two subunits, 5D (bottom) and 5E (top). Subunit 5D is characterized by an increase in loose crystals compared to the end of Llao Rock (subunit 5C) and by the presence of lithics in size fractions 1-2 mm and 2-4 mm. Subunit 5E marks the end of the lower Cleetwood and exhibits an increase in banded pumice (2.9 vol.%) >0.25 mm and a slight increase in both loose crystals (1.7 vol.%) and lithics (2.9 vol.%) at sizes 0.063-1 mm. The upper Cleetwood unit (subunit 5F) shows an overall increase in both banded pumice and obsidian pyroclasts compared to the lower Cleetwood. The proportion of lithics in this phase increases in size fractions 0.5-2 mm, whereas the overall abundance of loose crystals decreases.

4.4 Eruption Source Parameters

Bacon (1983) first proposed the vent for the Cleetwood eruption to be located in the low hills northeast of the Rim Road. Applying the source vent locator model of Yang et al. (2019) that uses deposit thickness to find the vent confirms this general location (Supplementary Figure 2). The original location of Bacon (1983) lies between the power-law and exponential points generated by the model Yang et al. (2019) and is used as the source vent for all Phases herein.

The erupted volumes (non-DRE) of the lower and upper units of the Cleetwood eruption, calculated both using best fit models (Figure 8) and the probabilistic Monte Carlo approach of Biass et al. (2014), are reported in Table 2. For each phase, the three methods give volumes that are within 40% of each other using the best fit approach, with the exponential and Weibull methods always giving the best fits (r^2>0.99). Calculated volumes are 0.98±0.01 km^3 for the lower Cleetwood unit and 0.20±0.03 km^3 for the upper Cleetwood, making each of these phases a VEI 4 eruption. Volumes obtained using the probabilistic approach are 3-5% larger than using

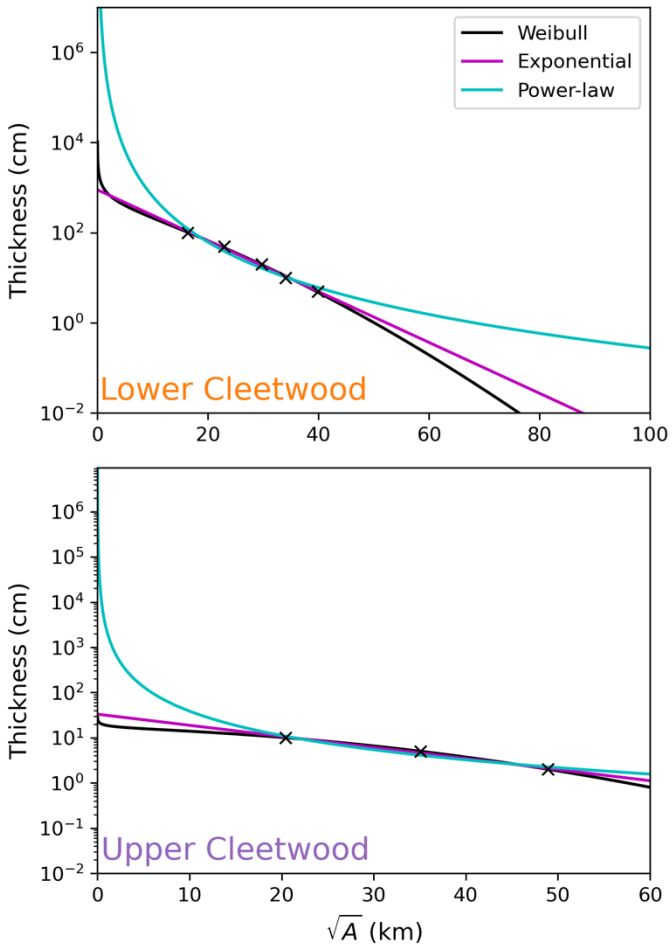

Figure 8. (A-B) Semi-log plots of the thickness of a deposit as a function of the square root of the isopach area and exponential, power-law, and Weibull best fit deposit thinning trends for the lower and upper Cleetwood units, respectively. See Table 1 for fitting parameters, Pearson correlation coefficients (r^2), and erupted volumes (non-DRE).

the best fit approach, being 1.01±0.19 km^3 for the lower Cleetwood, and 0.21±0.03 km^3 for the upper Cleetwood. These results confirm that the lower Cleetwood unit is the most voluminous out of all the phases of the Cleetwood eruption. It is, on its own, close to a VEI 5 eruption.

The upper Cleetwood units lacks sufficient field constraints to confidently draw isopleth lines for Maximum Lithic (ML) sizes > 0.8 cm (Figure 4C, D), making it unreliable to use the *CS86* or *R2019* models to calculate a plume height. Consequently, plume height and MER results are presented only for the lower Cleetwood unit in Supplementary Table 2. Using *CS86* and averaging the plume heights calculated for the 5, 2, and 0.8 cm ML isolines gives H_t = 25±2 km with an average wind velocity of 27±3 m/s. Comparing this wind velocity with NCEP-DOE Reanalysis 2 (Kanamitsu et al., 2002) data for the entire year of 2020 at Crater Lake shows that this value is reasonable for this location (Supplementary Figure 3). Using this H_t and the model of Mastin (2014), the calculated MER for the lower Cleetwood is $(8.6 \pm 3.3)\times10^7$ kg s^{-1}. Using *R2019*, the more robust model of Rossi et al (2019), and averaging the plume heights calculated for the 5 cm and 2 cm ML isolines for eruptive scenarios 2 (intermediate intensity) and 3 (high intensity; see Rossi et al., 2019), gives a plume height of 19±2 km. Given the inadequacies of these models to capture features such as partial column collapse or gravitational fountaining, a large degree of

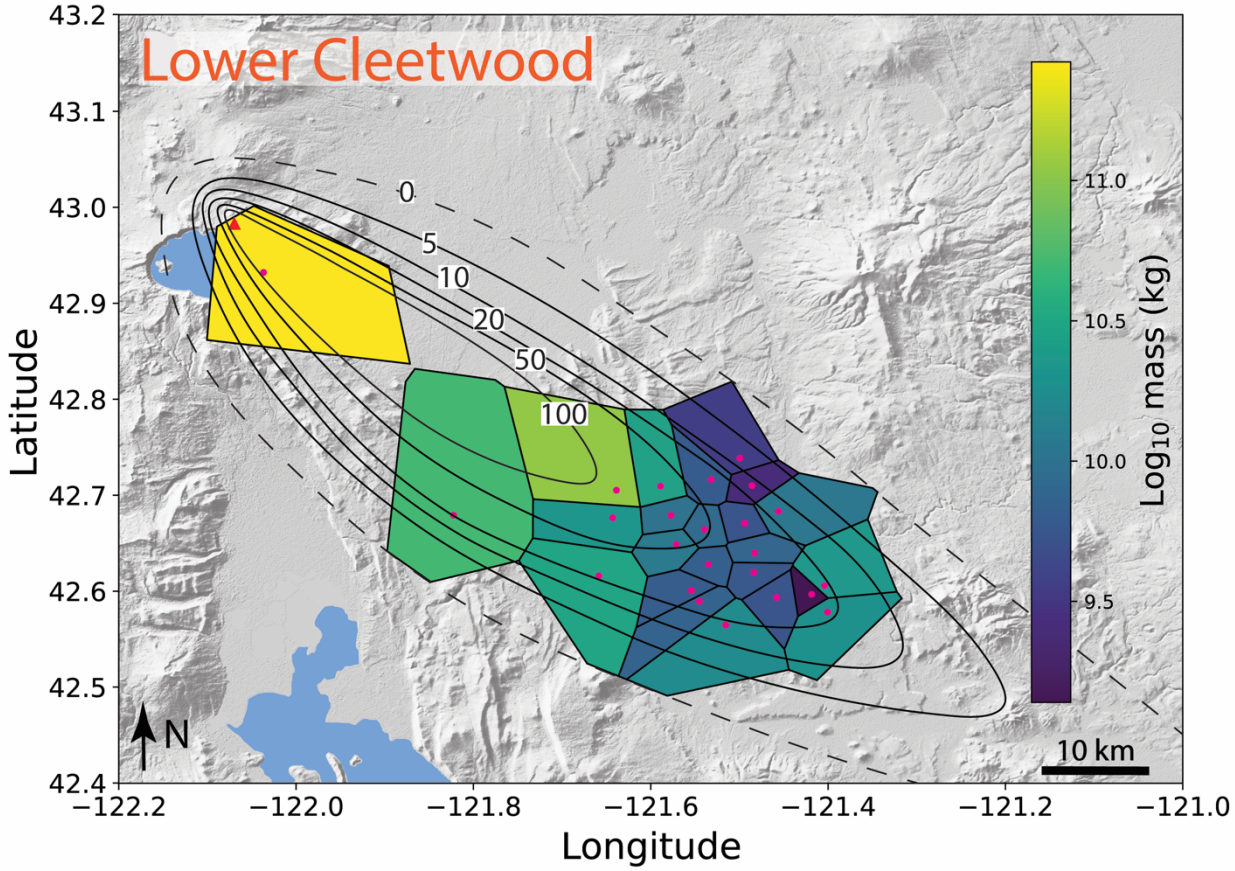

Figure 9. Voronoi tessellation of the lower unit of the Cleetwood eruptive sequence used to calculate the total grain-size distribution (TGSD). Pink dots indicate samples analyzed for their GSD via sieving and weighing. Isolines are in centimeters. Background is global earth relief (Tozer et al., 2019).

uncertainty is associated with their use. The uncertainty in the above calculated plume height of 2 km falls in line with the ~10% error for strong plumes as determined via the results of a model intercomparison study conducted by Costa et al. (2015). Using this plume height and the model of Mastin (2014), the calculated MER for the lower Cleetwood unit is $(3.1 \pm 1.0)\times10^{7}$ kg s^{-1}.

As the upper Cleetwood was not present at enough investigated locations within its respective dispersal area, the TGSD could not be confidently calculated. The TGSD of the lower Cleetwood, calculated using the Voronoi tessellation method of Bonadonna and Houghton (2005) (Figure 9), exhibits a power-law relationship, $N{>}d = \lambda d^{-D}$, where N is the number density of particles, d is the equivalent diameter, λ is a scaling factor, and D is the power-law exponent, or fractal dimension. Best-fitting the TGSD using the least-squares method gives fractal dimension (D) values of 3.0 ($r^2 = 0.997$), 3.1 ($r^2 = 0.997$), and 3.2 ($r^2 = 0.998$) when fitting grain-

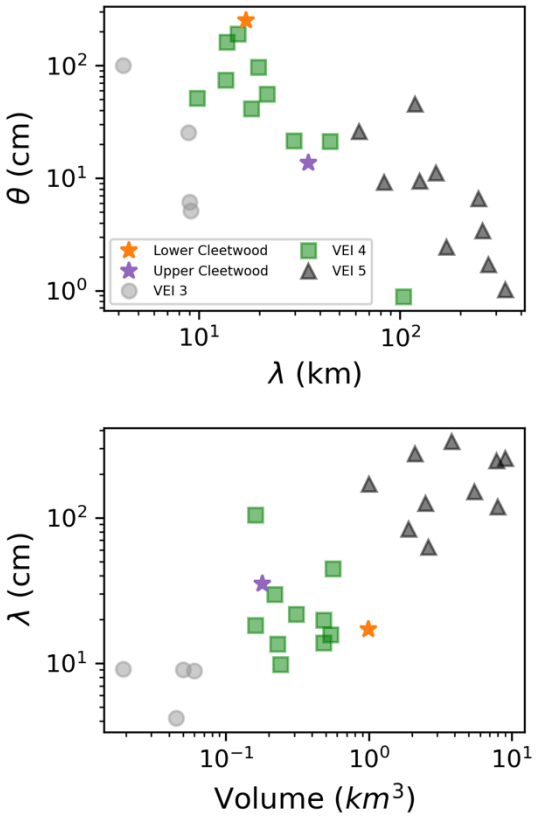

Figure 10. Best fit Weibull parameters for the two phases of the Cleetwood eruptive sequence plotted together with VEI 3, VEI4, and VEI 5 eruptions compiled by Bonadonna and Costa (2012). **(A)** θ versus λ. **(B)** λ versus total erupted volume (non-DRE). In both graphs, note that all phases of the Cleetwood eruptive sequence plot with other VEI 4 eruptions.

sizes ≥ 0.5 mm, ≥ 1 mm, and ≥ 2 mm, respectively. The rationale for only fitting values above 0.5-2 mm is discussed in detail below.

5 Discussion

5.1 The Cleetwood Eruptive Sequence

Our results show that the ~7.7 ka Cleetwood eruptive sequence of Mount Mazama consisted of two distinct and consecutive VEI 4 eruptions. Bonadonna and Costa (2012) plotted the relationship between the best fit Weibull parameters θ and λ, along with the total erupted volume derived from their Weibull method for a variety of eruptions ranging from VEI 1 to VEI 6. When plotted together with these data, all phases of the Cleetwood eruption clearly group with other historic VEI 4 eruptions (Figure 10).

With an erupted volume of 0.98±0.01 km^3, the lower Cleetwood straddles the line between a VEI 4 and VEI 5 eruption and is sub-Plinian following the classification of Bonadonna and Costa (2013, see Supplementary Figure 4). Its deposit is characterized by a strong normal grading, which indicates that both plume height (~19 km) and MER (~3.1×10^7 kg s^{-1}) reached a maximum at the beginning of this phase and continuously waned after that. The base of the lower Cleetwood unit appears relatively abundant in lithics in the field (5-10 vol.% of 1-4 mm, see Figure 6). We agree with Young's interpretation that this relative abundance of lithics at the onset of the Cleetwood eruption is the result of conduit/vent clearance. Young's (1990) volume estimate for the lower Cleetwood is 1.15 km^3 compared to our value of 0.98±0.01

km^3. Our results thus slightly revise downwards the volume of this phase of the Cleetwood eruption.

Comparing ML measurements of both the lower and upper Cleetwood units (Figure 4C, D) shows that MLs for the upper are only slightly smaller than those of the lower at the same location. This suggests that both plume height and MER are only slightly less than the lower Cleetwood unit, although the erupted volume is about five times smaller. The deposit of the upper Cleetwood is characterized by a strong reverse grading that suggests an increase in column height and MER with time, likely due to erosional vent widening (Wilson et al., 1980; Carey and Sigurdsson, 1989; Rosi et al., 1999). This vent widening is supported by a slight increase in the proportion of lithics from 3 vol.% to 5 vol.% from the lower to the upper unit. Another defining characteristic of the upper Cleetwood unit is the drastic increase in obsidian pyroclasts, which makes up to 23 vol.% of size fraction 0.125-0.25 mm. Young (1990), Bourgeois (1998), and Wearn (2002) all attributed this increase in obsidian pyroclasts towards the end of the Cleetwood eruption to the progressive annealing of juvenile glass to the conduit walls, which is then mostly eroded during this final explosive phase. Gardner et al. (2017) and Watkins et al. (2017) showed that obsidian pyroclasts from the North Mono Craters (CA, USA) formed by the syn-eruptive agglomeration and sintering of ash fragments on the conduit walls above the level of fragmentation, which were then remobilized over a wide range of depths and ejected together with juvenile porous pyroclasts. Wadsworth et al. (2019) showed that in the absence of a confining pressure, the timescale for sintering decreases with decreasing particle radius. We propose that ash fragments begin to sinter and weld to the conduit walls during the emplacement of the lower Cleetwood unit. As the MER wanes during the lower unit, as evidenced by the strong normal grading of that phase, sintering and welding dominate over erosion and ejection. This continues until the end of the lower Cleetwood unit and perhaps even partially seals the conduit (Wadsworth et al., 2020), which in turn repressurizes the system and may trigger the beginning of the upper Cleetwood. As the MER increases over the course of the upper Cleetwood, erosion begins to dominate over agglomeration and sintering, leading to an increase in both obsidian pyroclasts and lithics in the deposit of the upper Cleetwood unit. It should be noted that layer 5F (Figures 5 and 7), from which we determined componentry of the upper Cleetwood, does not lie directly on the dispersal axis of the upper unit and therefore probably

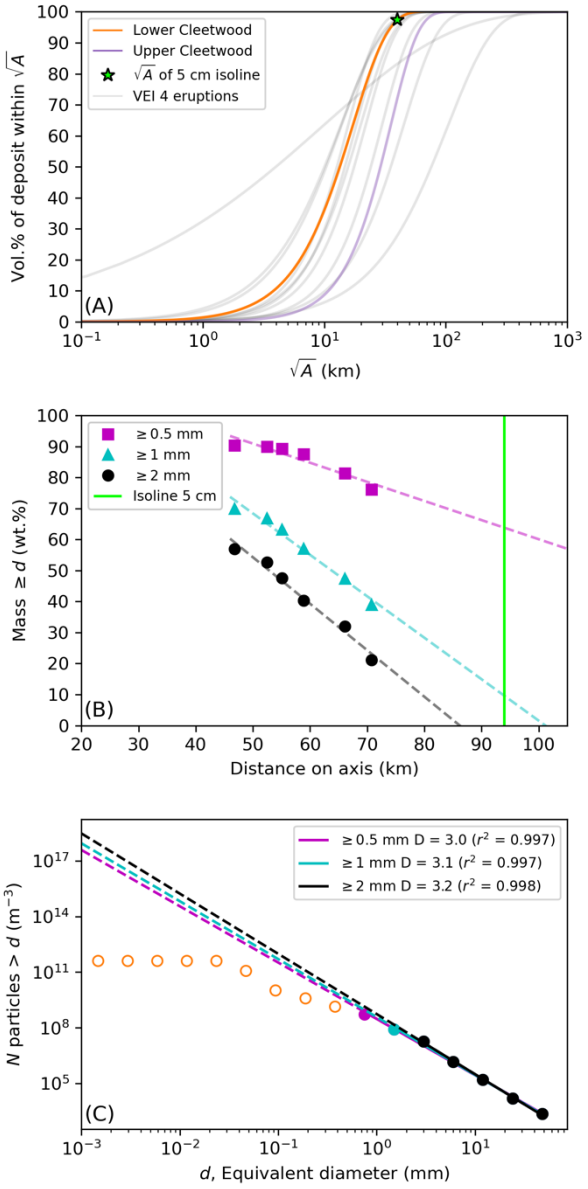

Figure 11. (A) Cumulative volume of tephra of the lower unit of the Cleetwood eruptive sequence as a function of the square root of the isopach area, $\sqrt{A}$ (km). Data for all other VEI 4 eruptions compiled by Bonadonna and Costa (2012) are also plotted, in gray, for comparison. **(B)** Mass fraction (in wt.%) of particles ≥0.5 mm, ≥1 mm, or ≥2 mm as a function of the distance from the vent along the dispersal axis of the lower Cleetwood unit. The vertical green line represents the furthest extent of the 5 cm isoline (Figure 4B). Because all locations plotted lie on the dispersal axis, the mass ≥ d for each grain-size likely represents maximum values. (**C**) Cumulative number density, $N > d$, versus equivalent diameter, d, for lower unit of the Cleetwood eruption (i.e., TGSD) and best fits obtained using a power-law distribution for all particles ≥0.5 mm, ≥1 mm, and ≥2 mm. The fractal dimension and Pearson coefficient obtained for each case are given in the legend.

represents minimum abundances of dense component (lithic, pyroclastic obsidian), when compared with those from the lower Cleetwood.

Judging solely from the contact between the lower and upper Cleetwood, it is difficult to say whether these two phases correspond to two distinct plumes or if the upper Cleetwood simply marks an increase in plume height and MER from the end of the lower Cleetwood, due to vent widening. The thin grey ash layer making contact between the lower and upper Cleetwood units shows no visible signs of erosion. Thus, if a separate plume is responsible for the

deposition of the upper unit, it occurred shortly after the end of the emplacement of the lower Cleetwood. Furthermore, this grey ash layer is only present at SE medial locations, which indicates that the dominant wind shifts from the SE to ESE by the end of the lower Cleetwood, when plume height and MER were at a maximum.

5.2 Comparison with Modern Equivalents

Although there are many historic examples of highly silicic eruptions that transitioned from explosive to effusive activity within the same eruptive sequence (e.g., the 1060 CE Glass Mountain eruption of Medicine Lake volcano, California, USA, Heiken, 1978; the 700 CE Big Obsidian Flow eruption at Newberry Volcano, Oregon, USA, Kuehn, 2002), the rhyolitic eruptions of Chaitén (2008, Chile; Alfano et al., 2011b) and Cordón Caulle (2011-2012, Chile; Pistolesi et al., 2015) provided the first real-time observations of an eruption of this type in modern history. The 2008 eruption of Chaiten consisted of a series of VEI 4 eruptions that began on May 1 with a ~0.5 km^3 explosive phase (Watt et al. 2009; Alfano et al. 2011b; Durant et al., 2012) and climaxed on May 6th with a sub-Plinian eruption that ejected ~0.3 km^3 of tephra from a 19±1 km high plume (Carn et al. 2009; Alfano et al. 2016), which corresponds to a MER of ~2.8×10^7 kg s^{-1} (Mastin, 2014). On May 11, the explosive activity began transitioning to effusive activity that eventually emplaced a ~0.8 km^3 rhyolitic flow (Pallister et al., 2013). The 2011-2012 eruption of Cordón Caulle can be divided into four explosive phases, two of which being classified as VEI 4 eruptions. The first and most intense sub-Plinian phase began on June 4 and deposited ~0.75 km^3 of tephra from a ~11-14 km plume and MER on the order of 10^7 kg s^{-1}. The second phase (5-6 June) fluctuated with MERs of 10^6-10^7 kg s^{-1} and deposited ~0.21 km^3 of material ending with the deposition of an obsidian-rich tephra layer. The third and fourth phases (June 7 and later) consisted of VEI 3 eruptions depositing a total of ~0.05 km^3 of tephra (Bonadonna et al., 2015; Pistolesi et al., 2015). Effusive activity began on June 15 from the same vent and produced a ~0.6 km^3 rhyolitic flow (Castro et al., 2013; Jay et al., 2014; Bertin et al., 2015). Calculated volumes, plume height, and MER for the Cleetwood eruptive sequence are like these two modern analogs, and we thus infer that the Cleetwood eruption unfolded in a manner and timing similar to that of these Chilean eruptions; explosive lower and upper Cleetwood units, all occurred within a period of days, followed, days/weeks later, by the emplacement of the

rhyodacitic Cleetwood Flow from the same vent, perhaps interspersed by hybrid explosive-effusive activity (Schipper et al., 2013).

5.3 Grain-Size Distribution

5.3.1 TGSD of the Cleetwood eruption

Exhaustive sample collection and grain-size data for the Cleetwood deposit are difficult to obtain due to the extreme thickness of the overlying Climactic deposit at proximal locations, and difficulties in distinguishing the Cleetwood from the Climactic deposits at distal locations. The TGSD of the lower unit of the eruption, the only phase for which we believe we have enough data to calculate an accurate TGSD, was thus constructed using samples collected at 24 locations 6-72 km from the vent. All the points used to build the TGSD are within the 5 cm isoline (Figure 9) and, given the density of data obtained within this area, we believe the TGSD built using the Voronoi tessellation is representative of the material deposited within that 5 cm isoline. Using the Weibull model of Bonadonna and Costa (2012), the volume of deposit enclosed within the 5 cm isoline can be calculated using

$$V(x) = \frac{2\theta\lambda^2}{n}\left[1 - e^{-(x/\lambda)^n}\right] \quad (1)$$

where x (km) is the square root of isopach area for isoline 5 cm, λ (km) is the characteristic decay length scale of deposit thinning, θ (cm) is a thickness scale, and n is a dimensionless shape parameter (λ, θ, and n are provided in Table 2). Using Eq [1], the volume enclosed by the 5 cm isoline is ~0.97 km^3, corresponding to about 97% of the whole volume of tephra ejected during the lower Cleetwood, consistent with other VEI 4 eruptions (Figure 11A). Furthermore, the proportions of pyroclasts ≥ 2 mm and ≥ 1 mm in samples of the lower Cleetwood unit collected along the main dispersion axis decrease downwind and reach 0% and <10%, respectively, when extrapolated to where the isoline 5 cm crosses the main axis of dispersion (at ~94 km, Figure 4B, Figure 11B). We thus infer that the TGSD calculated for the lower Cleetwood using medial data is representative of the whole TGSD for particles larger than ~1 mm. Over that range of sizes, the TGSD can be nicely fit using a power law distribution and a fractal dimension D = 3.1 (Figure 11C; D = 3.2 is obtained when fitting only particles ≥2 mm, and D = 3.0 for particles ≥0.5 mm).

In the absence of distal data in this study, it is impossible to accurately construct the TGSD for the lower unit of the Cleetwood eruption for particles ≤ 1 mm. However, compilations of TGSDs of >20 sub-Plinian and Plinian eruptions show that all can be fit using a single power law distribution over the whole range of particle sizes (~10^{-3}-10^{3} mm), with a fractal dimension D≥3 (see compilations in Kaminsky and Jaupart, 1998; Rust and Cashman, 2011). In particular, eruptions of silicic magma with MER similar to the lower unit of the Cleetwood eruption and ranging from 1.5×10^{7} kg s^{-1} to 7.9×10^{7} kg s^{-1} (MER for the lower Cleetwood is 3.1×10^{7} kg s^{-1}) have *D* values close to 3 (e.g., Phase D Askja 1875: *D*=3.0, Kaminsky and Jaupart 1998; Unit B 79 cal CE Mt. Pelée: *D*=3.0, Carazzo et al., 2020; Mt. St. Helens, May 18, 1980: *D*=3.1, Rust and Cashman, 2011; Layer β 2008 Chaitén: *D* = 3.0, Alfano et al., 2016). Given these observations, we speculate that the TGSD of the lower Cleetwood unit can be fit using a power law with a fractal dimension of ~3.1 over the whole range of particles sizes. As shown below, in the absence of distal data to construct the TGSD, we believe that individual high-resolution GSDs at medial locations on the dispersal axis can provide further insight into the fractal dimension of an eruption's TGSD.

5.3.2 High-Resolution GSDs

The high-resolution GSDs produced for individual locations do not equate to the whole TGSD of the deposit as they partly reflect transport processes (Pioli et al., 2019). Despite this, important information can still be gleaned from these individual GSDs. As seen in the results section above, all high-resolution GSDs in this study, regardless of the eruptive phase or sample location, show two systematic breaks in slope from a power-law relationship at ~0.125 mm and ~0.510 mm. These breaks in slope create three individual segments S1 (particles<0.125 mm), S2 (particles 0.125-0.510 mm), and S3 (particles >0.510 mm) that can all be fit by a power-law relationship with fractal dimensions *D1*, *D2*, and *D3* respectively. We discuss below the signification of each of these segments.

5.3.2.1 Particles <0.125 mm – Inheritance from Primary Fragmentation

Values of *D1* (Table 2; Supplementary Table 3) are 2.5±0.2 regardless of eruptive phase, distance from the vent, and location with respect to the dispersal axis. These values are within the range of those obtained by rapid decompression experiments (Kueppers et al., 2006). Particles are predominantly juvenile ash over the range of sizes covered by S1 (Figures 6-7), and

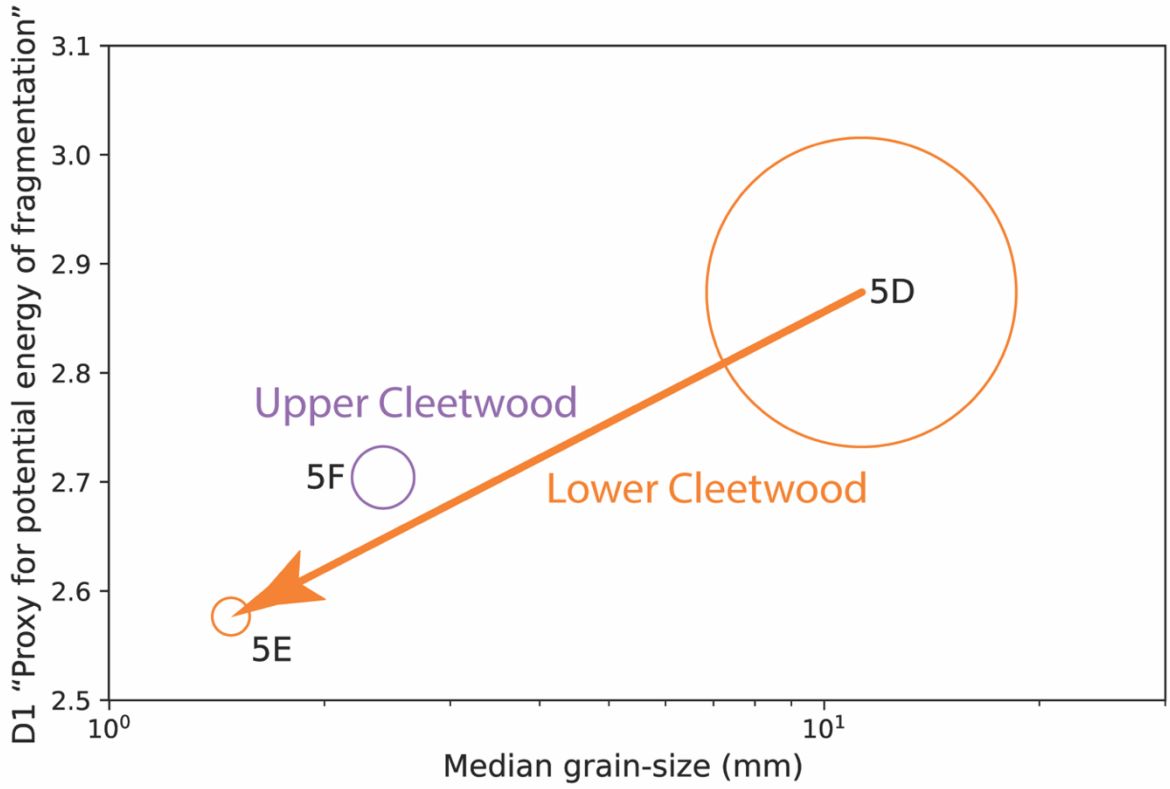

Figure 12. D1 values (i.e., fractal dimension of the cumulative size distribution of particles <0.125 mm) found for all Cleetwood units of Cltwd 5, plotted as a function of the median grain-size of that subunit. Circle size is representative of the inferred plume height and thus mass eruption rate (MER), being the highest but continuously decreasing (from 5D to 5E) for the lower Cleetwood, and intermediate for the upper Cleetwood.

thus the fractal dimension at these sizes is largely controlled by the size distribution of this component. Jones and Russel (2017) conducted pumice attrition experiments at varying time lengths and showed that a time ≥ 30 minutes was necessary to change the slope of the GSD for particles <0.156 mm, approximately equal to our S1 range. This timescale is far too long to represent transit time within the conduit after fragmentation (estimated to be of the order of 10^1-10^2 s for Plinian eruptions; Gardner et al., 1996), and Jones and Russel (2017) suggested that their longer experimental runs could represent residence times in the plume. However, the bulk ash concentration used in their experiments is ~4,000 $g.m^{-3}$, whereas measured concentrations in real plumes are three orders of magnitude lower (e.g., 3.6-4.9 $g.m^{-3}$ for the 1980 eruption of Mt. St. Helens; Harris and Rose, 1983). This suggests that the size distribution of particles within this size range only evolves slightly after initial magma fragmentation.

Giachetti et al. (2021) showed that some pumice lapilli from sub-Plinian and Plinian eruptions, including the Cleetwood eruption, are pumice agglomerates comprised of protopyroclasts, the products of primary magma fragmentation. These pumice aggregates are created by the agglomeration and partial sintering of protopyroclasts of all sizes as they collide during ascent in the conduit seconds after initial magma fragmentation. Giachetti et al. (2021) showed that the size distributions of 0.001-10-mm protopyroclasts from two sub-Plinian rhyolitic eruptions, the 1060 CE Glass Mountain eruption of Medicine Lake volcano (California, USA; Heiken, 1978) and the 700 CE Big Obsidian Flow eruption at Newberry Volcano (Oregon, USA; Kuehn, 2002), are power-law with *D* values of 2.5±0.1. These power-law exponents are consistent with those of the products of experimental magma fragmentation by rapid decompression (Kueppers et al., 2006). The *D1* values found in our study are also in the same range. Using the methodology developed by Giachetti et al. (2021), we analyzed the size distribution of protopyroclasts 1.5-30 μm in a pumice from the onset of the lower Cleetwood, collected at location Cltwd 5 (layer 5D, see Figure 5). Protopyroclasts were only analyzed for this narrow size range because outlining individual clasts at larger sizes in these Cleetwood pumices becomes too subjective. Indeed, Giachetti et al. (2021) suggested that the fluidization of packed beds of protopyroclasts immediately after fragmentation could be more efficient for eruptions with MERs $>10^7$ kg s^{-1} (e.g., the lower unit of the Cleetwood eruption), leaving less time for the mixing and amalgamation of protopyroclasts with highly contrasting textures, and thus making the boundaries between protopyroclasts less visually apparent. The size distribution of 3,011 protopyroclasts 1.5-30 μm in size analyzed in the pumice lapillus of the lower Cleetwood unit is best fit by a power-law with a *D* value of 2.7. Interestingly, the GSD of the lower Cleetwood is best fit by a power-law with $D1 = 2.6$ for particles <0.125 mm (Table 1).

Although further investigation is necessary, our results suggest that the fractal dimension of the GSD of particles <0.125 mm collected at medial locations on the dispersal axis of explosive deposits reflects the size distribution of the primary products of magma fragmentation in the conduit (i.e., like the distribution of protopyroclasts within pumice aggregates; Giachetti et al., 2021), and thus could be used to infer the potential energy at fragmentation. This hypothesis is supported by the fact that, at a given location, there is a positive correlation between the value of *D1* and the median grain-size (Figure 12).

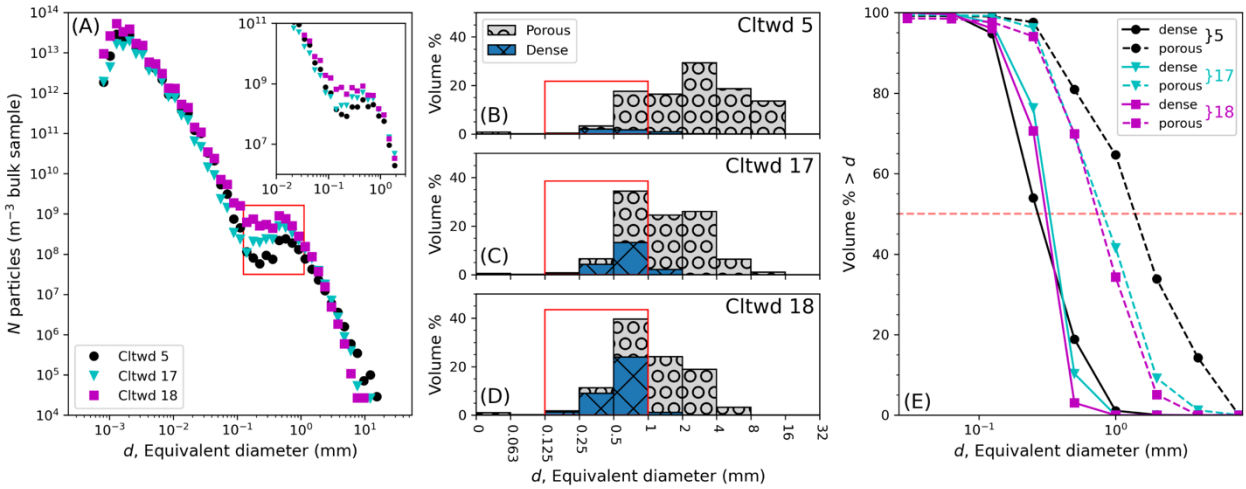

Figure 13. (A) Number density, *N*, versus equivalent diameter, *d*, for the end of the lower Cleetwood unit at locations Cltwd 5, 17, and 18, which are all located on the main dispersal axis at 46 km, 56 km, and 66 km from the proposed vent location, respectively. Note the sudden increase in number density of particle for ~0.1 mm<*d*<~1 mm (red rectangle). Inset shows *N* versus *d* using laser diffraction data only and further illustrate that this increase is not an artifact of merging datasets (see also Figure 3B). **(B-D)** Volume percent of porous and dense material versus *d* for locations Cltwd 5, 17, and 18, respectively. Note the increase of the proportion of dense particles in size range 0.125-1 mm with increasing distance from the vent (red rectangles). **(E)** Cumulative volume distribution for porous (dashed lines) and dense (solid lines) material at Cltwd 5, 17, and 18. Median grain-sizes are at the intersections of these distributions with a volume percent of 50% (i.e., horizontal red dashed line). Note the slight increase in the median diameter of dense particles from Cltwd 5 to Cltwd 17 and 18, which we attribute to particle rafting, whereas the median diameter of the porous particles logically decreases with increasing distance from the vent.

5.3.2.2 Particles 0.125-0.510 mm – Clues for Rafting During Transport

The second portion of the individual GSDs, S2 (particles 0.125-0.510 mm), can also be fit with a power-law giving D2 values of 0.6±0.1. This fractal dimension does not vary systematically with explosive phase, distance from the vent, nor location with respect to the dispersal axis (Table 1). This size fraction shows a noticeably higher proportion of non-juvenile components (i.e., loose crystals and lithics) compared to S1 and S3 (Figure 7). These components are not the primary products of fragmentation and thus this enrichment could be a contributing factor to where and why this break in slope with S1 occurs. A recent theoretical study suggests that particle rafting can modify the way in which some particles locally sediment (Rossi et al., 2021). Rafting occurs when fine particles aggregate around a relatively dense core particle during transport. The resulting aggregate has a density significantly lower than its core

due to the air entrapped in between aggregating particles. This leads to relatively dense particles 'rafting' and landing further than where they would have if smaller particles had not aggregated around them. Upon impact and over time these aggregates break apart and are rarely found intact when sampling historic eruptions. In their theoretical framework, Rossi et al. (2021) defined the size range of core particles that could undergo rafting as 0.138-0.710 mm, which mostly overlaps with the range of sizes over which we see major changes in the shape of our GSDs. Note that this transport process changes the individual GSDs at some locations, but not the overall TGSD of the eruption.

To investigate whether particle rafting may have occurred during the Cleetwood eruption and if this process can explain part of the shape of our GSDs, we analyzed the size distribution of the porous (pumice and banded pumice) and dense (obsidian pyroclasts, lithics, and loose crystals) components of a single layer at increasing distance from the vent, along the main axis of dispersion. Layers 5E, 17D, 18B (Figure 5) all correspond to the end of the lower Cleetwood and are located on the main dispersal axis at 46 km, 56 km, and 66 km from the proposed vent location, respectively. All three locations show an unexpected increase in particle number density over the size range ~0.125-0.650 mm (Figure 13A), which is not related to data combination as the same observation is made using laser diffraction data alone (see inset in Figure 13A). As expected, the overall median grain-size decreases with distance from the vent as the GSDs of 5E, 17D, and 18B skew towards finer particle sizes due to density sorting during transport in the plume (Figure 13B-D). However, the componentry (realized on sieved fractions independently of laser diffraction and DIA analyses), shows that the proportion of dense particles that compose the size fraction in which we see an increase in particle number density simultaneously increases from 4% at 46 km from the vent, to 18% at 56 km, and finally to 34% at 66 km (i.e., from Cltwd 5, Cltwd 17 to Cltwd 18, respectively). Furthermore, this increase in the volume percent of dense components is accompanied by an increase in the median grain-size of the dense particles as a function of distance, from ~0.27 mm at Cltwd 5 to ~0.31-0.33 mm at Cltwd 17 and 18, which is not expected (Figure 13E). We infer that this increase in both the proportion and the median grain-size of dense particles with distance from the vent are clues that particle rafting delayed their sedimentation (Rossi et al., 2021).

5.3.2.3 Particles >0.510 mm – Influence of Sedimentation

This portion of the GSD, which corresponds to particles >0.510 mm, is predominantly composed of juvenile pumice (Figure 7). For all layers of all units, it can be nicely fit with a power-law equation with a fractal dimension *D3* between 2.7 and 4.7. For a given unit, the value of D3 increases with distance from the vent along the main dispersion axis, testifying to a progressive loss of larger particles. For example, for the lower Cleetwood unit, *D3* is equal to 2.95 at ~46 km from the vent (Cltwd 5), increasing to 3.10 at ~56 km (Cltwd 17), and to 3.32 at ~66 km (Cltwd 18). At these three locations, particles ≥ 0.5 mm (approximately the lower bound of *D3*) represent >80% of the mass of the sample, and it is thus not surprising that these *D3* values (~3.1±0.2) are close to the fractal dimension of the calculated TGSD for particles > 0.5 mm (3.0, see Figure 11C).

6 Conclusion

The successful modeling and forecasting of the dispersion and sedimentation of tephra from explosive volcanic eruptions rely heavily on the initial eruption source parameters inputs such as plume height, erupted volume, MER and Total Grain-Size Distribution. During an eruption these parameters are challenging to determine and depend on those derived from detailed field studies of similar historic events. Here we calculated eruption source parameters for the ~7.7 ka Cleetwood eruption of Mount Mazama (Crater Lake/giiwas, Oregon, USA). We applied a novel approach to produce high-resolution grain-size distributions over the range 0.00035-35 mm by combining laser diffraction and dynamic image analysis techniques.

The ~7.7 ka Cleetwood eruptive sequence of Mount Mazama consisted of two consecutive VEI 4 eruptions: the lower and upper Cleetwood units, from oldest to youngest. The lower Cleetwood was the most intense (Ht = ~19 km; MER = ~3.1×10^7 kg s^{-1}) and voluminous (~0.98 km^3) of the sequence with a TGSD that can be fit with a fractal dimension of ~3.1. Altogether, the Cleetwood eruption deposited 1.10 km^3 (non-DRE) of tephra from at least one, but no more than two, separate plumes. Explosive activity then transitioned to an effusive stage, with no apparent break, extruding a rhyodacitic lava flow with a minimum volume of ~0.6 km^3. The continuity and deposit of the Cleetwood eruption of Mount Mazama is similar to the only two witnessed volcanic eruptions of rhyolitic magma that transition to an effusive phase: Chaitén (Chile, 2008; fall = ~1 km^3, flow= ~0.8 km^3, plume height = ~19 km) and Cordón Caulle (Chile,

2011-2012; fall = ~0.8 km^3, flow = ~0.8 km^3, plume height = ~14 km). Further detailed fieldwork in proximal deposits of the upper unit of the Cleetwood eruption would be necessary to resolve whether there was coeval (hybrid) effusive and explosive activity as suggested by observations at Cordón Caulle during the 2011-2012 eruption.

Regardless of the eruptive phase or sample location, all high-resolution cumulative GSDs show two systematic breaks in slope from a power-law relationship at ~0.125 mm and ~0.510 mm, creating three individual segments that can all be fit by power-law relationships. We show that in conjunction with eruption source parameters and detailed componentry, our high-resolution GSDs provide insight into magma fragmentation and tephra transport. We show that the fractal dimension for particles <0.125 mm from medial locations on the dispersal axis of the tephra deposit reflects the size distribution of the primary products of magma fragmentation, and thus could be used to infer the potential energy at fragmentation. This observation is further supported by the positive correlation between the D1 value and the median grain-size at a given location. The overall low slope of the GSD for particles 0.125-0.510 mm is due to an increase in the amount of dense components (obsidian pyroclasts, lithics, and loose crystals) that is accompanied by an increase in their median grain-size with distance. We infer that this is due to particle rafting and thus delayed sedimentation. Lastly, the increasing slope of the GSDs for particles >0.510 mm with increasing distance from the vent, reflects the progressive and rather rapid loss of coarse ash and lapilli in the medial portion of the deposit. Our comparison of high-resolution GSDs across a fallout deposit has potential for identifying processes that modify tephra dispersal and sedimentation, such as particle rafting. Newly gleaned information using a higher resolution of GSDs would greatly further our understanding of both primary and secondary eruptive processes and help constrain eruption modeling and hazard assessment in the future.

CHAPTER III

COMBINING FIELD OBSERVATIONS AND TEPHRA DISPERSAL MODELLING TO EVALUATE ERUPTION SOURCE PARAMETERS OF HISTORIC ERUPTIONS: A CASE STUDY FROM MOUNT MAZAMA (OREGON, UNITED STATES)

From Wiejaczka J and Giachetti T (in prep.). Combining Field Observations and Tephra Dispersal Modelling to Evaluate Eruption Source Parameters of Historic Eruptions: A Case Study from Mount Mazama (Oregon, United States). *Bulletin of Volcanology.*

1 Introduction

Tephra fallout during volcanic eruptions presents a wide range of hazards that can have significant impacts on human health, infrastructure, and the environment. The physical hazards of tephra fallout include the potential for injury or fatality due to direct interaction with falling volcanic fragments. Larger tephra fragments can cause blunt trauma, while smaller particles can lead to eye and respiratory irritation by penetrating deep into the respiratory system, exacerbating preexisting conditions and/or causing new respiratory distress (Baxter, 2005). Tephra accumulation also poses risks to infrastructure, including the collapse of roofs and structures under the weight of volcanic ash, which is compounded when it becomes wet (Blong, 1984). The agricultural sector is also vulnerable to tephra fallout, as the latter can damage crops, contaminate water sources, and hinder photosynthesis by blocking sunlight (Wilson et al., 2012). These hazards highlight the importance of the accuracy of Volcanic Ash Transport and Dispersal Models (VATDMs), which are used for real-time forecasting and probabilistic hazard assessments of tephra fallout.

VATDMs use either a Lagrangian particle tracking numerical approach (e.g., Puff; Searcy et al., 1998; HYSPLIT, Draxler and Hess, 1998), a Eulerian advection-diffusion numerical approach (e.g., Ash3d, Schwaiger et al., 2012; NAME, Jones et al., 2007; Fall3D, Folch et al., 2009), or a Eulerian advection-diffusion analytical approach such as Tephra2 (Bonadonna et al., 2005; Connor and Connor 2006; Volentik et al., 2009; Biass et al., 2016). While these models consider different secondary variables such as topography, particle shape, wet/dry particle aggregation, and have diverse options for how the erupted mass is distributed in the plume (i.e., point source, line source, umbrella cloud, etc.), all rely on detailed field studies of analogous eruptions to provide constraints on both the primary input Eruption Source Parameters

(ESPs) and the output of the model. The ESPs include the erupted mass, plume height (H_t), and the Total Grain-Size Distribution (TGSD) of particles ejected into the atmosphere. Particularly difficult to constrain is the TGSD, which is crucial for accurate forecasts. The TGSD affects the distribution of particles within the plume and, in turn, modulates the location and timing of when a particle will be deposited. In situ measurement of TGSD during an eruption prove difficult (Scollo et al., 2005; Gouhier and Donnadieu, 2008; Bonadonna et al., 2011; Kozono et al., 2019; Freret-Lorgeril et al., 2019), especially for high-flux, large plume eruptions. Moreover, constructing a TGSD from historic events is often complicated due to poor deposit exposure and preservation (Costa et al., 2016; Pioli et al., 2019).

The dependence of VATDMs on ESPs from analogous historic eruptions becomes more problematic when, for a given type of ongoing eruption, the catalog of similar, historically observed events is limited. An example of these eruptive scenarios is that of rhyodacitic to rhyolitic eruptions that transition from explosive to effusive activity. Although many of these deposits have been identified in the historic record, such as the 1060 CE Glass Mountain eruption of Medicine Lake volcano (Heiken, 1978) or the 700 CE Big Obsidian Flow eruption at Newberry Volcano (Kuehn, 2002; Trafton and Giachetti, 2022), the only direct observations of this behavior are from recent eruptions at two Chilean volcanoes; Chaitén in 2008 (Castro et al., 2009) and Cordón Caulle in 2011-2012 (Pistolesi et al. 2015; Schipper et al., 2013). The ~7.7 ka Cleetwood eruption of Mount Mazama (Crater Lake/giiwas, Oregon, United States) appears to also be one such silicic eruption that has transitioned from explosive to effusive activity (Young 1990). The Cleetwood eruptive sequence consisted of two consecutive VEI 4 eruptions, the lower and upper Cleetwood units. The lower Cleetwood unit is the first and main phase, with a tephra volume close to 1 km^3 and thus a VEI close to 5 (Young 1990; Wiejaczka and Giachetti 2022). After the upper Cleetwood phase, the eruptive activity transitioned to an effusive stage, producing a rhyodacitic flow with a minimum volume of ~0.6 km^3 (Bacon, 1983). This eruption was soon followed by the climactic caldera-forming eruption, which was one of the largest of the Holocene Epoch (60 km^3 DRE; Bacon, 1983; Buckland et al., 2021), pointing towards the Cleetwood eruptive sequence as potentially key in destabilizing a much larger magmatic system.

In this study, we first re-evaluate the field-derived ESPs (H_t, TGSD, and erupted mass) for the lower Cleetwood by adding new field data to those of Young (1990) and Wiejaczka and Giachetti (2022). Next, we use these field-derived ESPs, a large collection of wind profiles, and

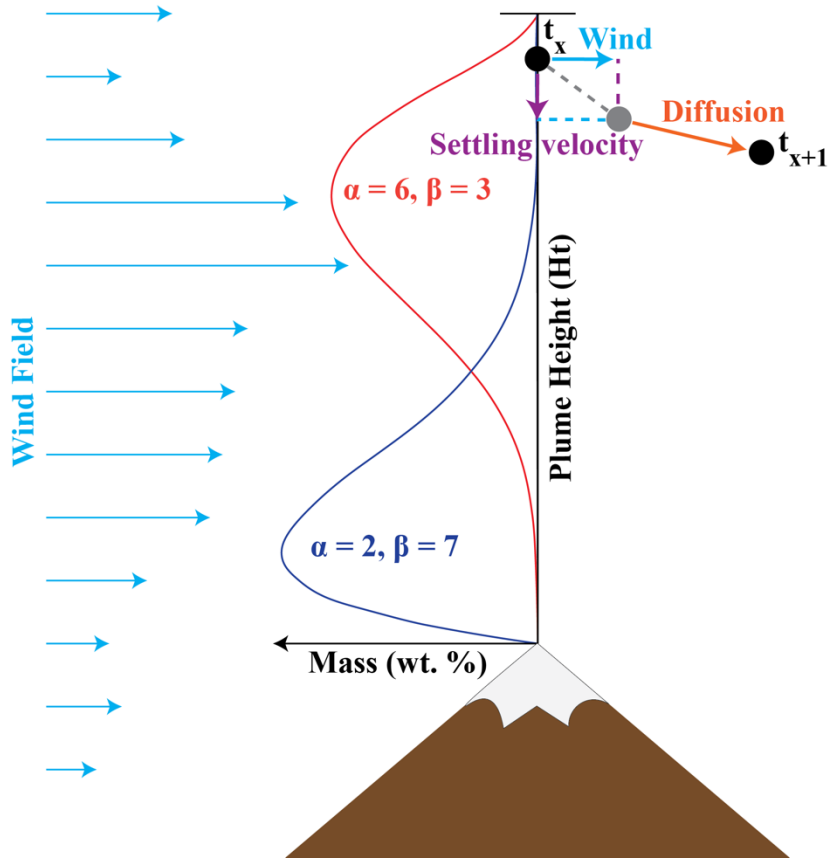

Figure 1. Schematic showing how Tephra2 operates. First, particles are released instantaneously from a plume located directly above the vent along a single vertical line and begin to fall through a layered atmosphere. Each particle's trajectory is then modified by the wind velocity and heading of each layer, and further by atmospheric diffusion. Particles are distributed within the plume using the equation $P(H_t) = \frac{(1-H_t)^{\beta-1} H_t{}^{\alpha-1}}{B(\alpha,\beta)}$ where H_t is plume height and $B(\alpha, \beta)$ is the beta function. Changing α and β in the beta function modifies the way in which mass is initially distributed within the plume.

a grid search approach in Tephra2 to explore the geometry of the lower Cleetwood plume and the diffusion characteristics of the tephra. We do so by minimizing the misfits between the model and both the mass load and the grain-size distributions obtained at 25 locations in the proximal and medial region of the fallout deposit. We demonstrate that comparing high-resolution grain-size distributions from individual locations with modeled outputs has the potential to give insight into the plume geometry for unwitnessed historic eruptions.

1.1 Tephra2

For a complete description, list of equations, and different versions of the Tephra2 VATDM, the reader is referred to Bonadonna et al. (2005; 2012), Connor and Connor (2006), Volentik et al. (2009; 2010), Biass et al. (2016), Constantinescu et al. (2021), and references therein, only the main points pertaining to this study being discussed here. We have chosen to use the Tephra2 VATDM because, as explained below, it solves the advection–diffusion equation analytically (Bonadonna et al., 2005), instead of numerically. This leads to much faster runtimes (~0.1-1 s per run on a single processor laptop) and allows for a broader exploration of plume and tephra diffusion characteristics. The fact that this model does not account for particle aggregation does not impact our results as this study focusses on the transport of particles ≤3 ϕ (0.125mm) where aggregation is believed to have a minimal impact on sedimentation (Rose and Durant 2011; Brown et al., 2012). The use of this model in the context of this study is also justified as the area of interest is within a 100 km of the vent location (Biass et al., 2016).

The Tephra2 VATDM solves the advection–diffusion equation analytically to determine the final mass per unit area (i.e., mass load, in kg/m^2) and grain-size distribution (in wt.%) of a tephra fall on the ground at points (x, y) within a 2D modeled space. Particles are released instantaneously from a plume located directly above the vent and fall through a layered atmosphere. A particle's trajectory is modified by the wind velocity of each layer, and further by atmospheric diffusion (Fig. 1). Particles are assumed to be spherical and have a size-dependent density. Their settling velocity is determined by their Reynolds number (see Bonadonna et al., 1998 for details).

Tephra2 requires the user to provide 1) the eruption source parameters, 2) a density versus size model, and 3) a 1D wind field in which both speed and direction vary with elevation (Tephra2 does not account for horizontal and temporal heterogeneities in the wind). The ESPs include plume height (H_t), erupted mass, and the total grain-size distribution (TGSD). Here we use the modified version of Tephra2 of Biass et al. (2016, TephraProb), which allows the user to provide a custom TGSD, as opposed to a Gaussian TGSD based on median grain-size and standard deviation. The user is also required to provide parameters that control the initial vertical mass distribution within the plume via a beta function with variables α and β (Fig. 1). When $\alpha < \beta$, mass is shifted towards the base of the plume,

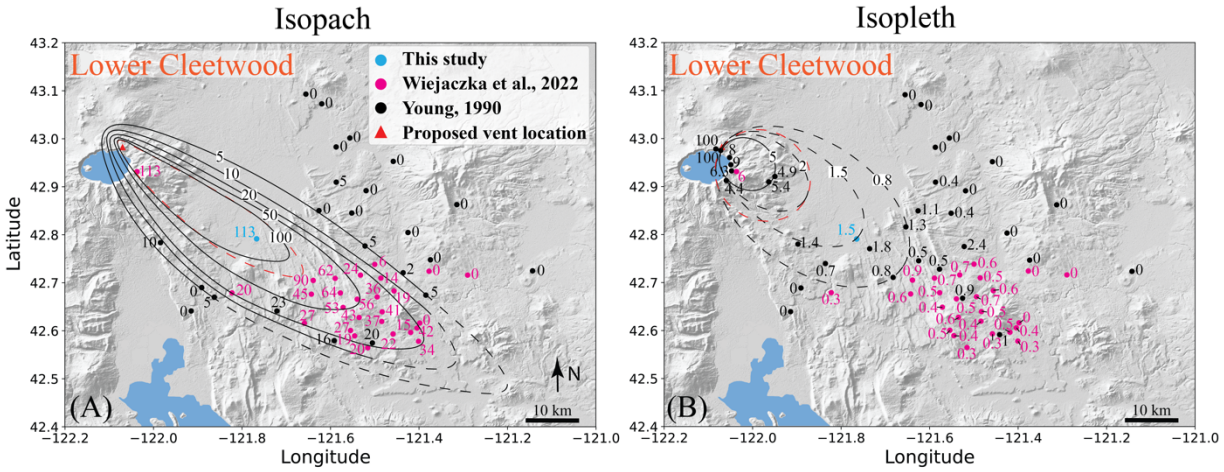

Figure 2. (A) Isopach map for the lower Cleetwood unit. **(B)** Maximum lithic (ML) isopleth map for the lower Cleetwood unit. All isolines are notated in centimeters and dashed red isolines represent the original lines from Wiejaczka and Giachetti (2022). Background is global earth relief (Tozer et al., 2019).

whereas the opposite occurs when $\alpha > \beta$. If $\alpha = \beta = 1$, the beta function becomes linear, and mass is distributed equally along the vertical axis. Both α and β are greater than zero, with values presented in the literature never exceeding 10 (Bonadonna et al., 2010; Elissondo et al., 2016).

Finally, a user-input diffusion coefficient (DC, in m^2/s) and fall time threshold (FTT, in s) are used to control how particles diffuse in the atmosphere. Diffusion of particles is size dependent and governed by a linear diffusion until the time exceeds FTT, at which point a power law diffusion is used (Bonadonna et al. 2005; Suzuki 1983). The latter is partly controlled by the eddy diffusivity constant (0.04 m^2/s; Suzuki, 1983). Values presented in the literature for DC and FTT cover orders of magnitude, ranging from ~10^2-10^5 m^2/s and ~3×10^2- 3×10^4 s, respectively (e.g., Bonadonna et al., 2010; Volentik et al., 2010; Johnston et al., 2012; Biass et al., 2016).

If the ESPs and the density model are usually derived from field data, values for α, β, DC, and FTT are typically determined via inversion. In the Methods section, we describe how the ESPs, the density model, and the wind fields were obtained for this study. We also describe how we compare the results of the model with field-derived data.

2 Methods

2.1 Field

The samples used in this study are those collected by Wiejaczka and Giachetti (2022). An additional pit was dug in 2022 (42.792344, -121.765731) approximately 32.5 km southeast from the supposed vent, on the main dispersal axis of the lower Cleetwood tephra fall deposit (Fig. 2). At this location, below 3.4 m of tephra from the climactic phase of the Mazama eruption, the Cleetwood deposit was divided into the lower and upper Cleetwood units based on changes in grain-size and grading. Each unit was then measured, photographed, and several kilograms of each unit were collected for analysis.

2.2 Deposit Density and Mass Load

Deposit density for each location was calculated by pouring bulk samples into a graduated cylinder and measuring both the mass and volume of the sample. Where samples were divided into subunits, the thickness fraction of each subunit collected was used as a weight to calculate the whole lower Cleetwood deposit density at that location. The mass load for each location was then calculated by multiplying it's the thickness measured in the field by the deposit density measured in the lab. The mass load of the whole deposit was obtained by averaging the density of all twenty-five locations.

2.3 Erupted Volume

The isopach map of the lower Cleetwood (Fig. 4A from Wiejaczka and Giachetti, 2022) was updated and the 100 cm isoline, the only that required modification following the addition of the new sample location described above, was redrawn using Adobe Illustrator (Figure 2A). The area enclosed within individual isolines was calculated using the image processing package Fiji (ImageJ, Schindelin et al., 2012). The lower Cleetwood tephra fall volume was then re-calculated with *TephraFits* (Biass et al., 2019) using the exponential, power-law, and Weibull models and the erupted mass was then determined by multiplying the volume by the average deposit density. For the power-law model, a distal integration limit of 90 km was used (i.e., the distance from the proposed vent to the tip of the 5 cm isoline).

2.4 Plume Height

The isopleth map of the lower Cleetwood (Fig. 4C from Wiejaczka and Giachetti, 2022) was updated: the 2 cm maximum lithic isoline was slightly altered and a 1.5 cm lithic isoline was added using Adobe Illustrator (Figure 2B) to include the additional data point. Downwind and crosswind distances were calculated using Fiji and the plume height, H_t (km) was then re-estimated using the models of Carey and Sparks (1986) and Rossi et al. (2019) herein referred to as CS86 and R2019, respectively.

2.5 High-Resolution Grain-Size Distributions

2.5.1 Individual Distributions

Individual high-resolution grain-size distributions (HR-GSDs) were determined following the sample preparation and methodology detailed in Wiejaczka and Giachetti (2022). The reader is referred to this paper for a full description of the methods used, only a summary being given here. After being dried, all samples were then dry-sieved every phi size from 5 to -6 (i.e., 0.031 mm to 64 mm). The volume and equivalent diameter of all particles >0.125 mm of all samples were then determined via dynamic image analysis (DIA) with a Microtrac PARTAN 3D particle size analyzer at the University of Oregon (Trafton and Giachetti, 2021; Wiejaczka and Giachetti, 2022). The volume of each particle is determined by multiplying its average length, width, and thickness and an equivalent diameter is calculated assuming a sphere of equal volume. Volume distribution of particles <0.125 mm was obtained for each size fraction by laser diffraction on a Beckman Coulter LS 13 320 at the USGS Cascades Volcano Observatory (Figure 2E; Blott et al., 2006; see also Wiejaczka and Giachetti, 2022).

Results of grain size analyses from both DIA and laser methods were then sorted in fifty-one regularly-spaced logarithmic bins from 12 to -6 phi (i.e., 0.2 μm – 64 mm). Due to laser diffraction data being given in volume percent as a function of equivalent diameter, each size fraction <0.125 mm was first converted to an actual volume using the mass of the size fraction (measured after sieving on a high-precision balance) and its bulk density measured using a Micromeritics AccuPyc II 1340 helium pycnometer at the University of Oregon. The two datasets were then merged to produce a continuous HR-GSD: we used laser diffraction data for size fractions <0.125 mm, and DIA data for size

fractions >0.125 mm. For locations where the lower Cleetwood deposit was divided into subunits, a HR-GSD was produced for each sub-unit and the HR-GSD of the whole lower Cleetwood at that location was obtained by averaging the sub-units HR-GSDs, using the thickness fraction of the subunits (i.e., thickness of the sub-unit divided by thickness of the whole lower Cleetwood unit) as weights. Note that the grain size distribution below 0.125 mm was measured by laser diffraction for only half of the samples. For the other half, a 'high-resolution' grain size distribution below 0.125 mm was interpolated from the sieve data of size fractions 0-0.032 mm, 0.032-0.063 mm, and 0.063-0.125 mm. This procedure, which greatly accelerates sample analysis, does not affect the results because 1) the <0.125 mm fraction represents only <4.2 wt% of each of these samples (except for Cltwd36 for which it accounts for 10.2% of the sample mass), and 2) this study focuses on transport of ash coarser than 0.125 mm, and lapilli.

2.5.2 Total Grain-Size Distribution

In order to create a high-resolution Total Grain-Size Distribution (HR-TGSD) to use as an input in Tephra2 and to compare model output to field-based HR-GSDs, our volume distributions need to be converted into mass distributions. This was done for each individual HR-GSD following the density model of Bonadonna and Phillips (2003). Their model assumes a constant density for both a smaller and larger particle boundary, with a linear increase in density between these two set bounds. For our model we use 2,380 kg/m^3 for all particles < 0.063 mm and a density of 481 kg/m^3 for all particles > 2 mm. The lower bound is the density of the glass determined by helium pycnometry by Wiejaczka and Giachetti (2022), and the upper bound was calculated by averaging the mass of all measured particles > 2 mm divided by their volume determined via DIA.

As Wiejaczka and Giachetti (2022) did for their low-resolution TGSD, the HR-TGSD was calculated by applying the Voronoi tessellation method (Bonadonna and Houghton, 2005) using the twenty-five HR-GSDs. This method creates Voronoi polygons of the area of interest in which all points inside a polygon are best represented by a central sample point, or centroid. The HR-TGSD is calculated by multiplying the HR-GSD of the centroid by the mass fraction of its representative Voronoi polygon, and then summing all weighted HR-GSDs.

2.6 Wind

Wind direction and velocity profiles at 42.982275, -122.069576 (i.e., the supposed location of the Cleetwood vent; Wiejaczka and Giachetti, 2022) were retrieved using the NCEP-DOE Reanalysis 2 database (Kanamitsu et al., 2002). All data available were gathered, that is four times daily (at 00:00, 06:00, 12:00, 18:00 UTC) over the timeframe of 1979-2022, corresponding to the first to latest wind field available at the time of writing, and totaling 64,284 wind fields. Wind files were then filtered to find and use only those for which the average wind direction between altitudes of 2 km (vent elevation) and 21 km (i.e., for a 19-km-high plume as determined by Wiejaczka and Giachetti, 2022) falls within 2° of the main dispersal axis of the lower Cleetwood unit (i.e., 129°±2° from North).

2.7 Tephra2 Grid Search

We conducted a grid search in parameter space using Tephra2 to estimate the best fit plume height (H_t), alpha (α), beta (β), diffusion coefficient (DC), and fall time threshold (FTT) for the filtered wind files. To do so, the TGSD and erupted mass, as determined above and derived from the field, were kept constant and H_t, α, β, DC, and FTT were allowed to vary. The parameters α and β were each varied over the range of 0.1-10, plume height varied from 9-30 km and both the diffusion coefficient and fall time threshold were varied over the logarithmic space 10^2-10^6. For each run the RMSE of the mass load and GSDs were determined by

$$RMSE = \sqrt{\sum_{i=1}^{n} \frac{(y_i - \hat{y}_i)^2}{n}} \quad (1)$$

where y_i is the observed result; $\hat{y}_i$ is the modeled result and n is the number of locations or grain-size bins. For mass load, the RMSE is a single value and n is equal to the 25 sample locations (one mass load per location). For the RMSE GSD, n is equal to the 26 size bins ≤3 ϕ

Table 1. Thickness, deposit density, and mass load for the lower Cleetwood unit locations used in this study.

Location ID	Distance from vent (km)	Thickness (m)	Deposit Density (kg/m^3)	Mass Load (kg/m^2)
Cltwd 01	6	1.13	767.6±5.0	867.4±9.4
Cltwd 02	32	1.13	412.8±1.0	465.6±3.2
Cltwd 05	46	0.90	524.2±5.2	471.8±7.3
Cltwd 12	48	0.45	444.9±8.0	200.2±5.8
Cltwd 13	39	0.20	603.1±6.3	120.6±4.3
Cltwd 15	52	0.64	464.7±2.0	295.1±3.6
Cltwd 16	49	0.62	471.6±8.7	344.3±9.2
Cltwd 17	55	0.56	566.9±5.1	340.1±6.1
Cltwd 18	66	0.22	503.2±5.4	110.7±3.7
Cltwd 19	61	0.19	470.6±5.7	89.4±3.4
Cltwd 20	39	0.20	532.7±6.8	106.5±4.0
Cltwd 21	55	0.53	492.0±1.9	260.7±3.5
Cltwd 22	62	0.37	493.3±3.3	182.5±3.7
Cltwd 23	68	0.15	461.8±3.0	69.3±2.8
Cltwd 24	70	0.34	545.8±4.4	185.6±4.2
Cltwd 26	68	0.42	585.6±3.2	245.9±4.3
Cltwd 32	52	0.24	508.4±2.0	122±3.0
Cltwd 33	53	0.06	438.0±7.2	26.3±2.6
Cltwd 34	56	0.14	484.2±4.0	65.4±3.0
Cltwd 36	52	0.27	772.0±3.8	208.4±4.9
Cltwd 37	58	0.43	542.6±2.5	233.3±3.8
Cltwd 38	58	0.36	536.7±2.2	190.5±3.5
Cltwd 42	61	0.41	516.5±3.0	211.8±3.8
Cltwd 43	59	0.27	510.5±6.9	137.8±4.4
Cltwd 44	60	0.19	490.9±2.7	90.8±3.0

(0.125 mm) and one RMSE is calculated per sample location, that is 25 values of RMSE GSD. To obtain a single RMSE value for GSDs, the median of these 25 values is used to estimate the goodness of the fit.

3 Results

3.1 Field

The additional pit dug in 2022 (Cltwd_2) lies on the main dispersal axis of the lower Cleetwood tephra fall deposit, approximately 32.5 km from the proposed vent. At this location, the Cleetwood deposit overlies the Llao Rock tephra fall (47 cm) and is covered first by 2.5 cm of the Basal Ash and then by 340 cm of the lower and upper pumice units of the Climactic eruption (Young, 1990; Appendix Fig. 1). The two units of the Cleetwood eruption, lower and

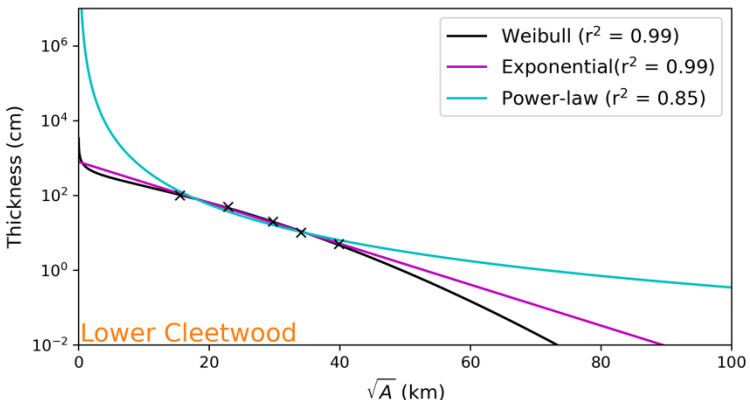

Figure 3. Semi-log plot of deposit thickness as a function of the square root of the isopach area and Weibull, exponential, and power-law best fit thinning trends for the lower Cleetwood unit.

upper, are both present at this location. The lower Cleetwood is 113 cm thick and exhibits strong normal grading. The base of this phase makes sharp contact with the top of the Llao Rock deposit, which shows signs of reworking. Median clasts are -4.2 ϕ (19.0 mm) at the base of the deposit, grading into smaller grains of -2.4 ϕ (5.4 mm) at the top. Interestingly, ~8 cm above the contact between Llao Rock and the lower Cleetwood, pumices are coated in what was identified as charcoal. This charcoal coated band is ~10 cm thick and pumices return to a white-grey color for the remainder of the lower Cleetwood deposit. The upper Cleetwood unit at this location is 3.5 cm thick and exhibits strong reverse grading. This unit reversely grades into the overlying Basal Ash unit of the Climactic eruption (Young, 1990).

3.2 Deposit Density and Mass Load

Deposit densities and mass loads for all locations used in this study can be found in Table 1. Deposit densities have an average value of 526±86 kg/m^3, a maximum value of 772±4 kg/m^3 and a minimum value of 438±7 kg/m^3, with most locations having a deposit density in the range 450-550 kg/m^3. Clwtd 1, which is the location closest to the vent, has a large deposit density of 768±5 kg/m^3 because of the presence of large, relatively heavy lithic clasts. Mass loads have an average value of 226±177 kg/m^2 with a maximum value of 867±9 kg/m^2 and a minimum value of 26±3 kg/m^2. As expected, mass load generally decreases with increasing distance from the vent.

Table 2. Plume heights and windspeeds from the R2019 and CS86 models for the lower Cleetwood unit.

Size (cm)	Rossi 1 (km)	Rossi 2 (km)	Rossi 3 (km)	CS86 (km)	windspeed (m/s)
5	16.5	18.6	20.5	23.5	28
2	5.6	13.4	16.1	22.2	36
1.5	fail	11.6	9.0	24.6	46
0.8	fail	fail	fail	27.3	30

3.3 Erupted Volume and Mass

The isopach map of the lower Cleetwood was redrawn following the addition of location Cltwd_2, further constraining the 100 cm isoline. The erupted volume was then recalculated using the exponential, power-law, and Weibull models of *TephraFits* (Biass et al., 2019) (Fig 1A; Fig 3), giving (non-DRE) erupted tephra volumes of 0.83 km^3, 0.75 km^3, and 0.86 km^3, respectively (Appendix Table 1). Both the exponential and Weibull models give the best fits to the data ($r^2 = 0.99$) and the average and standard deviation of the two (0.85±0.02 km^3) were used to convert, along with the average deposit density of all 25 locations (526±86 kg/m^3, see above), the erupted volume into an erupted mass. This translates into a total erupted mass of $4.5x10^{11}$±$0.8x10^{11}$ kg. These results confirm that the lower Cleetwood unit was a VEI 4 eruption, close to a VEI 5.

3.4 Plume Height

New maximum lithic data from Cltwd_2 made it possible to add a 1.5 cm isopleth isoline, also further constraining the 2 cm isoline (Fig. 2B). Recalculating the plume height (H_t) of the lower Cleetwood unit (Table 2) using the *CS86* model gives a H_t of 24.4±2.2 km, with a windspeed of 35±8 m/s (as a comparison, 23.5±2.3 km and 24 m/s wind speed were obtained by Wiejaczka and Giachetti, 2022 for the same phase). As shown in Figure 3 of the supplementary material of Wiejaczka and Giachetti (2022) and in Section 1.6. of this study, such strong winds are common above Crater Lake, especially between 5 and 15 km a.s.l. The R2019 model fails for the isoline of 0.8 cm and gives a H_t of 14.4±4.4 km when only

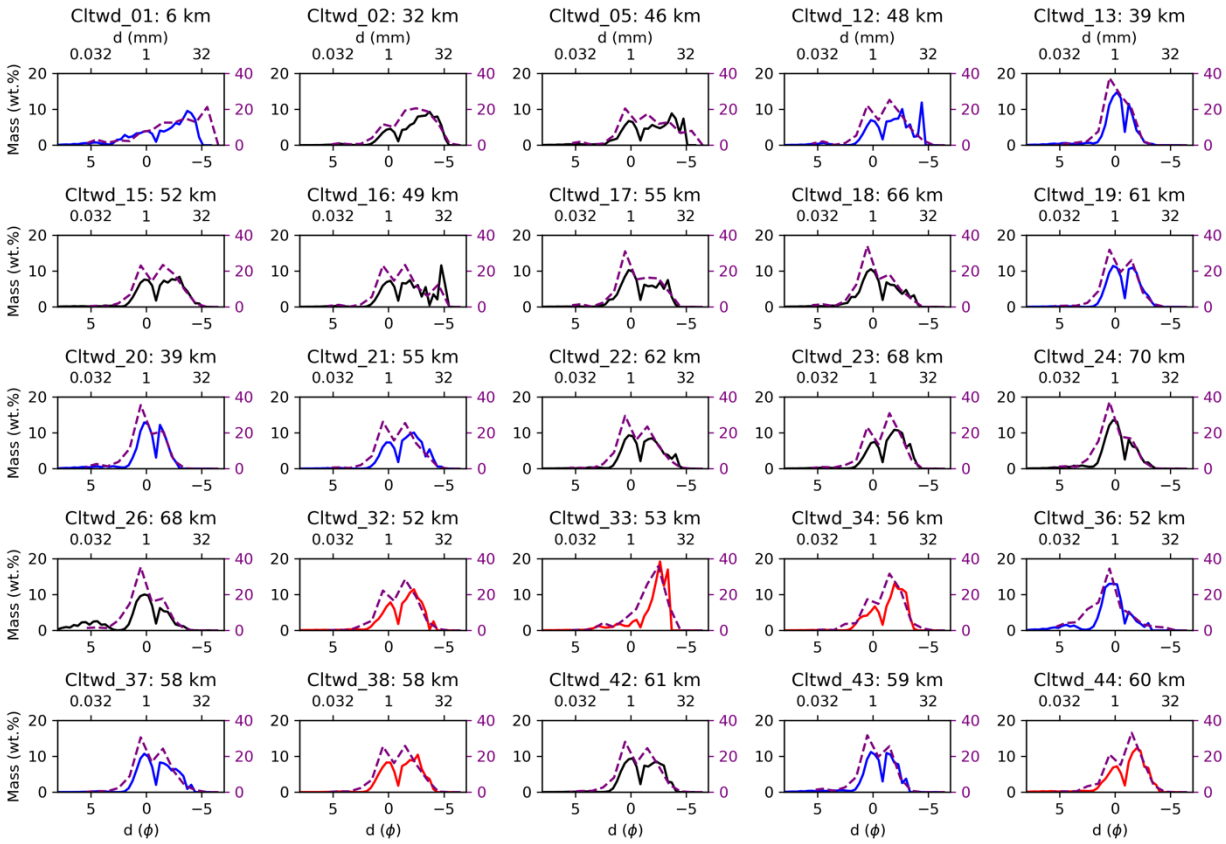

Figure 4. Individual High-Resolution Grain-Size Distributions (HR-GSDs) from the lower Cleetwood unit ranging from 6-70 km from the proposed vent location. Black, red, and blue curves represent locations along the main dispersal axis (i.e., 129°±2° from North), locations north of this line and locations south of this line, respectively. The dashed purple line is the GSD obtained from sieving. Note that the left and right y-axes have different scales.

considering eruptive scenarios 2 (intermediate intensity) and 3 (high intensity; see Rossi et al., 2019) for the 5, 2, and 1.5 cm maximum lithic isolines. This value is slightly lower than the 18.9±1.7 km obtained by Wiejaczka and Giachetti (2022) using the same model.

3.5 High-Resolution Grain-Size Distributions

3.5.1 Individual Grain-Size Distributions

Individual HD-GSDs were calculated for the 25 locations in Wiejaczka and Giachetti (2022) and this study (Fig. 4). GSDs for all locations are rather coarse with ~96% of the mass being ≤3 ϕ (0.125 mm). Each GSD exhibits at least two modes, and

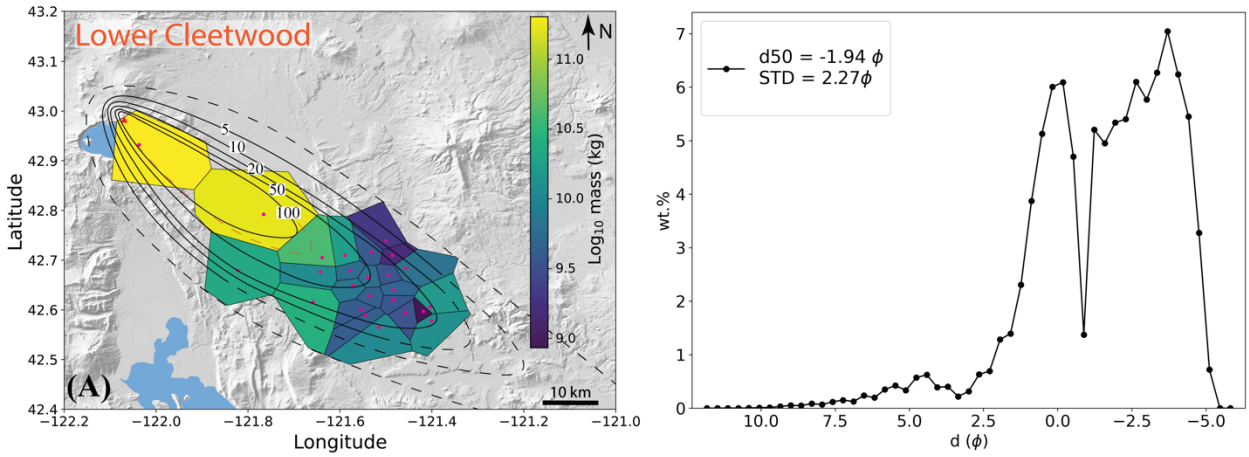

Figure 5. (A) Voronoi tessellation of the lower Cleetwood unit. **(B)** The total grain-size distribution of the lower Cleetwood unit with a median grain-size of -1.94 ϕ (3.84 mm) and a standard deviation of 2.27 ϕ (0.21 mm). Isolines are in centimeters and the dashed red line is the 100 cm isoline from Wiejaczka and Giachetti (2022). Background is global earth relief (Tozer et al., 2019).

some locations (i.e., Cltwd_26 and 36) show three modes. For 84% of the GSDs, the two major modes occur at -0.88 ϕ < d ≤ 3 ϕ (0.125 mm ≤ *d* < 1.8 mm) and ≥ -0.88 ϕ (*d* <1.8 mm), whereas the third mode, when present, is around 5 ϕ (0.032 mm). Note that this bimodality is not an artifact of converting DIA volume to mass as it is observed in the GSD obtained using (lower resolution) sieve data (Fig. 4 purple dashed lines) and for several other eruptions (e.g., Fig. 2 of Costa et al., 2016).

3.5.2 Total Grain-Size Distribution

Using the Voronoi tessellation method (Bonadonna and Houghton, 2005) on the twenty-five HR-GSDs produces a high-resolution total grain-size distribution (HR-TGSD) for the lower unit of the Cleetwood eruption (Fig. 5) with a median grain-size of -1.94 ϕ (3.84 mm), and a standard deviation of 2.27 ϕ (0.21 mm). The TGSD exhibits the three distinct modes visible in the individual HD-GSDs. The coarsest population with a median of ~-3 ϕ (8 mm), the intermediate mode with a median of ~0 ϕ (1 mm) and the finest population with a median of ~4.7 ϕ (0.04 mm). As discussed in Wiejaczka and Giachetti (2022), given the locations of the 25 samples analyzed, we believe this HR-TGSD is representative of the whole TGSD for all deposits within 70 km of the vent.

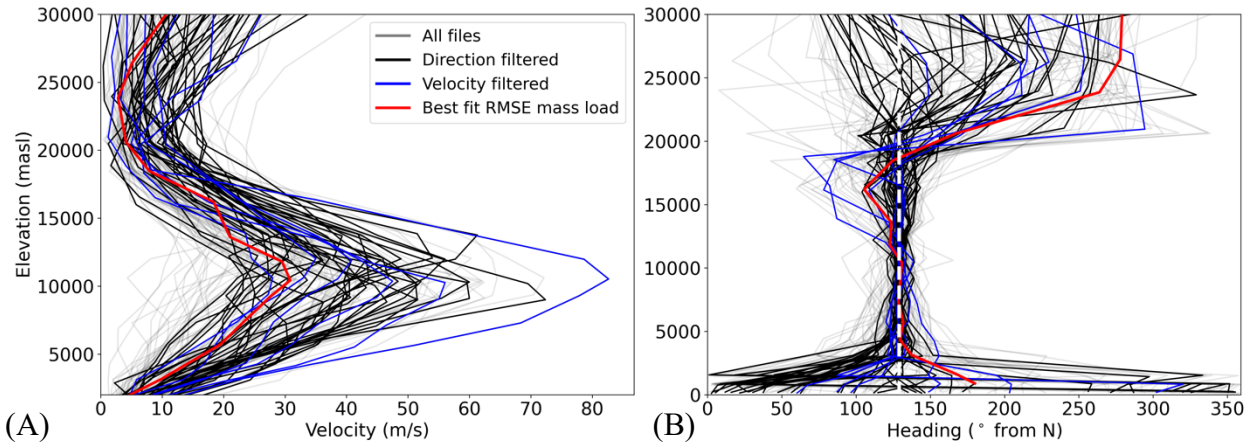

Figure 6. (A) Wind profile elevations (masl) as a function of wind velocity (m/s) profiles at 42.982275, -122.069576 (i.e., the proposed location of the Cleetwood vent; Wiejaczka and Giachetti (2022)) **(B)** Wind profile elevations as a function heading (° from North). White dashed line represents the main dispersal axis of 129° from North.

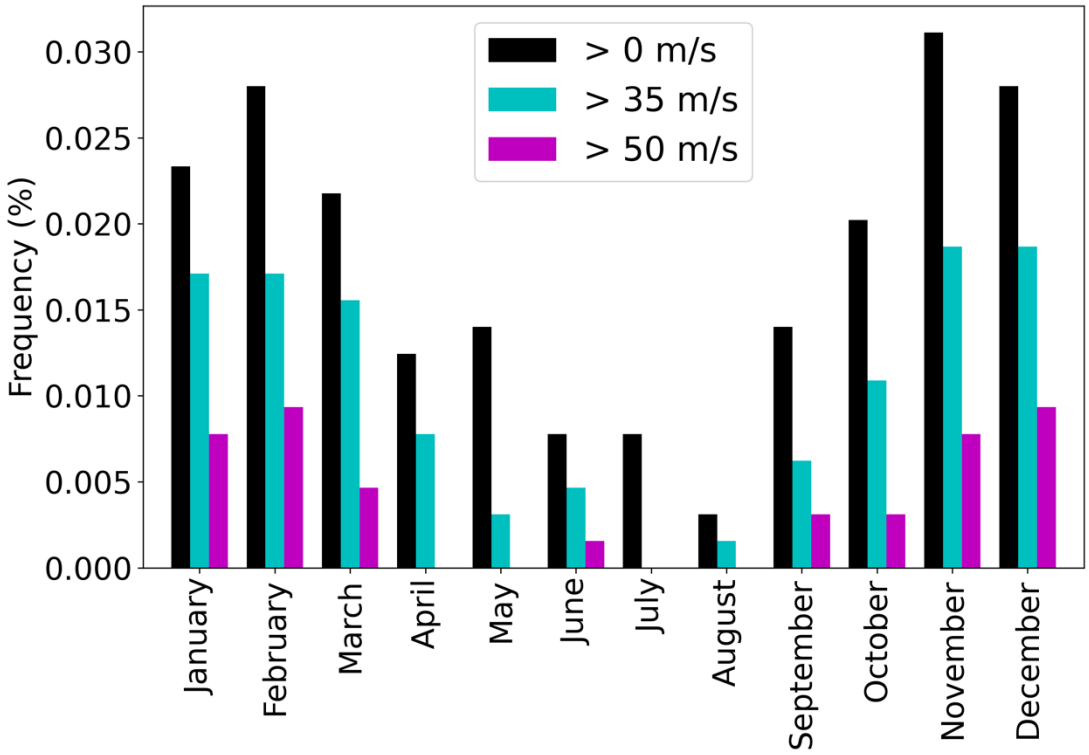

Figure 7. Frequency of wind profiles for which the average wind direction between 2 km (vent elevation) and 21 km falls within 2° of the main dispersal axis of the lower Cleetwood unit (i.e., 129°±2° from North). Wind profiles are from the NCEP-DOE Reanalysis 2 database (Kanamitsu et al., 2002) and are collected four times daily (at 00:00, 06:00, 12:00, 18:00 UTC) from 1979-2022. This corresponds to 64,284 wind fields in total at the time of writing.

Using this HR-TGSD to calculate the fractal dimension of the cumulative number distribution above 1 mm gives a value of 3.0 (r^2=0.997), consistent with the 3.1 value found by Wiejaczka and Giachetti (2022).

3.6 Wind

Filtering the 64,284 wind fields so that only those directed along the main dispersal axis of the lower Cleetwood deposit (±2°) are kept, leads to a subset of 136 wind fields, corresponding to 0.21% of our original catalog. These 136 winds can then be further filtered based solely on velocity or direction (Fig. 6). Regardless of further filtering, most wind fields have their highest velocities at elevations between 7.5 km and 15 km.a.s.l., with velocities reaching upwards of 80 m/s at a maximum. Wind velocity as a whole drastically decreases above 16-18 km a.s.l. (i.e., above the tropopause), and at higher altitudes headings move away from the main dispersal axis, usually towards the west. When distributed based on average velocities and time of the year (Fig. 7), filtered winds with an average heading of N129°±2° between 2-21 km a.s.l. concentrate in the September to May period. This trend becomes increasingly apparent when only considering wind fields that have average velocities >35 m/s (value obtained from CS86). The Cleetwood eruption thus probably occurred sometime between late summer and mid-spring.

Table 3. Output parameters from a selection of best fit RMSE ML and RMSE GSD.

	Wind	Plume Height	Alpha	Beta	Diffusion Coefficient	Fall time threshold	RMSE ML	RMSE GSD
Best RMSE ML	2020_02_27_00UTC	18500	5	2.9	1668	4642	85.68	9.78
	2014_12_22_12UTC	30000	0.8	2	16681	1000	92.38	5.79
	2007_02_17_00UTC	15000	9	5	5995	1000	98.54	7.96
	2015_09_07_06UTC	15000	7	2	774	21544	106.25	13.04
	1994_04_15_06UTC	18000	9	5	5995	1000	121.69	8.30
	2002_01_13_06UTC	21000	0.6	0.8	100	1000	129.70	12.89
	2021_02_07_18UTC	30000	0.6	1	16681	1000	153.97	9.02
Best RMSE GSD	2014_12_22_12UTC	27000	1	5	129155	4642	224.13	1.42
	2021_02_07_18UTC	24000	3	9	359381	4642	254.85	1.43
	2002_01_13_06UTC	12000	10	4	359381	100000	257.73	1.45
	1994_04_15_06UTC	12000	10	2	359381	10000	260.74	1.45
	2007_02_17_00UTC	15000	6	5	359381	100000	258.35	1.45
	2020_02_27_00UTC	12000	8	2	359381	10000	261.02	1.46
	2015_09_07_06UTC	12000	6	1	359381	10000	262.01	1.48

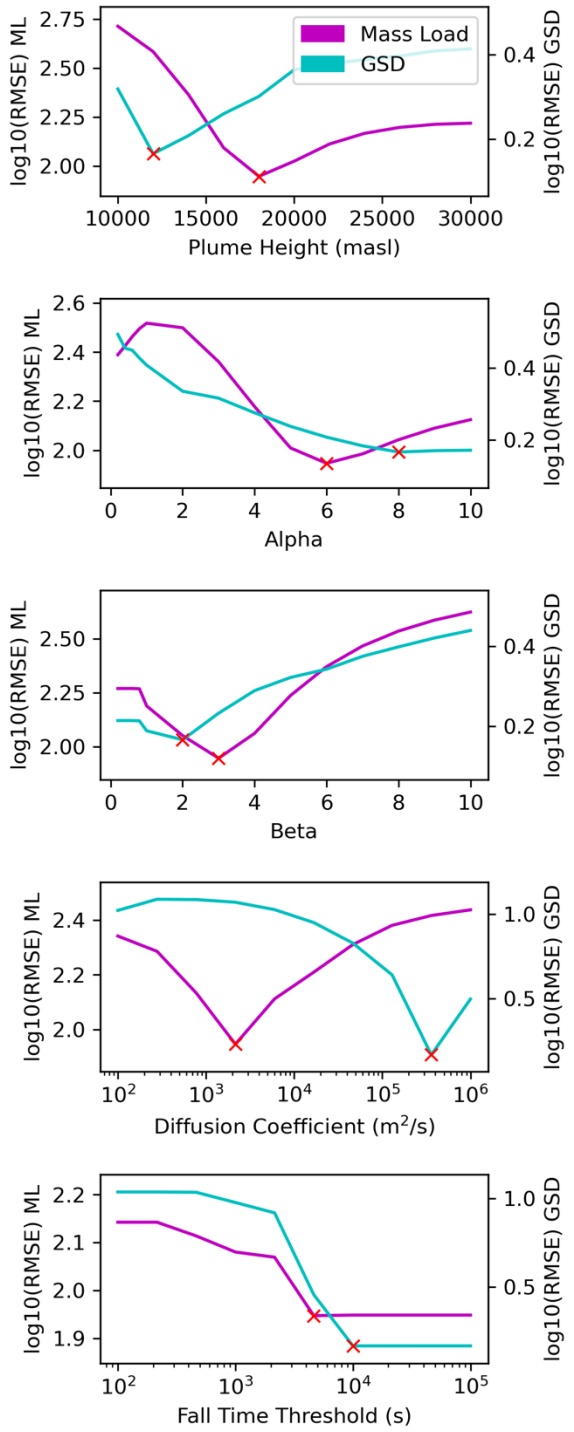

Figure 8. Sensitivity analysis on the wind field on 02/27/2020 00:00 UTC (i.e., the one which produces the best fit RMSE ML) for the parameters plume height, alpha, beta, diffusion coefficient and fall time threshold respectively.

3.7 Tephra2 Grid Search

A total of 8,839,600 scenarios were investigated using Tephra2, corresponding to 41 winds files, 11 values of H_t, 14 values of α, 14 of β, 10 values of DC and 10 of FTT. The results from a subset of the filtered wind fields are shown in Table 3 and are divided into the parameters that give the lowest RMSE for mass load (top) and the lowest RMSE for grain-size distribution (bottom). Although only a subset, they encapsulate the overall trends observed in all scenarios. Sensitivity analyses were conducted to ensure parameters reached a global minimum (Fig. 8). Full results can be found in appendix Table 2 and are discussed below.

3.7.1 Mass Load Best Fits

For all filtered wind fields, best fitting for mass load (ML) gives plume heights (H_t) of 19.0±7.5 km a.s.l., α and β values of 5.6±3.3 and 3.2±3.1, respectively, diffusion coefficients (DC) of 8,797±6,900 m^2/s, and fall time thresholds (FTT) of 5,414±8,856 s. The lowest RMSE ML of all (85.68) is obtained with the wind field from 02/27/2020 at 00:00 UTC and H_t = 18.5 km, α= 5.0, β= 2.9, DC = 1,668 m^2/s, and FTT = 4,642 s, which are all values consistent with the range provided in the

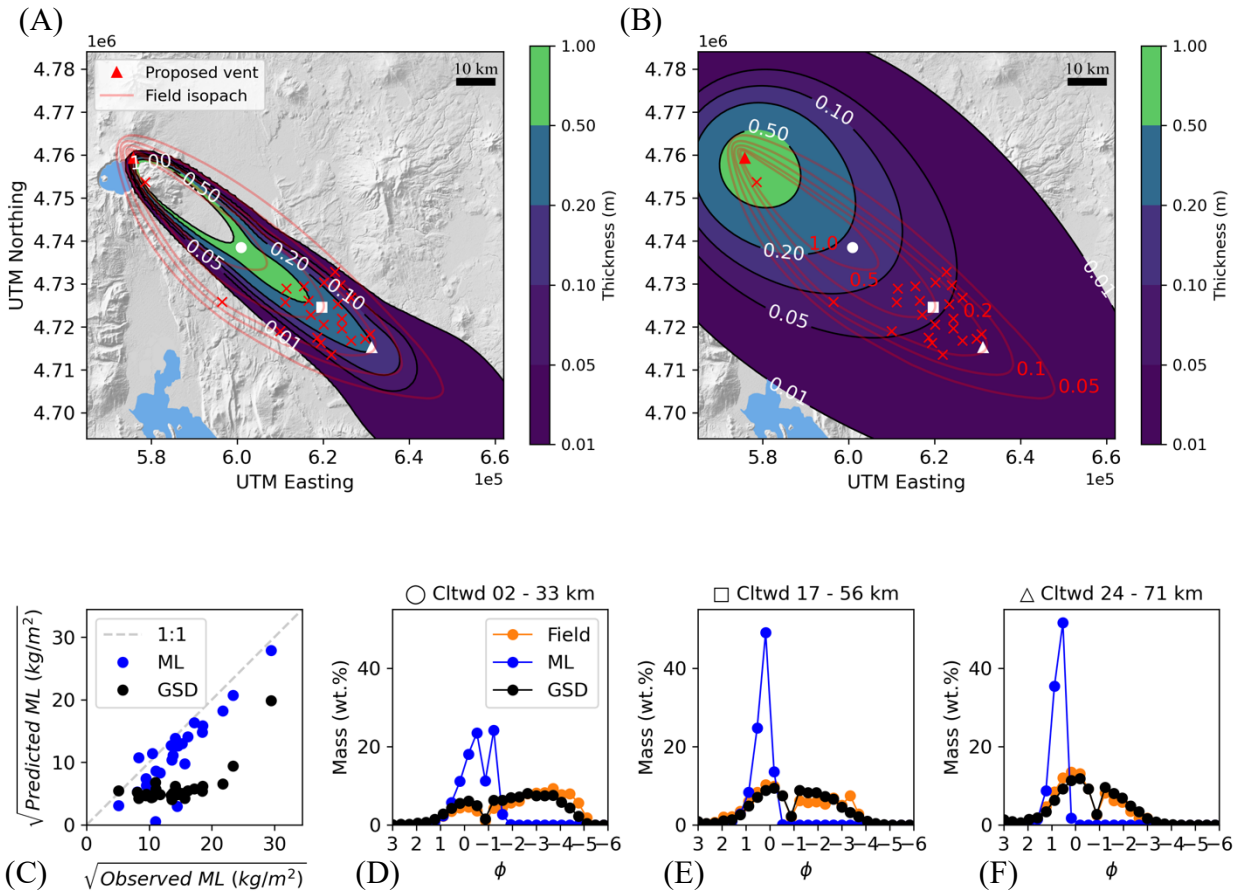

Figure 9. (A) Isopach map comparing field results with model output of best RMSE mass load (ML) for wind field 02/27/2020 00:00 UTC. Isolines in meters. Field isolines from largest to small are 1, 0.5, 0.2, 0.1, and 0.05 m respectively (see red labels on B) **(B)** Isopach map comparing field results with model output of best RMSE grain-size distribution (GSD) for wind field 02/27/2020 00:00 UTC. Background is global earth relief (Tozer et al., 2019). **(C)** Predicted vs. observed square root of best fit RMSE ML and GSD **(D-F)** HR-GSDs from the best fit ML and GSD RMSE compared with field-derived HR-GSDs. Circle, square and triangle symbols in plot titles correspond to the same symbols on above isopach maps.

literature (Bonadonna et al., 2005; Connor et al., 2006; Bonadonna et al., 2010; Elissondo et al., 2016) and H_t is consistent with the value obtained by applying the CS86 and RS19 models (14.4±4.4 to 24.4±2.2 km a.s.l.). Figure 8c shows that modeled mass loads are very closed to the measured one both close to the vent (highest mass loads) and further from it. Modeled isolines are slightly narrower than the field-derived one. The parameters that give the lowest RMSE in terms of mass load, lead to a RMSE GSD of 9.78,

compared to 1.42 when parameters are optimized to minimize the RMSE GSD. The same observation is made for all scenarios listed in the upper part of Table 3. Parameters optimized to get a low RMSE ML thus always give a poor fit in terms of GSD.

3.7.2 Grain-Size Distributions Best Fits

Best fits for grain-size distributions are obtained with average plume heights (H_t) of 14.8±4.1 km a.s.l., α and β of 5.1±2.9 and 3.3±2.7, respectively, very high DC of 34,5245±64,591m^2/s, and large fall time thresholds (FTT) of 37,243±41,834 s. When the RMSE GSD is minimized, all wind fields give similar RMSE results (1.58±0.85). The wind field that gives the lowest RMSE GSD is that on 12/22/2014 at 12:00 UTC and lowest RMSE GSD is obtained for H_t=27km, α= 1.0, β= 5.0, DC = 129,155 m^2/s, and FTT = 4,642 s. For this scenario, the RMSE ML is 224.13 (~2.5 more than when we optimize parameters to minimize RMSE ML), and when optimizing the GSD, the RMSE ML values are always very high. Isopach maps derived from the best fit RMSE GSD values (Fig. 9) are always much wider and more circular (i.e., propagating upwind and in all directions around the vent) than what is observed in the field. Note that the wind field used in Figure 9a and b is the same and is the one providing the best fit to the mass load data (02/27/2020 at 00:00 UTC).

4 Discussion

This study uses a grid search approach with the Tephra2 VATDM to determine the ESPs that best fit the mass loads and grain-size distributions observed in the field from the lower unit of the ~7.7 ka Cleetwood eruption of Mt. Mazama. While the model does well to reproduce MLs *or* GSDs with reasonable ESPs, it fails to give good fits for both MLs *and* GSDs simultaneously (Fig. 8; Table 3). When minimizing the RMSE ML, particles <-1.6 ϕ (>3.0 mm) from the coarsest mode are absent in model output GSDs (Fig. 8). This holds true for our closest sample location on the dispersal axis (33 km: Cltwd_02), where particles <-1.6 ϕ make up 68.5 wt.% of the deposit (Fig. 8D). When minimizing the RMSE GSD, 98% of the best fits give diffusion coefficients two orders of magnitude larger than those obtained when best fitting MLs. While

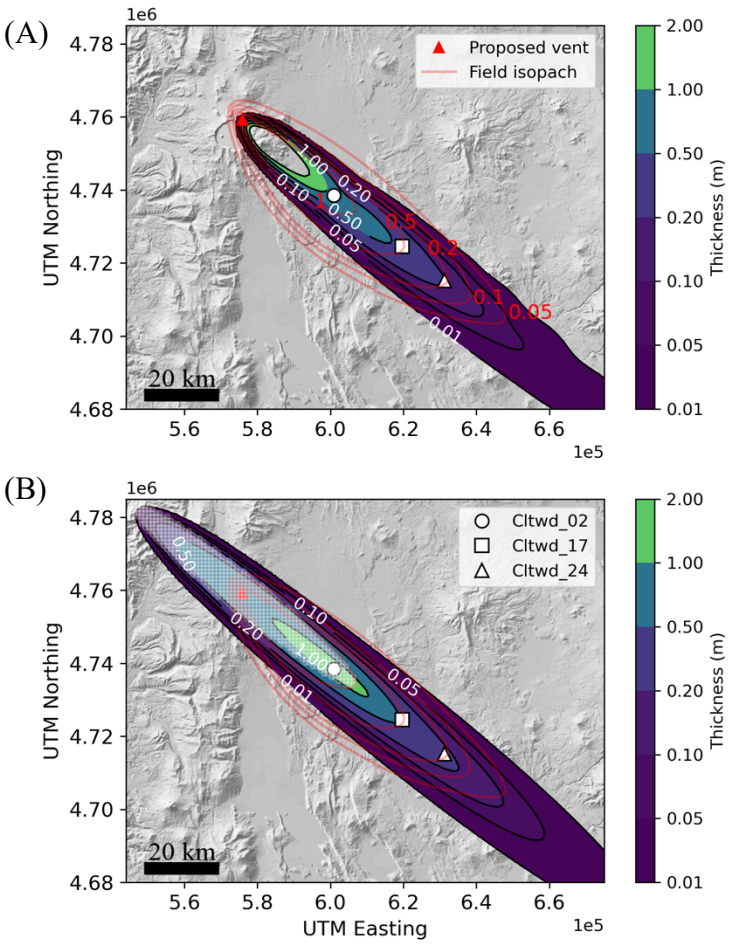

Figure 10. (A) Isopach map when using a line source with Ht = 17.5 km, α = 5, β = 2.5, DC = 1668, FTT = 7742 and the wind field from 02/27/2020 00:00 UTC. **(B)** Isopach map when using a 40x5 km^2 umbrella cloud with the same parameters. White ellipse represents the umbrella cloud geometry used. All isopachs are in meters and background is global earth relief (Tozer et al., 2019).

these are empirical values, DCs from analogous eruptions are on the same order of magnitude as those obtained when fitting MLs (e.g., 3900 m^2/s for the 2011 eruption of Cordón Caulle; Elissondo et al., 2016). Past studies have shown that if the lateral spreading of tephra (i.e., from an umbrella cloud) is not accounted for in advection-diffusion models, then both plume height and the diffusion coefficient may be overestimated (Volentik et al., 2010; Magill et al., 2015). Constantinescu et al. (2021) illustrated that modeling tephra sedimentation using Tephra2 using a disk geometry, instead of a vertical line, gave more reasonable estimations of the ESPs for the 2450 BP eruption of Pululagua (Ecuador) without artificially inflating plume height or the DC. Furthermore, the lateral spreading from umbrella clouds also assists in the transport of coarser particles farther from the vent (Sparks et al., 1992; Sparks et al., 1997; Baines and Sparks, 2005). Both the very high DCs required when minimizing RMSE GSD, and modelled deposits being poor in coarse particles when minimizing RMSE ML, point towards the fact that having an umbrella cloud, rather than a single-point vertical source, would help improve the fit of the model to the data. Given the shape

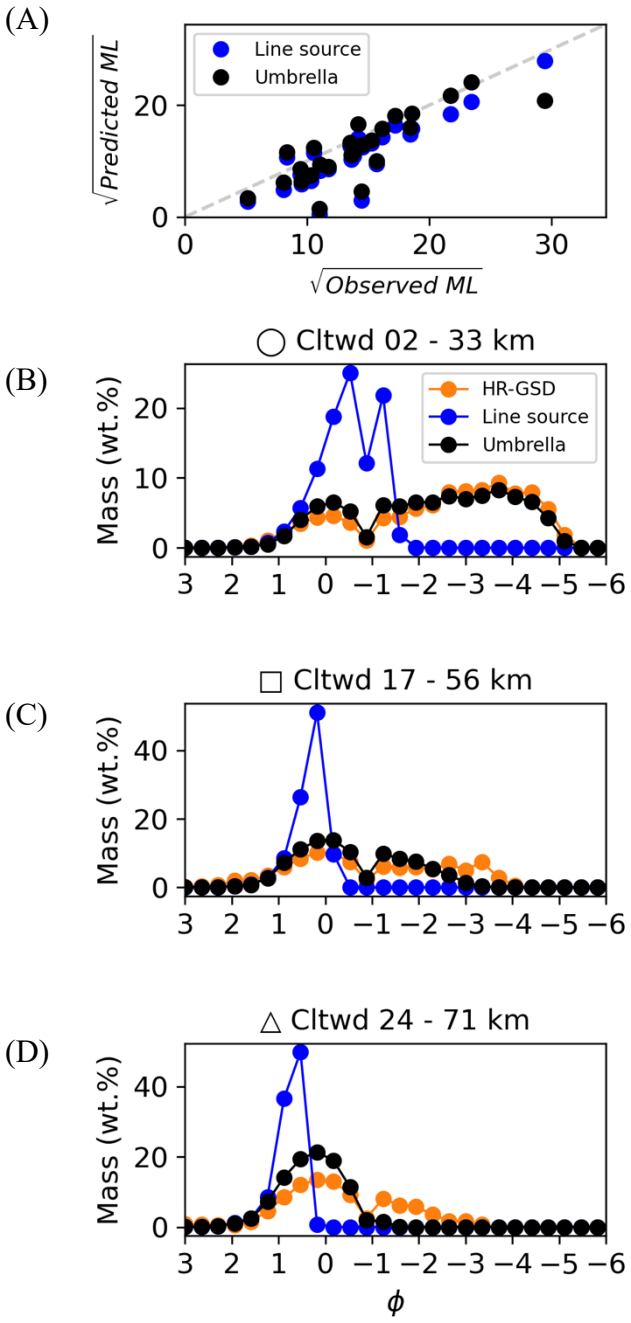

Figure 11. (A) Predicted vs. observed square root for line source and umbrella cloud scenario. **(B-D)** HR-GSDs from line source and umbrella cloud compared with field-derived HR-GSDs. Circle, square and triangle symbols in plot titles correspond to the same symbols on Fig. 10 isopach maps.

of the lower Cleetwood isopach, an umbrella cloud for this phase of the eruption is perhaps elliptical, spreading both upwind and downwind the vent and elongated in the main direction of wind propagation. Such oval umbrella shapes have been reported at Kelud (Kristiansen et al., 2015) and Calbuco (Romero et al., 2016; Van Eaton et al., 2016), for example. To test this hypothesis, we use the output of Tephra2 to calculate what would be the MLs and GSDs for such an umbrella cloud, as opposed to a single point source.

To simulate an umbrella cloud, we apply the simple and elegant approach of transforming a single Tephra2 output file. In Tephra2, the mass is initially released along a single vertical line directly above the vent. The TGSD is the same at any point vertically along this line and, as discussed earlier, the mass is distributed following a and b input parameters, the bulk of the mass being concentrated towards the upper part of the plume when $\alpha > \beta$. For a given scenario, dividing the total mass erupted by X in the input while keeping everything else constant leads to results in which the GSDs at all locations on the grid remain the same as the original results, but the mass load is divided by X compared to the original results. Thus, by

Table 4. Line source vs. umbrella cloud comparison.

	RMSE Line Source	RMSE Umbrella	% Difference
Mass Load	84.5	99.6	17.9
All GSDs	10.0	4.2	-58.0
Cltwd_01 GSD	4.9	1.9	-61.4
Cltwd_02 GSD	8.2	1.0	-87.9
Cltwd_05 GSD	9.2	1.8	-80.2
Cltwd_12 GSD	9.0	3.2	-64.0
Cltwd_13 GSD	5.3	5.1	-2.4
Cltwd_15 GSD	9.5	2.0	-79.4
Cltwd_16 GSD	10.0	3.0	-69.8
Cltwd_17 GSD	9.7	2.5	-74.1
Cltwd_18 GSD	10.5	4.2	-60.2
Cltwd_19 GSD	9.0	4.8	-46.8
Cltwd_20 GSD	9.6	4.9	-48.5
Cltwd_21 GSD	10.0	3.5	-64.7
Cltwd_22 GSD	10.2	4.4	-57.3
Cltwd_23 GSD	12.9	6.9	-46.8
Cltwd_24 GSD	10.6	3.6	-65.8
Cltwd_26 GSD	11.7	4.2	-64.0
Cltwd_32 GSD	10.8	4.6	-57.2
Cltwd_33 GSD	13.6	9.7	-28.8
Cltwd_34 GSD	12.7	7.2	-43.1
Cltwd_36 GSD	5.1	2.7	-47.5
Cltwd_37 GSD	9.1	3.1	-66.1
Cltwd_38 GSD	11.4	4.5	-60.3
Cltwd_42 GSD	10.3	4.2	-59.4
Cltwd_43 GSD	8.9	4.6	-48.8
Cltwd_44 GSD	12.8	6.7	-47.8

dividing the total mass of the original scenario by X and distributing X vertical lines in a disc or oval shape centered (or not) around the vent, one can mimic an umbrella cloud (provided $\alpha > \beta$ and the mass of the plume is concentrated in its upper section), obtaining X different output files. For such "umbrella scenario", the total mass load at a given location is equal to the sum of the X mass loads obtained from the X different output files. The GSD at that same location is the weighted average of the GSDS of the X different output files, where the weight is the relative contribution, in terms of mass load, of each of the X output files

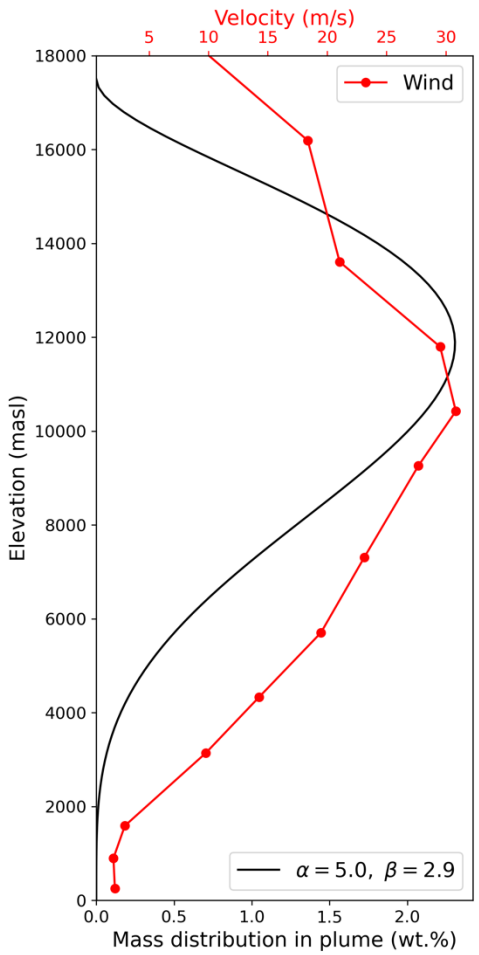

Figure 12. Beta distribution and wind profile for the best fit umbrella cloud. ~90% of the mass is released above the highest wind velocities (i.e., > 7 km) showing that both the umbrella cloud's geometry and wind contribute to the modeled deposit.

at that location. Compared to the model of Constantinescu et al., (2021), our approach has the advantage of allowing 1) the use of a custom, non-Gaussian TGSD, 2) to define elliptically- shaped umbrella cloud geometries, 3) to spread the mass vertically in the plume, and 4) the ability to vary the wind direction and speed with elevation.

We applied the above approach to the wind field that produces the best RMSE ML value while grid searching over umbrella cloud geometries and location compared to the vent. We allowed both of the semi-short and semi-long axes of the umbrella ellipse to vary between 1 and 50 km every km, keeping the long axis parallel to the main dispersal axis of the tephra deposit (i.e., N129). We also allowed the oval umbrella to be decentered from the vent, keeping the vent located on the long axis of the oval umbrella. Figure 11 shows that using an umbrella (instead of a single line source) greatly improves the GSDs, leading to a reduction in RMSE GSD of up to 87.9% at individual locations, and a 58% decrease overall (Table 4), while also maintaining a very good fit to the ML. The dimensions of the oval umbrella cloud that gives the best results are 4x40 km^2 (20 km upwind), centered on the vent, and with a plume height of 17.5 km. The alpha and beta values for the best fit umbrella scenario are 5 and 2.5, respectively, corresponding to most of the mass of the plume being concentrated between 10 and 15 km km a.s.l. (Fig. 12). Comparing this best fit geometry with well observed umbrella clouds show that this geometry is realistic. For example, the VEI 4 eruption of Kelud (Indonesia) on February 13th, 2014, produced a 200x300 km^2 oval shaped

umbrella with a radius extending ~40 km upwind and the top of the umbrella region reaching altitudes of 18-19 km a.s.l. (Kristiansen et al., 2015; Goode et al., 2019; Hargie et al., 2019).

5 Conclusions

The accuracy of Volcanic Ash Transport and Dispersal Models (VATDMs) is crucial for real-time forecasting and future hazard assessments of tephra fallout and relies on field studies of analogous eruptions to estimate the initial input Eruption Source Parameters (ESPs). The ~7.7 ka Cleetwood eruption of Mount Mazama (Crater Lake/giiwas, Oregon, United States) is a silicic eruption that has transitioned from explosive to effusive activity, with no apparent break. We re-evaluated the ESPs (plume height, erupted mass and TGSD) of the first, main phase of this eruption, the lower Cleetwood unit, which had a VEI of 4. The lower Cleetwood unit produced ~4.5×10^{11} kg of tephra with a median grain-size of 1.94 ϕ (3.84 mm) and a standard deviation of 2.27 ϕ (0.21 mm). More than 75% of the twenty-five grain size distributions measured on the tephra deposit are bimodal, and deposit at all locations is rather coarse, with ~96 wt.% of the mass being distributed ≤ 3 ϕ (> 0.125 mm). Detailed wind analysis shows that the Cleetwood eruption probably occurred sometime between late summer and mid-spring.

We carried out a grid search approach using the VATDM Tephra2 using the field-derived erupted mass and TGSD to minimize the fits of both modeled mass load and high-resolution grain-size distributions to the field data. The original model, which assumes that mass is released vertically along a single line above the vent, reproduces measured mass loads using reasonable ESPs, but fails to give good fits for mass load and HR-GSDs simultaneously. Optimizing the fit for best mass loads results in the coarsest particles falling too close to the vent. On the other hand, minimizing the fit of the model to the field-derived grain size distributions, leads to unrealistically high diffusion coefficients. To be able to fit both mass loads and grains-size distributions simultaneously, we post-treat Tephra2 output to simulate an umbrella cloud. Unlike other similar approaches, our method allows for the use of a custom TGSD, variable umbrella cloud geometries, vertical mass distribution in the plume, and the use of real 1D wind fields. Grid searching over umbrella cloud geometries and plume heights gives the best results for an elliptical geometry of 4x40 km^2 (20 km upwind). The addition of this umbrella cloud greatly improves the fits to measured grain size distributions, while maintaining a very good fit to the measured mass loads.

Our findings contribute to improving the understanding and prediction of the transport and sedimentation of tephra from silicic volcanic eruptions that transition from explosive to effusive activity. This study demonstrates the value of using high-resolution grain size distributions at individual locations to give insight into both the wind conditions and the plume geometry and dimensions for unwitnessed eruptions. Our addition of a custom geometry and a mass distributed umbrella cloud further emphasizes the importance of considering accurate eruption source parameters to successfully model historic eruptions, especially when the intent of using these results is to mitigate the impacts of future volcanic eruptions.

CHAPTER IV

PHYSICAL CHARACTERISTICS OF THE PRODUCTS FROM THE HYBRID EXPLOSIVE-EFFUSIVE ACTIVITY OF THE 2011-2012 ERUPTION OF CORDÓN CAULLE

From Wiejaczka J and Giachetti T (in prep.). Physical Characteristics of the Products from the Hybrid Explosive-Effusive Activity of the 2011-2012 Eruption of Cordón Caulle

1 Introduction

Silicic eruptions have been classically divided into two discrete end members, explosive and effusive eruptions. Explosive activity produces particle-laden plumes that can reach tens of kilometers in altitude and deadly pyroclastic density currents, both of which can widely disperse tephra. Effusive eruptions tend to be more quiescent, producing thick domes and lava flows confined to the areas immediately surrounding the source vent.

Most deposits from historic highly silicic eruptions include both explosive and effusive products and are believed to be emplaced in tandem over one eruptive cycle. These include the ~7.7 ka Cleetwood eruption at Mount Mazama (Young, 1990; Wiejaczka and Giachetti, 2022), the 1060 CE Glass Mountain eruption of Medicine Lake volcano (Heiken, 1978), and the 640 CE Big Obsidian Flow eruption at Newberry Volcano (Kuehn, 2002; Trafton and Giachetti, 2022), amongst others. The shift from explosive to effusive activity has been described as occurring due to a transition from closed to open-system degassing (Eichelberger and Westrich 1981; Eichelberger et al. 1986; Newman et al. 1988; Adams et al. 2006; Castro and Gardner 2008; Degruyter et al. 2012). Closed-system degassing facilitates magma fragmentation via high magma ascent rates (i.e., explosive activity), while open-system degassing allows for gas escape through permeable networks due to a decrease in magma ascent (i.e., effusive activity).

Prior to the 2008 eruption of Chaitén (Chile) and the 2011-2012 eruption of Cordón Caulle (Chile), no rhyodacitic/rhyolitic eruption had been observed in modern history. At Chaitén, after the initial explosive phase, an explosive eruption occurred through fractures while a dome was growing (Pallister et al., 2013; Castro et al., 2014). At Cordón Caulle, direct observations showed development of a small plume transporting tephra to the surface through fractures that infiltrated the simultaneously erupting obsidian flow (Schipper et al.,

2013; Fig. 12 from Wadsworth et al., 2022). These direct observations at both Volcán Chaitén and Cordón Caulle illuminated that eruptive styles, at least in the silicic realm, can in fact be non-discrete and that explosive and effusive behaviors can occur simultaneously in a so-called hybrid phase.

The sedimentological characteristics of several historic silicic eruptions are like those found at Chaitén and Cordón Caulle, suggesting that the explosive to effusive transition might be a common trait to most highly silicic eruption. For example, through detailed componentry analysis, Trafton and Giachetti (2022) observed a drastic increase in obsidian pyroclasts in the uppermost stratigraphy of the 640 CE Big Obsidian Flow eruption deposit (Newberry Volcano; USA). They attributed this to a conduit being repeatedly sealed via sintering and agglomeration of magmatic ash fragments, which is repeatedly shattered by Vulcanian-like explosive events. They surmised that the explosive phase of the 640 CE Big Obsidian Flow eruption likely transitioned from an initially stable sub-Plinian phase to pulses of Vulcanian-like activity, before ultimately transitioning to effusive activity. However, their observations and conclusions pertain to the end of the main explosive phase. Due to poor deposit preservation following centuries of erosion, tephra layers that would have been deposited during a hybrid explosive/effusive phase at these historic eruptions are most probably unrecoverable. This makes Chaitén and Cordón Caulle the currently unique rhyodacitic/rhyolitic tephra deposits where a complete record of the transition from explosive to effusive activity exists and can be studied in detail.

In this study we analyze tephra samples collected from the explosive portion of the hybrid phase from the 2011–2012 rhyolitic eruption of Cordón Caulle (Chile). This suite of samples gives an unprecedented chance to examine their size and componentry with the aim at determining temporal trends towards the end of the eruption. Changes in both the size and abundance of different types of particles with time may bridge the gap and give potential insight into how similar historic eruptions shifted from explosive to hybrid to final effusive activity.

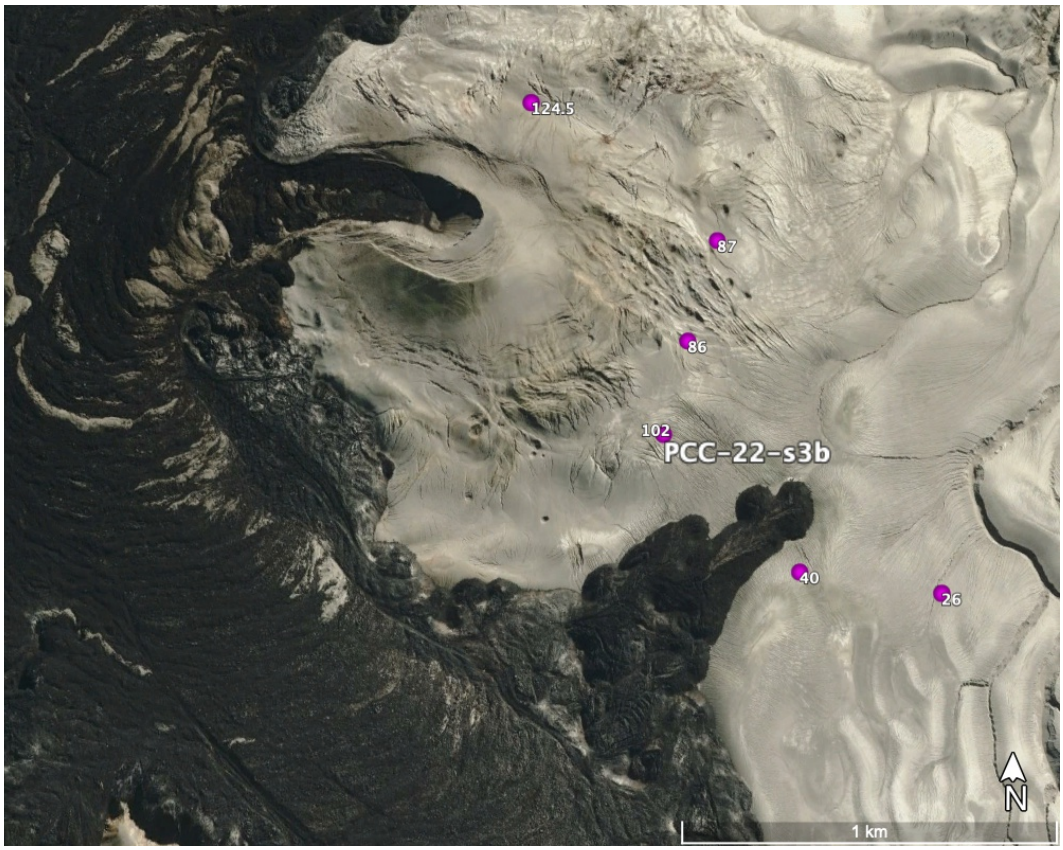

Figure 1. March 2022 field campaign sites (image data ©2023 CNES/Airbus). Numbers represent the thickness of the hybrid phase in centimeters.

1.1 The 2011-2012 Eruption of Cordón Caulle

Presented below is the chronology of the 2011-2012 eruption of Cordón Caulle and the associated physical characteristics of the tephra deposit for each major event, as described by Pistolesi et al., 2015. The eruption of Cordón Caulle, in Chile, began on June 4th, 2011 at 18:45 UTC. It produced a large, stable plume that reached altitudes of up to 15 km (Collini et al., 2012). Between June 5th and June 7th fluctuations in plume height (12-8 km) and thus mass discharge, were observed. While the mass discharge rate fluctuated, it never reached values below 10^6 kg/s (Bonadonna et al., 2015a) until after June 15th. For a brief period on June 6th, the plume dispersal rapidly shifted from the E to a NNE heading. Mid-June marks the beginning of a months-long intermittent sub-Plinian activity with the simultaneous continuous effusion of rhyodacitic lava (Silva Parejas et al., 2012), referred to as hybrid by

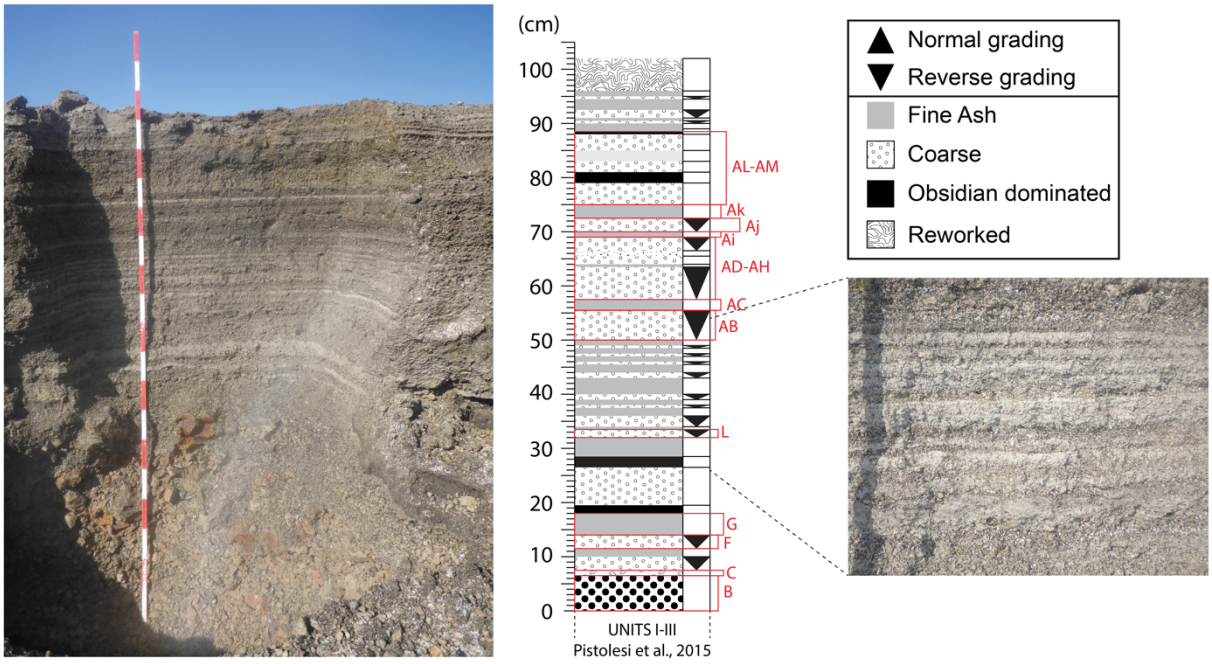

Figure 2. Stratigraphy at PCC-22-s3b. Red letters represent the layers sampled for this study.

Schipper et al. (2013). By January 2012, this hybrid activity continued, but the average plume height had decreased to ~1.5–5 km. After transitioning to solely effusive activity, lava emergence from the vent ended on 15 March 2012 according to SERNAGEOMIN.

Pistolesi et al. (2015) divided the tephra fall deposit into four main units (I, II, III, and IV). Unit I represents the opening phase of the eruption and is characterized by multiple coarse, reversely graded layers. At sections 15 km from the vent, median grain-sizes reach upwards of 8.6 mm. Unit II contains layer G, which represents the time on June 6th when the dispersal direction rapidly shifts to the NNE. Overall grain-size decreases in this unit with the median grain-size at the same 15 km location diminished to 1.8 mm. Unit III is distinguished in proximal locations by five layers alternating between coarse and fine grain-sizes with median grain-sizes ranging from 1.5 to 3.1 mm. Unit IV is only present in proximal locations as a mm thick ash deposit, suggesting it was deposited during lowered intensity.

2 Methods

2.1 Field

Field work was conducted in March of 2022 and focused on the deposit of the hybrid phase of the 2011-2012 eruption of Cordón Caulle tephra fall deposit, 0.4 km to 1.7 km east southeast of the vent (Fig. 1). Six pits were dug by hand until the base of the hybrid phase was reached. The deposit was divided into subunits based on changes in grading, particle size, and componentry at each location. Subunits were described in full, their thickness measured, photographed, and several hundred grams to kilograms of each subunit were collected and transported back to the physical volcanology laboratory at the University of Oregon for analysis. This study focuses on samples collected from the following subunits at PCC-22-s3b (Fig. 1; Fig 2): B, C, F, G, L, AB, AC, AD-AH, Ai, Aj, Ak, and AL-AM.

2.2 Laboratory Analyses

All samples collected at PCC-22-s3b were analyzed for low resolution grain-size distribution by sieving and massing and were further analyzed for high-resolution grain-size distribution by combining laser diffraction and dynamic image analysis. Componentry analysis of particles ≥ 0.125 mm was carried out on subunits B, AB, AC, Ak, and AL-AM. Componentry distributions and high-resolution grain-size distributions (HR-GSDs) were constructed following the methodology detailed in the methods section of Chapter III. The reader is referred to this section for a full description of the sample preparation and methods used. A brief summary is given below.

2.2.1 Grain-Size Analyses

Samples from each subunit were first dried in a convection oven at 100 ˚C for 24 hr to remove adsorbed water. Bulk samples were then split into workable aliquots and each aliquot was then manually sieved into twelve size fractions: 0-0.032 mm, 0.032-0.063 mm, 0.063–0.125 mm, 0.125–0.25 mm, 0.25–0.5 mm, 0.5–1 mm, 1–2 mm, 2–4 mm, 4–8 mm, 8–16 mm, 16-32 mm and 32-64 mm. Each sieve size fraction was then weighed using a high-precision balance before high-resolution particle size analysis.

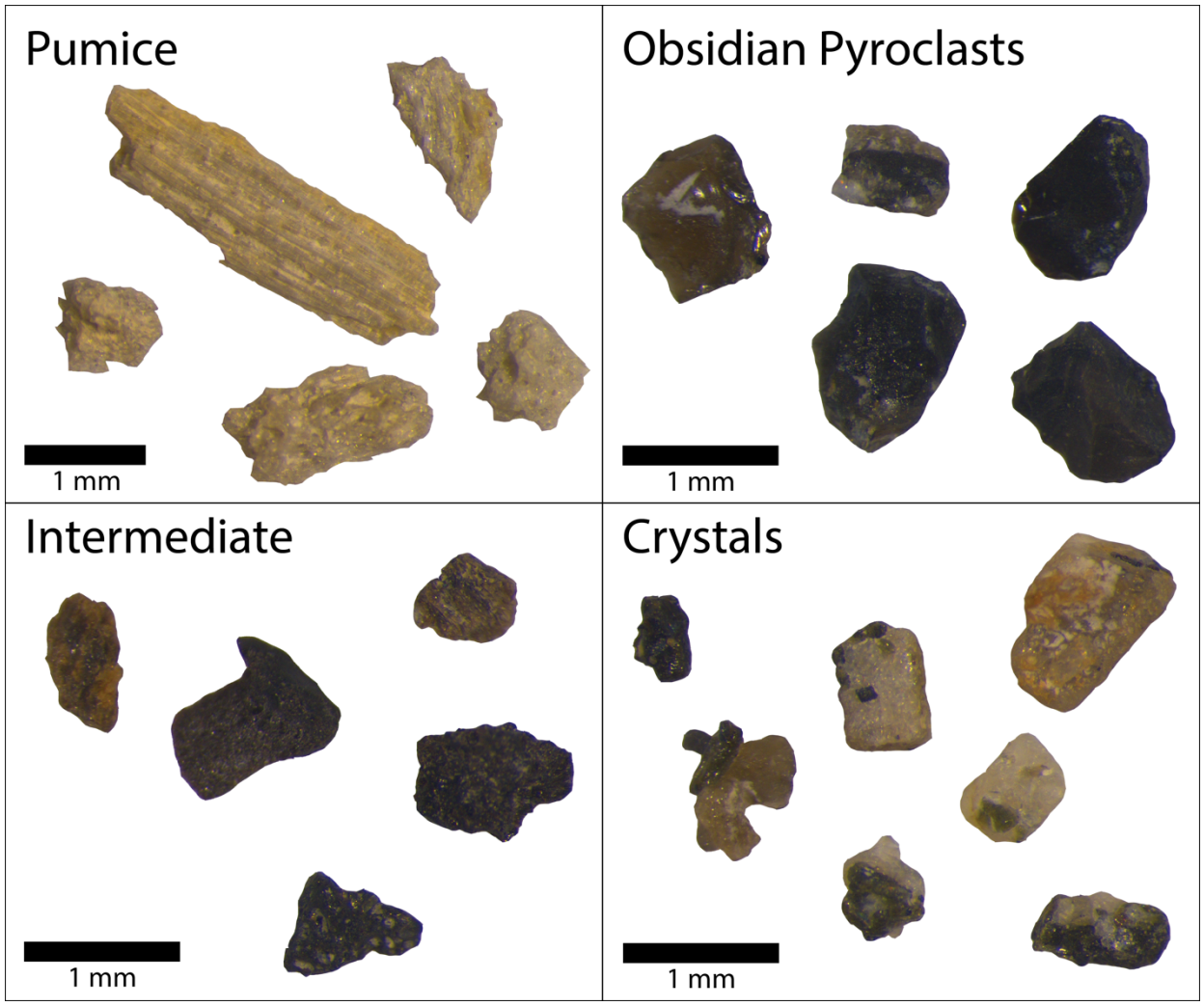

Figure 3. Stereomicroscope images of the pumice, obsidian pyroclasts, intermediate, and crystal component categories.

The size of each particle from each size fraction ≥0.125 mm was measured via Dynamic Image Analysis (DIA) using a Microtrac PARTAN 3D particle size analyzer at the University of Oregon. Size measurements for aliquots of particles 0–0.125 mm were done using laser diffraction on a Beckman Coulter LS 13 320 at the USGS Cascades Volcano Observatory. In this study, results are sorted in 50 regular logarithmic bins from 0.00035 to 35 mm, and both the distributions of volume and particle number density as a function of size are presented. Data collected by laser diffraction was first converted from volume percent to an absolute volume using the density of the glass (2,690 kg/m^3) measured by Pistolesi et al., 2015 and the mass of the sieved fraction. To determine number densities, the number of particles for each bin was calculated by assuming spherical particles. This is a built-in assumption used during laser

diffraction analysis. The number of particles is thus determined by dividing the total volume of each bin by the volume of a single particle with a diameter equal to the center of that bin. For size fractions larger than 0.125 mm, individual particles were analyzed via DIA and the number of particles per bin is obtained directly. The number density of particles (m^{-3}) was then calculated by dividing the total number of particles per bin by the total volume of the sample analyzed. To produce a single distribution, we use laser diffraction data for sieve fractions <0.125 mm and DIA data for all size fractions >0.125 mm.

2.2.2 Componentry

For size fractions ≥ 0.25 mm, all particles were handpicked and sorted into one of the following components using a stereomicroscope: pumice, Intermediate (banded pumice, pieces of the flow), obsidian pyroclasts and loose crystals (Fig. 3). Pumice lapilli are generally golden in color and exhibit elongated to spherical shapes. Obsidian pyroclasts range from completely translucent to black dense particles. Intermediate components include pumice with obsidian

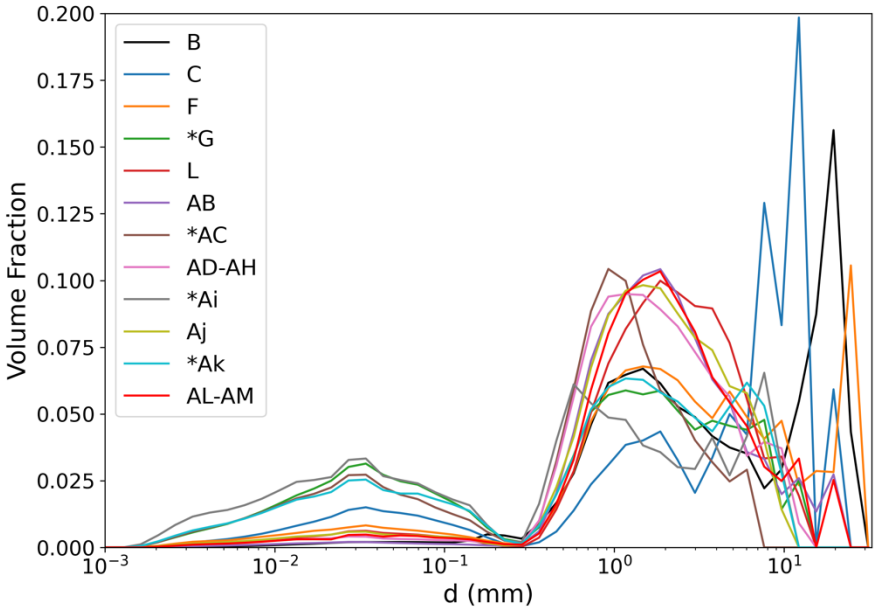

Figure 4. Volume fraction as a function of equivalent diameter, d (mm). Asterisk (*) next to the layer's name denotes a fine ash layer.

Table 1: Sample locations, thicknesses, and distances from the vent.

Location ID	Latitude	Longitude	Thickness (m)	Distance from vent (km)
PCC-22-s3b	-40.527406	-72.140201	1.02	0.9
PCC-22-s4	-40.531317	-72.131204	0.26	1.7
PCC-22-s5	-40.530835	-72.135734	0.4	1.4
PCC-22-s8	-40.525035	-72.139369	0.86	0.8
PCC-22-s9	-40.522423	-72.138300	0.87	0.8

banding and vesiculated pieces of the flow. Once separated, all particles of each component at each size fraction ≥ 0.25 mm were analyzed via DIA to measure their relative volume in each size fraction. For size fractions 0.125-0.25 mm, images of the bulk sample were taken, and individual components were outlined using Adobe Photoshop. The area of each particle was then determined with the Fiji (ImageJ) image processing package (Schindelin et al., 2012), and component volumes were calculated assuming a spherical shape. Particles that were cut by the image boundary were not included.

3 Results

3.1 Field

Six pits were dug and investigated in the proximal section of the deposit, within 2 km from the vent (Table 1). Their thickness ranges from 26-124.5 cm (Fig. 1). While only the

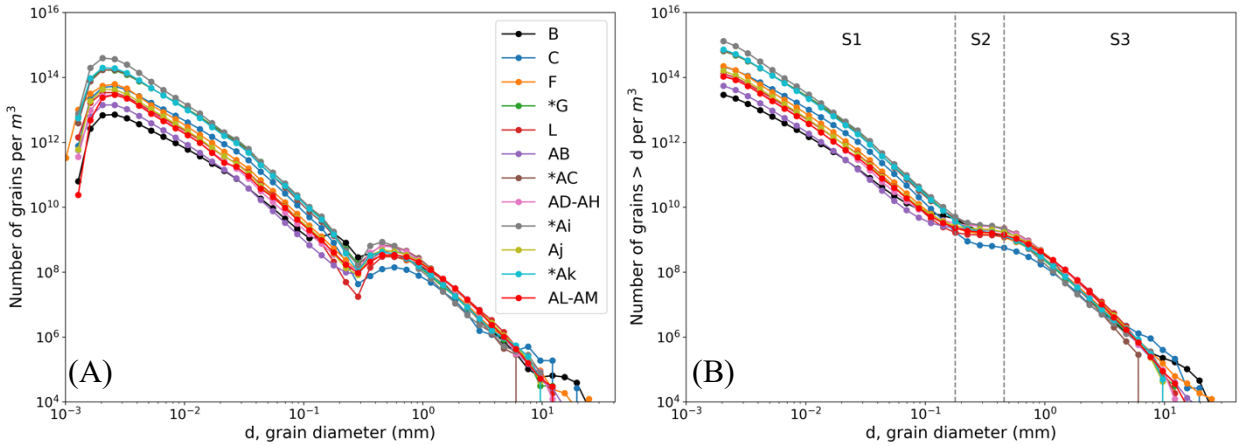

Figure 5. (A) Number density, N, versus equivalent diameter, d, for layers of PCC-22-s3b **(B)** Cumulative number density, N, versus equivalent diameter, d, for the layers of PCC-22-s3b. Breaks in slope at 0.178 mm and 0.456 mm create three individual segments S1, S2, and S3, which are observed in all distributions. A segments' s fractal dimension (D1, D2, and D3) is obtained by fitting a power law, $N{>}d = \lambda d^{-D}$, where N is the number density of particles greater than size d, D is the fractal dimension, and λ is a scaling factor. Asterisk (*) next to the layer's name denotes a fine ash layer.

Table 2: Fractal dimension values of cumulative grain-size distributions, D, for layers of PCC-22-s3b, together with the r^2 value of the fit. D1, D2, and D3 respectively correspond to the best fits of segments S1 (<0.178 mm), S2 (0.178-0.456 mm), and S3 (>0.456 mm) of the cumulative size distribution (see Figure 5).

Layer	D1	D1 r^2	D2	D2 r^2	D3	D3 r^2
B	2.17	0.993	1.08	0.981	3.18	0.995
C	2.65	0.983	0.62	0.925	2.63	0.993
F	2.70	0.994	0.53	0.978	3.04	0.996
*G	2.74	0.988	0.77	0.979	3.13	0.998
L	2.65	0.992	0.20	0.853	3.04	0.986
AB	2.50	0.993	0.30	0.919	3.31	0.989
*AC	2.77	0.990	0.48	0.976	3.77	0.996
AD-AH	2.57	0.994	0.38	0.909	3.35	0.994
*Ai	2.85	0.995	0.65	0.928	3.18	0.997
Aj	2.62	0.995	0.37	0.891	3.20	0.992
*Ak	2.78	0.992	0.63	0.961	3.07	0.998
AL-AM	2.56	0.996	0.39	0.974	3.22	0.988

stratigraphy of sample location PCC-22-s3b (Fig.2) is described in detail below, it captures the general trends observed at all locations. The deposit makes sharp contact with the top of what we interpreted to be the unit III described by Pistolesi et al. (2015). This contact is marked by a drastic shift in grain-size with maximum pumice measurements decreasing from 30 cm at the top of Unit III to about 1.5 cm at the base of Unit IV. The total thickness at this location is 102 cm and was further divided into 40 distinct layers. The most obvious feature in the whole Unit IV deposit is the repeating occurrence of couplets of 1) a reversely graded lapilli-dominated layers capped by 2) a layer of fine ash, which are present throughout the entirety of the deposit. Occasionally this couplet pattern is interrupted by thin layers (~1-2 cm) which are more obsidian rich than the rest of the deposit (Figure 2). These layers only occur in the first and last third of the stratigraphy. The upper 7 cm of the deposit is visibly eroded and highly reworked.

3.2 Grain-Size Distributions

All grain-size distributions plotted in terms of volume fraction as a function of equivalent diameter, d (mm), show at least a bimodality with the two modes occurring below and above ~0.3 mm (Fig. 4). For layers at the bottom of the stratigraphy (i.e., B, C, and F) a third

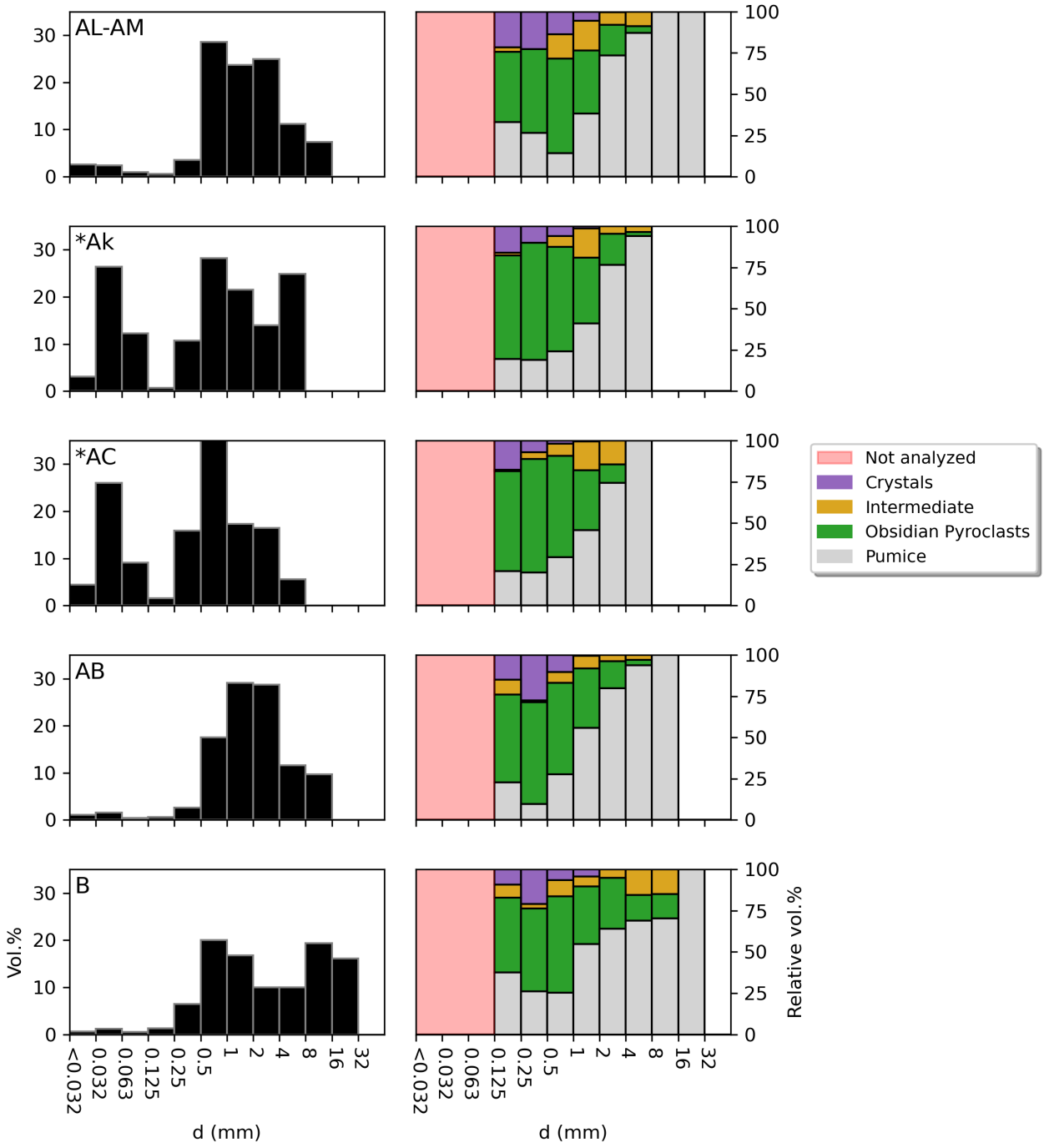

Figure 6. Volume percent of bulk samples (left) and relative volume percent of individual components within each size fraction (right), plotted as a function of equivalent diameter, *d*. Asterisk (*) before a sample's name denotes a fine ash layer.

coarser mode occurs around 5 mm. As expected, fine ash layers (i.e., G, AC, Ai, and Ak) have a more abundant mode of finer particles; for example, 39% of the total volume of the fine ash layer Ai occurs below 0.3 mm. All number density (and thus cumulative number density) distributions exhibit the same trough around 0.178-0.456 mm, regardless of the layer (Fig. 5A). In cumulative number density GSDs, this lack of particles creates two systematic breaks in slope from a power-law relationship around 0.178 mm and 0.456 mm (Figure 5B). These breaks in slope form three individual segments which can be fit by a power-law relationship, $N_{>d} = \lambda d^{-D}$, where D is the fractal dimension of the segment being considered. Following Wiejaczka and Giachetti (2022), we define D1, D2, ad D3 as the best fits of segments S1 (<0.178 mm), S2 (0.178-0.456 mm), and S3 (>0.456 mm), respectively (Table 2). D1 values range from 2.17-2.85 and are the highest for the fine ash layers. D2 values are the lowest of all fractal dimensions and range from 0.20-1.08. Values of D3, for particles >0.456 mm, range from 2.63-3.77.

3.3 Componentry

Detailed componentry was conducted at sample location PCC-22-s3b on all size fractions ≥0.125 mm in layers B, AB, AC, AK, and AL-AM (Fig. 6; Fig. 7). In all layers, pumice and obsidian pyroclasts are the major components and account for at least 42% and 29% of each layer's volume ≥0.125 mm, respectively. The median grain-size is controlled by the major components and exhibits a decrease in the first 18 cm of the stratigraphy from 2.6-0.13 mm (Fig. 7). For the remainder of the stratigraphy the median grain-size fluctuates between lapilli and fine ash layers. Intermediate (banded pumice, pieces of the flow) and loose crystals are minor components and make up only 5% and 2% of a sample's volume, respectively. Notably, both intermediate particles and loose crystals reach their maximum values of 11% and 6%, respectively, toward the top of the deposit.

4 Discussion

Detailed sedimentological studies from explosive-effusive historic eruptions at Mount Mazama (Young, 1990; Wiejaczka and Giachetti, 2022), Newberry Volcano (Trafton and

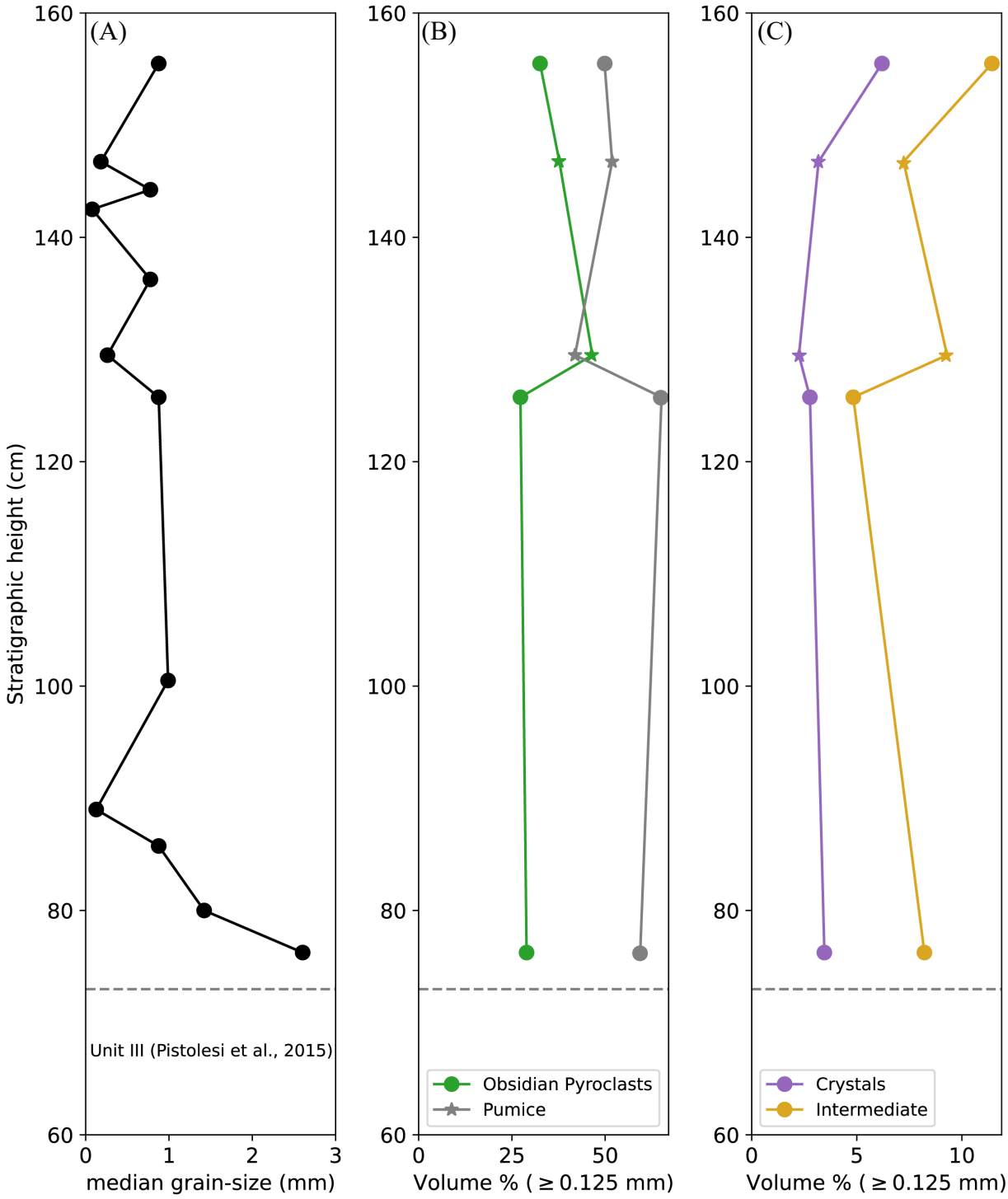

Figure 7. (A) Median grain-size (mm) as a function of stratigraphic height. **(B)** Pumice and obsidian pyroclasts (major component) vs. stratigraphic height. **(C)** Intermediate (banded pumice, pieces of the flow) and obsidian pyroclasts (minor components) as a function of stratigraphic height. Note that the x-axis of **B** and **C** are different scales and star symbol denotes a fine ash layer.

Giachetti, 2022), and Medicine Lake Volcano (Giachetti and Shea, in prep.) show that all deposits exhibit, after the first explosive unit (step 1 in Fig 8A), at least one prominent ending explosive unit that is reversely graded, with an increase in pyroclastic obsidian component. Wiejaczka and Giachetti (2022) interpreted these characteristics seen in the upper Cleetwood unit of the ~7.7 ka Cleetwood eruption of Mount Mazama unit to be a consequence of competing rates between erosion and ash sintering/agglomeration. They surmised that the lowered mass eruption rate (MER) towards the end of the lower Cleetwood unit facilitated sintering over erosion, allowing for progressive welding of ash particles to the conduit margins which partially sealed the conduit and repressurized the system. They further inferred that this re-pressurization initiated the beginning of the upper Cleetwood unit, during which the mass eruption rate increased with time and erosion rates dominated over sintering in the final Plinian phase (i.e., steps 2-3 in Fig 8A). Similarly, Trafton and Giachetti (2022) observed repeated sequences of reverse grading and increased obsidian pyroclast abundances in the upper pumice unit of the 640 CE Big Obsidian Flow eruption. They attributed this to a conduit being cyclically sealed via ash agglomeration and then shattered by Vulcanian-like explosive events, before ultimately transitioning solely to effusive activity. While these observations align to some extent with the characteristics described by Pistolesi et al. (2015) for Unit III of the 2011-2012 Cordón Caulle eruption, it is important to note that these findings at Mazama and Newberry Volcano specifically pertain to the conclusion of the primary explosive phase. Unfortunately, the tephra layers associated with the hybrid explosive-effusive phase during these historical eruptions, if any, are likely to remain inaccessible due to the significant erosion of the deposits over centuries. The samples analyzed in this study currently serve as a unique collection of the hybrid phase of an explosive-effusive eruption and give insight into this previously missing pivotal activity.

The analysis of the stratigraphy of the hybrid phase reveals a repeating couplet pattern of a reversely graded lapilli-dominated layers followed by a layer of fine ash. These couplets are like the units upper Cleetwood at Mazama and upper pumice at Newberry described above but occur at a smaller scale in terms of both thickness and median grain-size. Unlike the units from these aforementioned historic eruptions, lithics are not a significant part of the deposit at

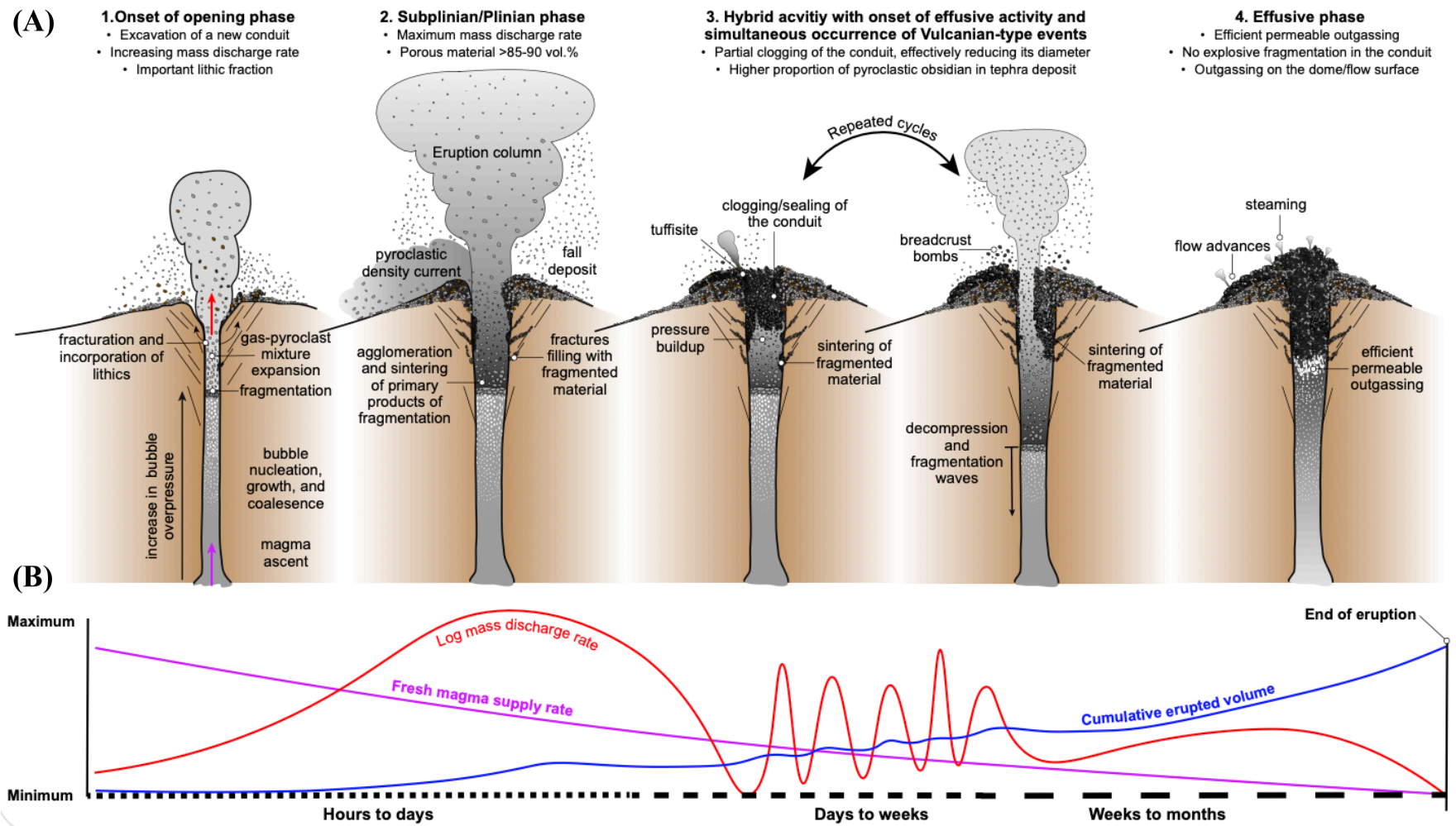

Figure 8. Figure from Giachetti et al., Pulling the Plug: Do Silicic VEI 4-5 Eruptions Always Progress from Plinian to Vulcanian, and Finally to Effusive Activity? Poster presented at: the IAVCEI Scientific Assembly, February 2, 2023; Rotorua, New Zealand. **(A)** Schematic showing the eruptive progression from the opening Plinian phase to the closing effusive phase. **(B)** Mass discharge rate, magma supply rate, and cumulative erupted volume vs. time based on analysis from historic eruptions at Mount Mazama, Newberry Volcano, Medicine Lake Volcano and recent direct observations at Chaitén and Cordón Caulle.

Cordón Caulle, and instead, pumice and obsidian pyroclasts consistently dominate. This suggests that during the hybrid phase of the eruption, tephra is transported to the surface through fractures in a substantially annealed vent structure, and little to no country rock is excavated during this phase. These deposit and component characteristics suggest that the ash in the upper portion of the plumbing system underwent sintering following shallow fragmentation, resulting in the formation of a dense plug that narrows the shallow conduit. Consequently, the system experiences a re-pressurization, leading to the fragmentation of parts of the plug during subsequent explosive events. Fluctuations in the MER over the course of this phase point to changes in the degree of conduit sealing and thus re-pressurization efficiency. Wiejaczka and Giachetti (2022) showed that D1 values (the fractal dimension of the grain size distribution for particles <0.125 mm) can be used to infer the potential energy of fragmentation. D1 values for this phase increase overall as conduit sealing becomes more prominent and changes drastically between each plug shattering sequence (Fig. 9). During these repeated cycles of plug formation and shattering, the overall MER wanes in accordance with the rate of fresh magma supply. This reduction of MER and magma supply rate eventually leads to efficient permeable outgassing

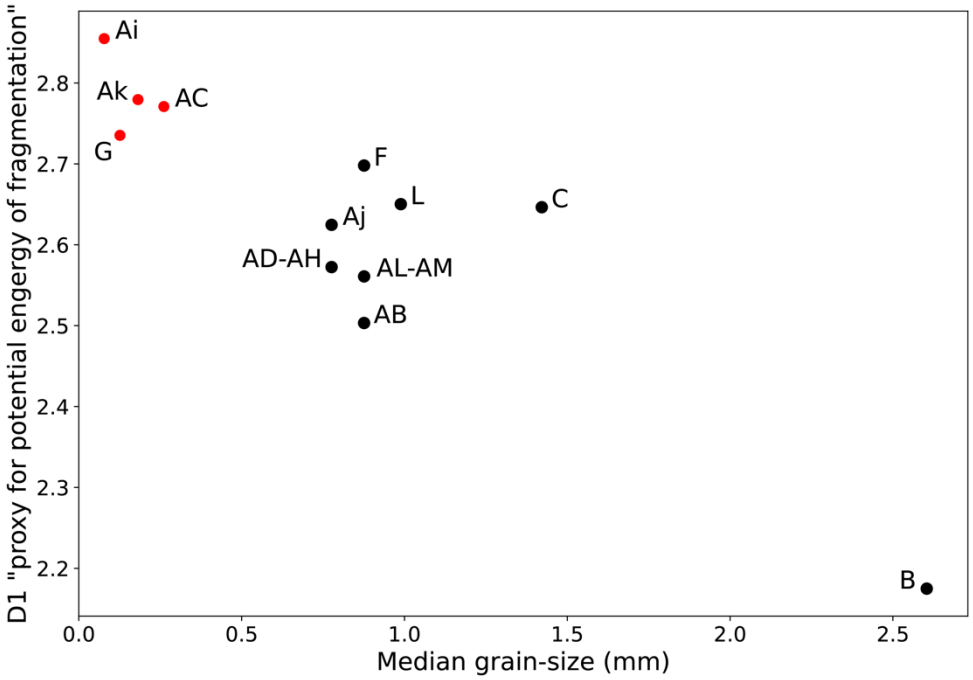

Figure 9. D1 values for all analyzed layers of PCC-22-s3b plotted as a function of the median grain-size of that layer. Red markers denote fine-ash layers.

dominating over re-pressurization that finally facilitates a purely effusive stage, as suggested by Eichelberger et al., (1986; “permeable foam collapse’; Fig. 8A 3-4; Fig. 8B). Noticeably towards the later stages of the hybrid phase, there is a rise in intermediate components including banded pumices, fragmented pieces of the flow, and loose crystals, while the overall proportion of pumice decreases. This gradual increase in these components with time could potentially serve as a signal for the eventual cessation of the explosive activity.

4.1 Future Directions

This research on the sedimentological characteristics of the tephra from the hybrid phase of the 2011-2012 eruption of Cordón Caulle is in progress. Further textural analysis of the juvenile components, especially obsidian pyroclasts, is underway to determine if changes occur within the stratigraphy, and thus with time. Componentry analysis for all layers collected at all sizes is ongoing and especially important for the fine-ash layers where particle sizes <0.125 mm make up a significant portion of a layer’s volume. Furthermore, analysis directly on the loose crystals along with a direct comparison with those found in the effusive products is needed to continue to explore how these eruptions transition from explosive to hybrid to a purely effusive activity. A comparison with the fresh rhyolitic deposits of Chaitén, which exhibit the same overall progression in type of activity, could confirm whether this behavior is common to most rhyodacitic/rhyolitic systems.

5 Conclusion

Before the 2008 eruption of Chaitén and the 2011-2012 eruption of Cordón Caulle, no explosive rhyodacitic/rhyolitic eruption transitioning to effusive behavior had been witnessed in modern history. Direct observations showed explosive activity occurring simultaneously with the effusion of lava as a never-before-seen hybrid phase. Although many historic examples of highly silicic explosive-effusive eruptions exist, extensive erosion over centuries has led to deposit degradation, rendering the tephra layers from the hybrid phase irretrievable. This study showcases a distinct suite of samples from the hybrid phase of the 2011-2012 eruption of Cordón Caulle, significantly contributing to our understanding of this previously overlooked stage. By examining the componentry and grain-size distributions of the layers composing the hybrid phase stratigraphically, a distinct recurring pattern emerges consisting couplets of 1) a reversely

graded layer dominated by lapilli capped by 2) a fine ash layer. The observed characteristics of the deposit and components indicate that the ash in the upper part of the plumbing system undergoes sintering after shallow fragmentation. This process results in the formation of a compact plug that constricts the shallow conduit, leading to a re-pressurization of the system. Subsequently, this re-pressurization leads to parts of this dense plug fragmenting during the next explosive event. The insignificant abundance of lithics suggests that, during this hybrid phase, little new vent excavation occurs and almost no country rock is being incorporated in the eruptive mixture. By examining the fractal dimension of particles smaller than 0.125 mm, we believe it is possible to estimate the potential energy of fragmentation. Fluctuations of this value during this phase appear to indicate variations in the level of conduit sealing and the efficiency of re-pressurization. Generally, the D1 values increase as conduit sealing becomes more prominent, with changes occurring between each occurrence of plug shattering. Throughout the repetitive cycles of plug formation and shattering, the overall mass eruption rate gradually decreases in line with the rate of fresh magma supply. Eventually, this decline allows for efficient permeable outgassing to dominate over re-pressurization, ultimately leading to a final purely effusive stage.

A. CHAPTER II APPENDIX

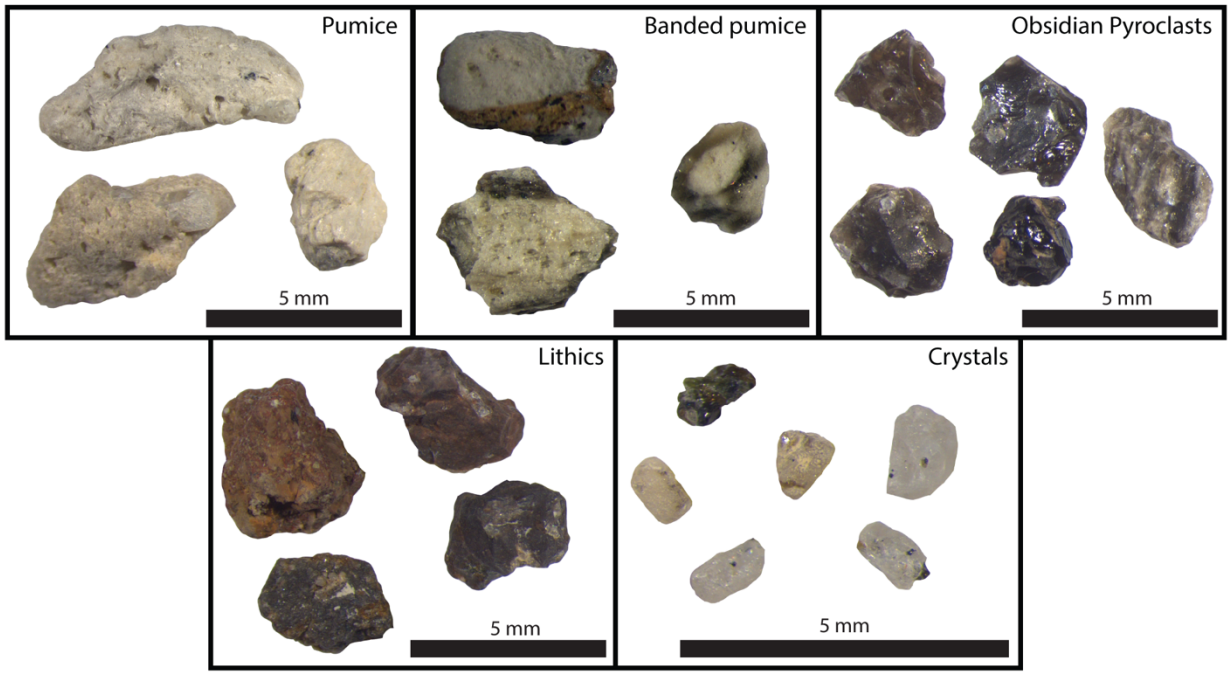

Appendix Figure 1. Stereomicroscope images of component categories.

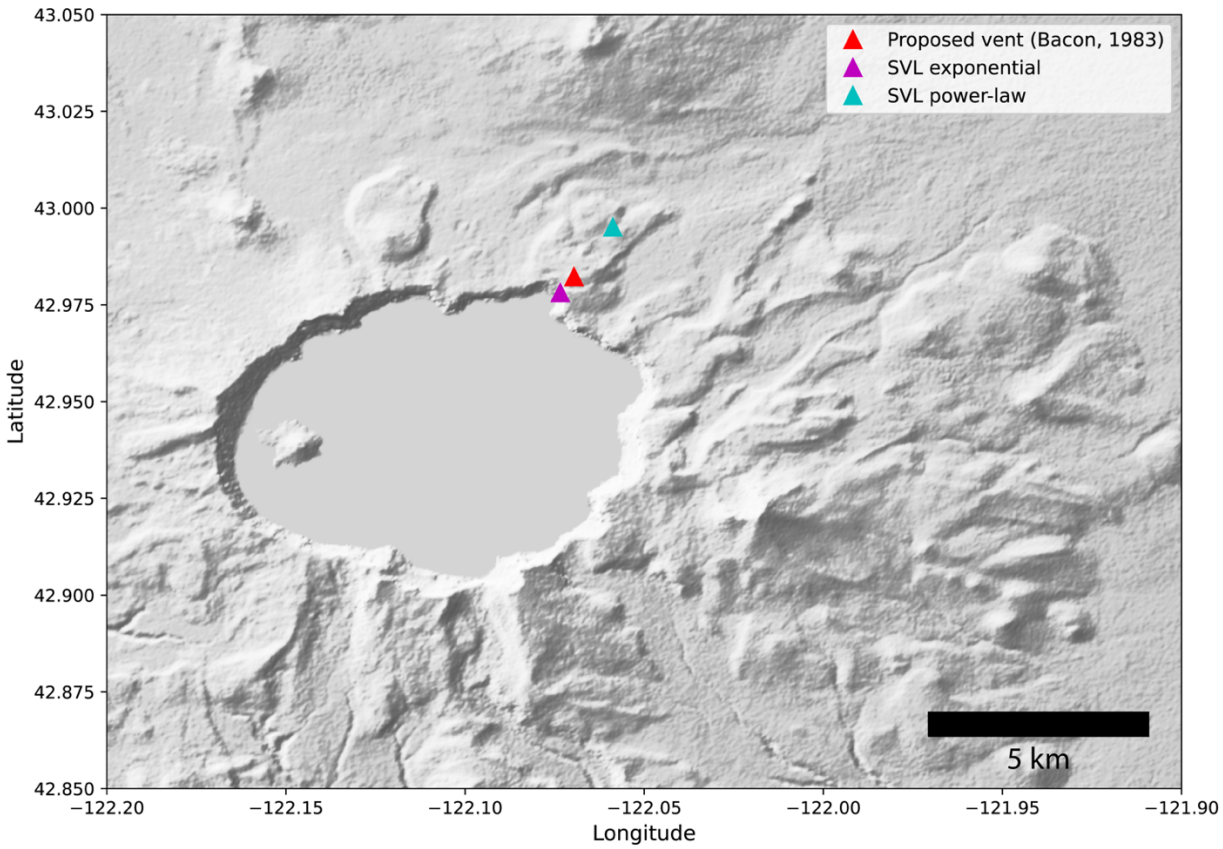

Appendix Figure 2. Proposed Cleetwood vent location from Bacon (1983) and the power-law and exponential vent locations generated by the SVL model of Yang et al. (2019).

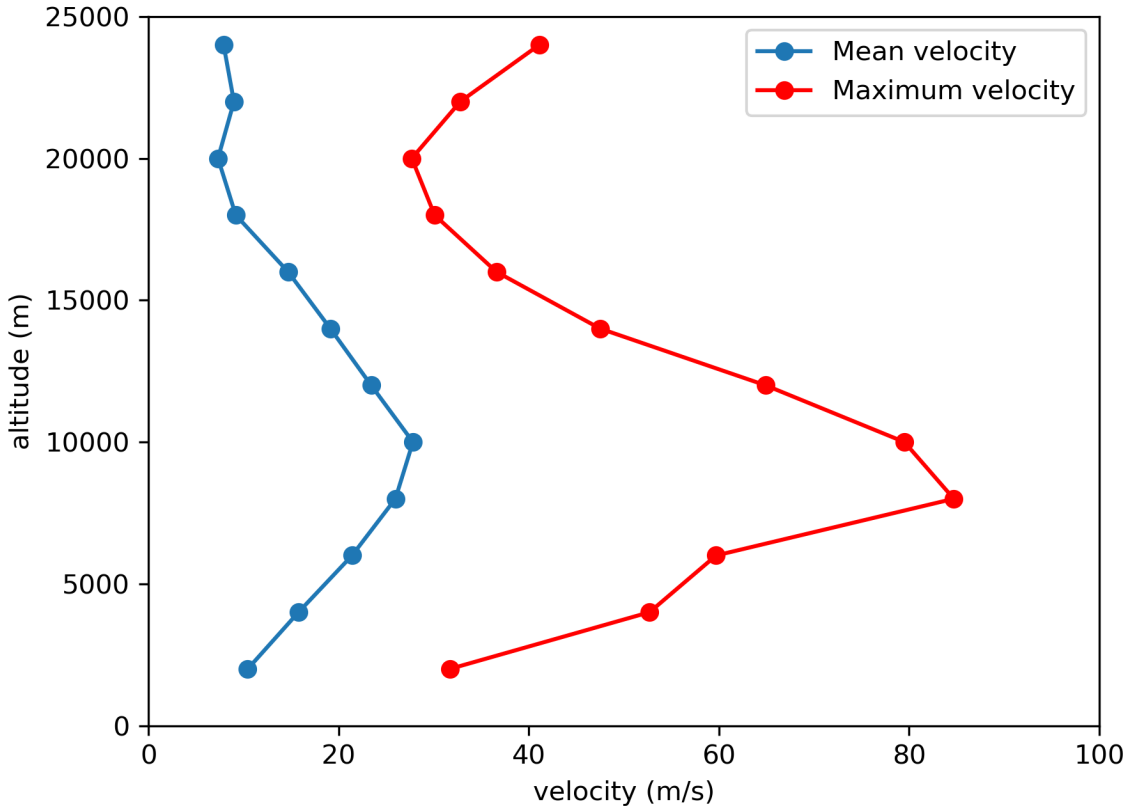

Appendix Figure 3. NCEP-DOE Reanalysis 2 (Kanamitsu et al., 2002) wind velocity data for the year 2020 at Crater Lake.

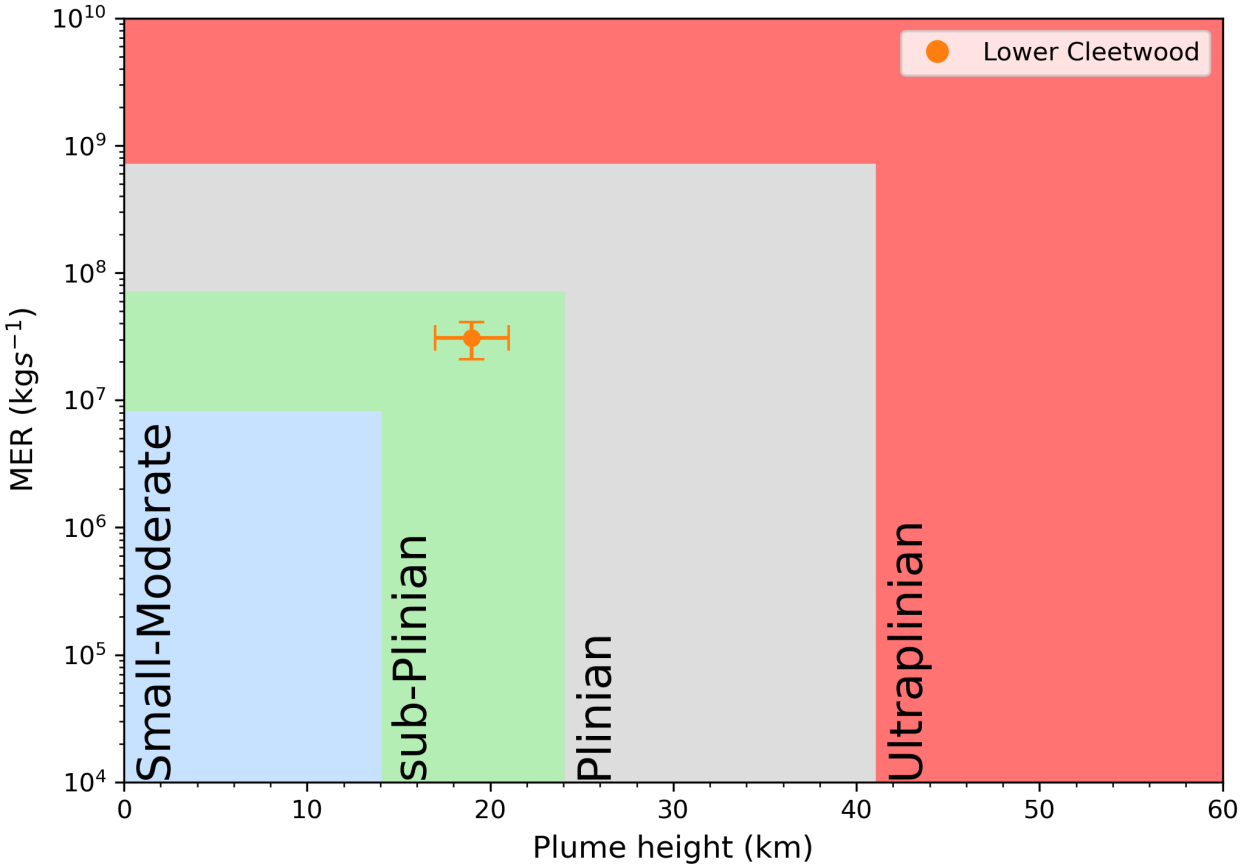

Appendix Figure 4. Plume height versus mass eruption rate (MER) classification for tephra deposits. The lower unit of the Cleetwood eruption of Mazama plots within the sub-Plinian field. Figure modified from Bonadonna and Costa (2013).

Appendix Table 1. Density model used to convert mass to volume for the cumulative number density of the TGSD.

Phi	Density (kg/m^3)
-6	455
-5	455
-4	455
-3	455
-2	455
-1	455
0	746
1	1209
2	1567
3	1975
4	2380
5	2380
6	2380
7	2380
8	2380
9	2380
10	2380

Appendix Table 2: Plume heights (km) and windspeeds (m/s) for the lower Cleetwood unit calculated using the models of Carey and Sparks (1986; *CS86*) and Rossi et al. (2019; *R2019*). Using *R2019*, only eruptive scenarios 2 (intermediate intensity) and 3 (high intensity) were considered (see Rossi et al., 2019 for details concerning these scenarios).

Maximum lithic (cm)	*R2019* Scenario 2 (km)	*R2019* Scenario 3 (km)	*CS86* (km)	*CS86* windspeed (m/s)
5	17.9	20.0	21.9	27
2	17.1	20.6	25.1	24
0.8	extrapolation fails	extrapolation fails	26.7	29

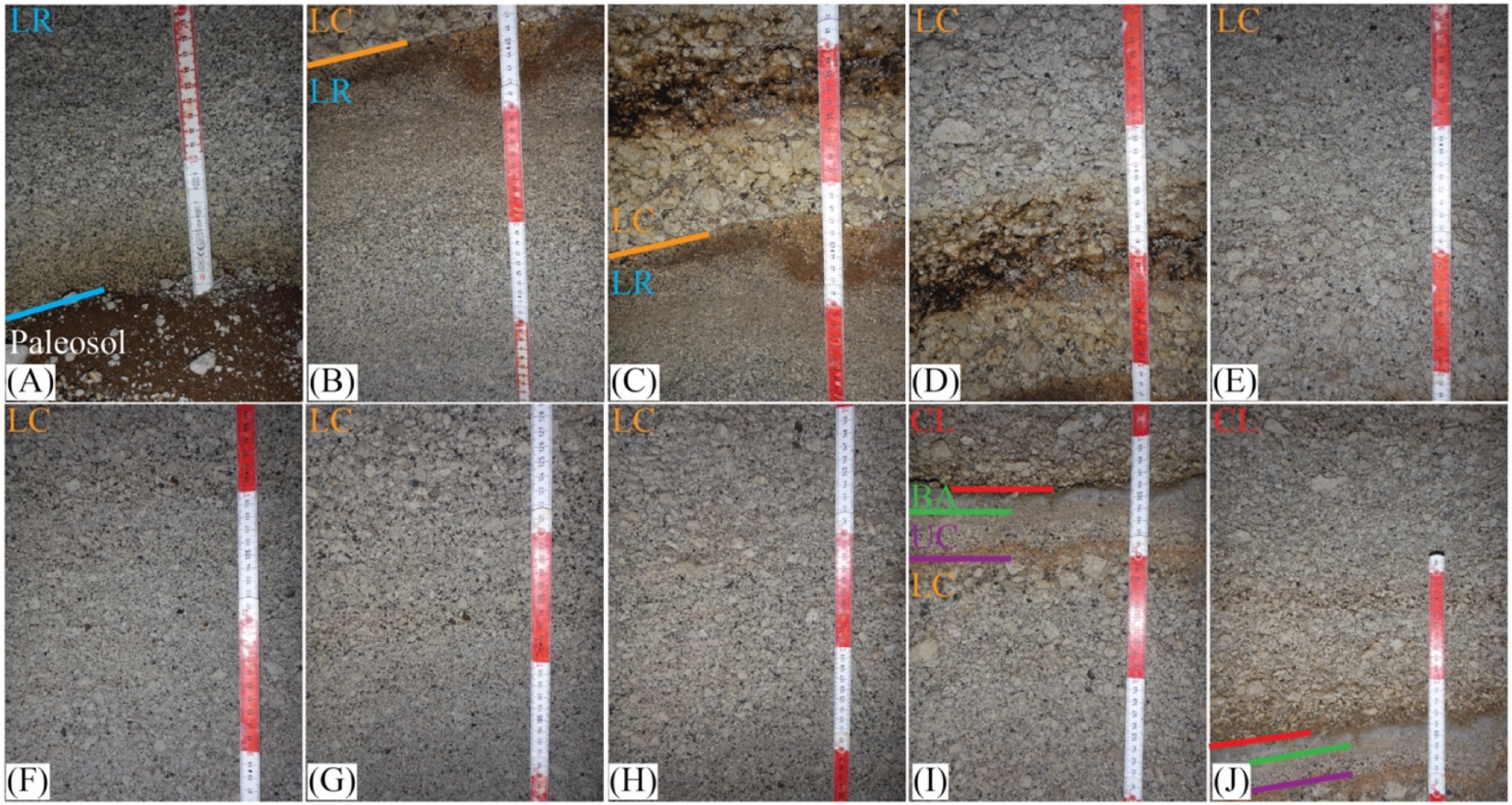

Appendix Figure 1. (A-J) Stratigraphic sequence of Llao Rock (LR), Lower Cleetwood (LC), Upper Cleetwood (UC), Basal Ash (BA) and Climactic (CL) as seen at Cltwd 02. Note in photos C and D the band of charcoal coated pumice.

Appendix Table 1. Best fitting parameters and erupted volumes obtained using *TephraFits* (Biass et al., 2019) for the lower Cleetwood unit.

	Models	**Lower Cleetwood**
Best fit	Exponential Volume (km^3)	0.83 (r^2 = 0.99)
	Power-law Volume (km^3)	0.75 (r^2 = 0.85)
	Weibull Volume (km^3)	0.86 (r^2 = 0.99)
	k_1	-0.0935
	k_2	-0.1373
	$T0_1$	426.06
	$T0_2$	1.15E+03
	m	3.1712
	CPl	7.57E+05
	Θ	203.92
	λ	18.52
	n	1.63

Appendix Table 2. Full Tephra2 grid search results.

	Wind	Plume height (masl)	Alpha	Beta	Diffusion coefficient (m^2/s)	Fall time threshold (s)	RMSE ML	RMSE GSD
BEST RMSE ML	2020_02_27_00UTC	18500	5	2.9	1668	4642	85.68	9.78
	2002_10_28_06UTC	12000	3	1	2154	21544	89.41	9.61
	2021_02_17_00UTC	12000	8	2	5995	1000	90.68	8.83
	1986_11_30_12UTC	24000	10	8	2154	10000	90.81	9.18
	2020_03_03_06UTC	14000	3	1	2154	4642	91.22	9.00
	2015_07_17_00UTC	16000	9	1	2154	10000	91.47	13.38
	1984_01_24_12UTC	10000	6	1	16681	1000	92.26	10.64
	2014_12_22_12UTC	30000	0.8	2	16681	1000	92.38	5.79
	1997_10_26_00UTC	30000	8	7	774	10000	92.75	12.26
	1983_12_16_00UTC	12000	6	2	5995	1000	93.48	8.21
	2011_11_16_00UTC	10000	7	1	5995	1000	94.31	10.21
	1989_11_07_18UTC	12000	10	3	16681	1000	94.80	9.48
	1981_10_25_12UTC	20000	7	7	2154	21544	95.77	7.40
	2004_01_05_06UTC	10000	6	1	5995	1000	96.74	9.20
	2002_03_28_06UTC	12000	7	3	16681	1000	98.43	8.46
	2007_02_17_00UTC	15000	9	5	5995	1000	98.54	7.96
	2021_04_19_06UTC	14000	9	3	2154	4642	100.44	11.30
	1990_11_03_18UTC	30000	6	10	2154	10000	103.33	7.80
	2011_10_30_00UTC	18000	3	1	2154	46416	103.51	9.94
	2015_09_07_06UTC	15000	7	2	774	21544	106.25	13.04
	1983_12_20_00UTC	12000	5	2	16681	1000	106.48	8.38
	1983_12_21_12UTC	14000	4	1	5995	1000	106.60	9.26
	2021_12_05_18UTC	26000	1	1	2154	1000	110.73	7.75
	1990_12_02_18UTC	14000	10	8	16681	1000	110.90	7.81
	1997_02_15_00UTC	12000	0.2	0.8	16681	1000	118.01	13.09
	2000_09_11_06UTC	14000	10	2	2154	10000	118.88	12.41
	2012_11_04_18UTC	30000	4	5	2154	10000	121.27	8.71
	1994_04_15_06UTC	18000	9	5	5995	1000	121.69	8.30
	2009_10_26_00UTC	14000	8	2	16681	1000	126.94	8.39
	2016_03_16_00UTC	10000	6	1	16681	1000	129.24	10.31
	2002_01_13_06UTC	21000	0.6	0.8	100	1000	129.70	12.89
	1985_03_30_12UTC	30000	6	10	16681	1000	136.16	8.27
	1996_04_29_00UTC	22000	10	10	5995	1000	141.00	7.17
	2019_04_17_12UTC	14000	6	2	16681	1000	142.64	8.47

	1996_01_04_18UTC	16000	10	10	16681	1000	146.54	7.67
	2021_02_07_18UTC	30000	0.6	1	16681	1000	153.97	9.02
	2014_11_25_06UTC	30000	0.6	1	16681	1000	157.08	8.87
	2007_03_01_12UTC	30000	6	0.4	2154	10000	159.62	12.95
	1994_02_23_00UTC	28000	0.8	1	16681	1000	170.07	8.98
	1985_11_01_18UTC	30000	0.6	1	16681	1000	181.93	8.61
	1991_11_05_00UTC	30000	0.8	1	16681	1000	186.06	8.84
Best RMSE GSD	2014_12_22_12UTC	27000	1	5	129155	4642	224.13	1.42
	2020_03_03_06UTC	10000	0.6	0.8	359381	10000	259.22	1.43
	1990_12_02_18UTC	16000	4	5	359381	4642	256.39	1.43
	1996_01_04_18UTC	16000	4	5	359381	4642	257.20	1.43
	2021_02_07_18UTC	24000	3	9	359381	4642	254.85	1.44
	2002_03_28_06UTC	20000	5	9	359381	4642	256.56	1.44
	1983_12_16_00UTC	10000	10	1	359381	100000	257.05	1.44
	2016_03_16_00UTC	18000	5	8	359381	4642	257.14	1.44
	1991_11_05_00UTC	14000	4	3	359381	4642	259.22	1.44
	2019_04_17_12UTC	10000	0.2	0.8	359381	100000	258.56	1.44
	1985_03_30_12UTC	10000	0.2	0.8	359381	100000	258.34	1.44
	1997_02_15_00UTC	12000	2	1	359381	4642	257.47	1.44
	2004_01_05_06UTC	20000	5	10	359381	10000	257.03	1.44
	2007_03_01_12UTC	16000	4	4	359381	4642	258.70	1.44
	1984_01_24_12UTC	12000	7	3	359381	100000	256.48	1.44
	1981_10_25_12UTC	10000	1	0.8	359381	10000	260.06	1.44
	1989_11_07_18UTC	18000	5	7	359381	10000	257.72	1.44
	1983_12_20_00UTC	12000	10	4	359381	10000	257.01	1.44
	2021_04_19_06UTC	10000	3	0.8	359381	100000	260.51	1.44
	1985_11_01_18UTC	12000	8	3	359381	100000	258.09	1.45
	1994_02_23_00UTC	16000	4	5	359381	100000	257.77	1.45
	2014_11_25_06UTC	14000	8	6	359381	4642	256.80	1.45
	2002_01_13_06UTC	12000	10	4	359381	100000	257.73	1.45
	1994_04_15_06UTC	12000	10	2	359381	10000	260.74	1.45
	2021_12_05_18UTC	12000	4	2	359381	21544	256.59	1.45
	2009_10_26_00UTC	10000	2	0.8	359381	100000	260.53	1.45
	1983_12_21_12UTC	10000	0.8	0.8	359381	10000	260.01	1.45
	2011_11_16_00UTC	10000	8	1	359381	46416	256.86	1.45
	2002_10_28_06UTC	16000	6	6	359381	100000	258.41	1.45
	2007_02_17_00UTC	15000	6	5	359381	100000	258.35	1.46
	2021_02_17_00UTC	20000	5	8	359381	10000	258.44	1.46

	1990_11_03_18UTC	12000	5	1	359381	10000	261.16	1.46
	2000_09_11_06UTC	12000	5	1	359381	46416	261.19	1.46
	1996_04_29_00UTC	12000	8	2	359381	10000	261.39	1.47
	2015_09_07_06UTC	12000	6	1	359381	10000	262.01	1.48
	2015_07_17_00UTC	12000	7	1	359381	10000	262.66	1.48
	2011_10_30_00UTC	12000	7	1	359381	10000	262.79	1.49
	2012_11_04_18UTC	12000	7	1	359381	10000	262.20	1.49
	1986_11_30_12UTC	14000	8	3	359381	21544	262.98	1.50
	1997_10_26_00UTC	12000	10	1	359381	100000	264.24	1.51
	2020_02_27_00UTC	19500	2	3.3	10000	4642	275.77	6.89

REFERENCES CITED

Chapter II

Alfano, F., Bonadonna, C., Volentik, A., Connor, C. B., Watt, S. F. L., Pyle, D. M., & Connor, L. J. (2011). Tephra stratigraphy and eruptive volume of the May, 2008, Chaitén eruption, Chile. *Bulletin of Volcanology*, *73*(5), 613–630.

Alfano, F., Bonadonna, C., Watt, S., Connor, C., Volentik, A., & Pyle, D. M. (2016). Reconstruction of total grain size distribution of the climactic phase of a long-lasting eruption: the example of the 2008–2013 Chaitén eruption. *Bulletin of Volcanology*, *78*(7), 1–21.

Bacon, C. R. (1983). Eruptive history of Mount Mazama and Crater Lake Caldera, Cascade Range, U.S.A. *Journal of Volcanology and Geothermal Research*, *18*(1–4), 57–115. https://doi.org/10.1016/0377-0273(83)90004-5

Bacon, C. R., Gardner, J. V., Mayer, L. A., Buktenica, M. W., Dartnell, P., Ramsey, D. W., & Robinson, J. E. (2002). Morphology, volcanism, and mass wasting in Crater Lake, Oregon. *Bulletin of the Geological Society of America*, *114*(6), 675–692. https://doi.org/10.1130/0016-7606(2002)114<0675:MVAMWI>2.0.CO;2

Bacon, C. R., & Lanphere, M. A. (2006). Eruptive history and geochronology of Mount Mazama and the Crater Lake region, Oregon. *Bulletin of the Geological Society of America*, *118*(11–12), 1331–1359. https://doi.org/10.1130/B25906.1

Bertin, D., Lara, L. E., Basualto, D., Amigo, Á., Cardona, C., Franco, L., … Lazo, J. (2015). High effusion rates of the Cordón Caulle 2011–2012 eruption (Southern Andes) and their relation with the quasi-harmonic tremor. *Geophysical Research Letters*, *42*(17), 7054–7063.

Biass, S., Bonadonna, C., & Houghton, B. F. (2019). A step-by-step evaluation of empirical methods to quantify eruption source parameters from tephra-fall deposits. *Journal of Applied Volcanology*, *8*(1), 1. https://doi.org/10.1186/s13617-018-0081-1

Biasse, S., Bagheri, G., Aeberhard, W., & Bonadonna, C. (2014). TError: towards a better quantification of the uncertainty propagated during the characterization of tephra deposits. *Statistics in Volcanology*, *1*(2), 1–27.

Blott, S. J., & Pye, K. (2006). Particle size distribution analysis of sand-sized particles by laser diffraction: An experimental investigation of instrument sensitivity and the effects of particle shape. *Sedimentology*, *53*(3), 671–685. https://doi.org/10.1111/j.1365-3091.2006.00786.x

Bonadonna, C., Connor, C. B., Houghton, B. F., Connor, L., Byrne, M., Laing, A., & Hincks, T. K. (2005). Probabilistic modeling of tephra dispersal: Hazard assessment of a multiphase rhyolitic eruption at Tarawera, New Zealand. *Journal of Geophysical Research: Solid Earth*, *110*(B3). https://doi.org/https://doi.org/10.1029/2003JB002896

Bonadonna, C., & Houghton, B. F. (2005). Total grain-size distribution and volume of tephra-fall deposits. *Bulletin of Volcanology*, *67*(5), 441–456. https://doi.org/10.1007/s00445-004-0386-2

Bonadonna, C., & Costa, A. (2012). Estimating the volume of tephra deposits: A new simple strategy. *Geology*, *40*(5), 415–418. https://doi.org/10.1130/G32769.1

Bonadonna, C., Cioni, R., Pistolesi, M., Elissondo, M., & Baumann, V. (2015). Sedimentation of long-lasting wind-affected volcanic plumes: the example of the 2011 rhyolitic Cordón Caulle eruption, Chile. *Bulletin of Volcanology*, *77*(2), 1–19.

Bonadonna, C., & Costa, A. (2013). Plume height, volume, and classification of explosive volcanic eruptions based on the Weibull function. *Bulletin of Volcanology*, *75*(8), 1–19. https://doi.org/10.1007/s00445-013-0742-1

Bonadonna, C., & Phillips, J. C. (2003). Sedimentation from strong volcanic plumes. *Journal of Geophysical Research: Solid Earth*, *108*(B7).

Bourgeois, R. L. (1998). *Physical characteristics of proximal Cleetwood airfall Deposits, Crater Lake, OR: The transition from explosive to effusive eruption*. University of Oregon.

Buckland, H. M., Cashman, K. V, Engwell, S. L., & Rust, A. C. (2020). Sources of uncertainty in the Mazama isopachs and the implications for interpreting distal tephra deposits from large magnitude eruptions. *Bulletin of Volcanology*, *82*(3), 23. https://doi.org/10.1007/s00445-020-1362-1

Buckland, H. M., Saxby, J., Roche, M., Meredith, P., Rust, A. C., Cashman, K. V, & Engwell, S. L. (2021). Measuring the size of non-spherical particles and the implications for grain size analysis in volcanology. *Journal of Volcanology and Geothermal Research*, *415*, 107257. https://doi.org/https://doi.org/10.1016/j.jvolgeores.2021.107257

Carazzo, G., Tait, S., Michaud-Dubuy, A., Fries, A., & Kaminski, E. (2020). Transition from stable column to partial collapse during the 79 cal CE P3 Plinian eruption of Mt. Pelée volcano (Lesser Antilles). *Journal of Volcanology and Geothermal Research*, *392*, 106764. https://doi.org/https://doi.org/10.1016/j.jvolgeores.2019.106764

Carey, S. N., & Sigurdsson, H. (1982). Influence of particle aggregation on deposition of distal tephra from the MAy 18, 1980, eruption of Mount St. Helens volcano. *Journal of Geophysical Research: Solid Earth*, *87*(B8), 7061–7072. https://doi.org/https://doi.org/10.1029/JB087iB08p07061

Carey, S., & Sigurdsson, H. (1989). The intensity of plinian eruptions. *Bulletin of Volcanology*, *51*(1), 28–40. https://doi.org/10.1007/BF01086759

Carey, S., & Sparks, R. S. J. (1986). Quantitative models of the fallout and dispersal of tephra from volcanic eruption columns. *Bulletin of Volcanology*, *48*(2), 109–125.

Carn, S. A., Pallister, J. S., Lara, L., Ewert, J. W., Watt, S., Prata, A. J., … Villarosa, G. (2009). The unexpected awakening of Chaitén volcano, Chile. *Eos, Transactions American Geophysical Union*, *90*(24), 205–206.

Castro, J. M., Schipper, C. I., Mueller, S. P., Militzer, A. S., Amigo, A., Parejas, C. S., & Jacob, D. (2013). Storage and eruption of near-liquidus rhyolite magma at Cordón Caulle, Chile. *Bulletin of Volcanology*, *75*(4), 1–17.

Choumert-Nkolo, J., Lamour, A., & Phélinas, P. (2021). The Economics of Volcanoes. *Economics of Disasters and Climate Change*, *5*(2), 277–299. https://doi.org/10.1007/s41885-021-00087-2

Costa, A., Pioli, L., & Bonadonna, C. (2016). Assessing tephra total grain-size distribution: Insights from field data analysis. *Earth and Planetary Science Letters*, *443*, 90–107. https://doi.org/https://doi.org/10.1016/j.epsl.2016.02.040

Dufek, J., & Manga, M. (2008). In situ production of ash in pyroclastic flows. *Journal of Geophysical Research: Solid Earth*, *113*(B9). https://doi.org/https://doi.org/10.1029/2007JB005555

Dufek, J., Manga, M., & Patel, A. (2012). Granular disruption during explosive volcanic eruptions. *Nature Geoscience*, *5*(8), 561–564. https://doi.org/10.1038/ngeo1524

Durant, A. J., Villarosa, G., Rose, W. I., Delmelle, P., Prata, A. J., & Viramonte, J. G. (2012). Long-range volcanic ash transport and fallout during the 2008 eruption of Chaitén volcano, Chile. *Physics and Chemistry of the Earth, Parts A/B/C*, *45*, 50–64.

Egan, J., Staff, R., & Blackford, J. (2015). A high-precision age estimate of the Holocene Plinian eruption of Mount Mazama, Oregon, USA. *Holocene*, *25*(7), 1054–1067. https://doi.org/10.1177/0959683615576230

Engwell, S. L., Sparks, R. S. J., & Aspinall, W. P. (2013). Quantifying uncertainties in the measurement of tephra fall thickness. *Journal of Applied Volcanology*, *2*(1), 1–12.

Fierstein, J., & Nathenson, M. (1992). Another look at the calculation of fallout tephra volumes. *Bulletin of Volcanology*, *54*(2), 156–167.

Folch, A., Mingari, L., Gutierrez, N., Hanzich, M., Macedonio, G., & Costa, A. (2020). FALL3D-8.0: a computational model for atmospheric transport and deposition of particles, aerosols and radionuclides–Part 1: Model physics and numerics. *Geoscientific Model Development*, *13*(3), 1431–1458.

Gardner, J. E., Llewellin, E. W., Watkins, J. M., & Befus, K. S. (2017). Formation of obsidian pyroclasts by sintering of ash particles in the volcanic conduit. *Earth and Planetary Science Letters*, *459*, 252–263. https://doi.org/https://doi.org/10.1016/j.epsl.2016.11.037

Gardner, J. E., Thomas, R. M. E., Jaupart, C., & Tait, S. (1996). Fragmentation of magma during Plinian volcanic eruptions. *Bulletin of Volcanology*, *58*(2), 144–162. https://doi.org/10.1007/s004450050132

Giachetti, T., Trafton, K. R., Wiejaczka, J., Gardner, J. E., Watkins, J. M., Shea, T., & Wright, H. M. N. (2021). The products of primary magma fragmentation finally revealed by pumice agglomerates. *Geology*, *49*(11), 1307–1311. https://doi.org/10.1130/G48902.1

Harris, D. M., & Rose Jr., W. I. (1983). Estimating particle sizes, concentrations, and total mass of ash in volcanic clouds using weather radar. *Journal of Geophysical Research: Oceans*, *88*(C15), 10969–10983. https://doi.org/https://doi.org/10.1029/JC088iC15p10969

Heiken, G. (1978). Plinian-type eruptions in the medicine lake highland, california, and the nature of the underlying magma. *Journal of Volcanology and Geothermal Research*, *4*(3), 375–402. https://doi.org/https://doi.org/10.1016/0377-0273(78)90023-9

Jay, J., Costa, F., Pritchard, M., Lara, L., Singer, B., & Herrin, J. (2014). Locating magma reservoirs using InSAR and petrology before and during the 2011–2012 Cordón Caulle silicic eruption. *Earth and Planetary Science Letters*, *395*, 254–266.

Jones, A., Thomson, D., Hort, M., & Devenish, B. (2007). *The U.K. Met Office's Next-Generation Atmospheric Dispersion Model, NAME III BT - Air Pollution Modeling and Its Application XVII* (C. Borrego & A.-L. Norman, Eds.). Boston, MA: Springer US.

Jones, T. J., & Russell, J. K. (2017). Ash production by attrition in volcanic conduits and plumes. *Scientific Reports*, *7*(1), 5538. https://doi.org/10.1038/s41598-017-05450-6

Kamata, H., Suzuki-Kamata, K., & Bacon, C. R. (1993). Deformation of the Wineglass Welded Tuff and the timing of caldera collapse at Crater Lake, Oregon. *Journal of Volcanology and Geothermal Research*, *56*(3), 253–265. https://doi.org/10.1016/0377-0273(93)90019-N

Kaminski, E., & Jaupart, C. (1998). The size distribution of pyroclasts and the fragmentation sequence in explosive volcanic eruptions. *Journal of Geophysical Research: Solid Earth*, *103*(B12), 29759–29779. https://doi.org/https://doi.org/10.1029/98JB02795

Kanamitsu, M., Ebisuzaki, W., Woollen, J., Yang, S.-K., Hnilo, J. J., Fiorino, M., & Potter, G. L. (2002). NCEP–DOE AMIP-II Reanalysis (R-2). *Bulletin of the American Meteorological Society*, *83*(11), 1631–1644. https://doi.org/10.1175/BAMS-83-11-1631

Klawonn, M., Houghton, B. F., Swanson, D. A., Fagents, S. A., Wessel, P., & Wolfe, C. J. (2014). Constraining explosive volcanism: subjective choices during estimates of eruption magnitude. *Bulletin of Volcanology*, *76*(2), 1–6.

Klawonn, M., Houghton, B. F., Swanson, D. A., Fagents, S. A., Wessel, P., & Wolfe, C. J. (2014). From field data to volumes: constraining uncertainties in pyroclastic eruption parameters. *Bulletin of Volcanology*, *76*(7), 1–16.

Kueppers, U., Perugini, D., & Dingwell, D. B. (2006). "Explosive energy" during volcanic eruptions from fractal analysis of pyroclasts. *Earth and Planetary Science Letters*, *248*(3–4), 800–807. https://doi.org/10.1016/j.epsl.2006.06.033

Kueppers, U., Putz, C., Spieler, O., & Dingwell, D. B. (2012). Abrasion in pyroclastic density currents: Insights from tumbling experiments. *Physics and Chemistry of the Earth, Parts A/B/C*, *45–46*, 33–39. https://doi.org/https://doi.org/10.1016/j.pce.2011.09.002

Le Pennec, J.-L., Ruiz, G. A., Ramón, P., Palacios, E., Mothes, P., & Yepes, H. (2012). Impact of tephra falls on Andean communities: The influences of eruption size and weather conditions during the 1999–2001 activity of Tungurahua volcano, Ecuador. *Journal of Volcanology and Geothermal Research*, *217*, 91–103.

Liu, E. J., Cashman, K. V, & Rust, A. C. (2015). Optimising shape analysis to quantify volcanic ash morphology. *GeoResJ*, *8*, 14–30. https://doi.org/https://doi.org/10.1016/j.grj.2015.09.001

Mastin, L. G. (2014). Testing the accuracy of a 1-D volcanic plume model in estimating mass eruption rate. *Journal of Geophysical Research: Atmospheres*, *119*(5), 2474–2495. https://doi.org/https://doi.org/10.1002/2013JD020604

McCormick, M. P., Thomason, L. W., & Trepte, C. R. (1995). Atmospheric effects of the Mt Pinatubo eruption. *Nature*, *373*(6513), 399–404. https://doi.org/10.1038/373399a0

Mele, D., Costa, A., Dellino, P., Sulpizio, R., Dioguardi, F., Isaia, R., & Macedonio, G. (2020). Total grain size distribution of components of fallout deposits and implications for magma fragmentation mechanisms: examples from Campi Flegrei caldera (Italy). *Bulletin of Volcanology*, *82*(4), 31. https://doi.org/10.1007/s00445-020-1368-8

Murrow, P. J., Rose Jr., W. I., & Self, S. (1980). Determination of the total grain size distribution in a Vulcanian eruption column, and its implications to stratospheric aerosol perturbation. *Geophysical Research Letters*, *7*(11), 893–896. https://doi.org/https://doi.org/10.1029/GL007i011p00893

Pallister, J. S., Diefenbach, A. K., Burton, W. C., Muñoz, J., Griswold, J. P., Lara, L. E., … Valenzuela, C. E. (2013). The Chaitén rhyolite lava dome: Eruption sequence, lava dome volumes, rapid effusion rates and source of the rhyolite magma. *Andean Geology*, *40*(2), 277–294.

Perugini, D., & Kueppers, U. (2012). Fractal analysis of experimentally generated pyroclasts: A tool for volcanic hazard assessment. *Acta Geophysica*, *60*(3), 682–698. https://doi.org/10.2478/s11600-012-0019-7

Pioli, L., Bonadonna, C., & Pistolesi, M. (2019). Reliability of Total Grain-Size Distribution of Tephra Deposits. *Scientific Reports*, *9*(1), 1–15. https://doi.org/10.1038/s41598-019-46125-8

Pistolesi, M., Cioni, R., Bonadonna, C., Elissondo, M., Baumann, V., Bertagnini, A., … Francalanci, L. (2015). Complex dynamics of small-moderate volcanic events: the example of the 2011 rhyolitic Cordón Caulle eruption, Chile. *Bulletin of Volcanology*, *77*(1), 1–24.

Pyle, D. M. (1989). The thickness, volume and grainsize of tephra fall deposits. *Bulletin of Volcanology*, *51*(1), 1–15. https://doi.org/10.1007/BF01086757

Riley, C. M., Rose, W. I., & Bluth, G. J. S. (2003). Quantitative shape measurements of distal volcanic ash. *Journal of Geophysical Research: Solid Earth*, *108*(B10). https://doi.org/https://doi.org/10.1029/2001JB000818

Robock, A. (2000). Volcanic eruptions and climate. *Reviews of Geophysics*, *38*(2), 191–219. https://doi.org/https://doi.org/10.1029/1998RG000054

Rose, W. I., & Durant, A. J. (2011). Fate of volcanic ash: Aggregation and fallout. *Geology*, *39*(9), 895–896. https://doi.org/10.1130/focus092011.1

Rosi, M., Vezzoli, L., Castelmenzano, A., & Grieco, G. (1999). Plinian pumice fall deposit of the Campanian Ignimbrite eruption (Phlegraean Fields, Italy). *Journal of Volcanology and Geothermal Research*, *91*(2), 179–198. https://doi.org/https://doi.org/10.1016/S0377-0273(99)00035-9

Rossi, E., Bagheri, G., Beckett, F., & Bonadonna, C. (2021). The fate of volcanic ash: premature or delayed sedimentation? *Nature Communications*, *12*(1), 1303. https://doi.org/10.1038/s41467-021-21568-8

Rossi, E., Bonadonna, C., & Degruyter, W. (2019). A new strategy for the estimation of plume height from clast dispersal in various atmospheric and eruptive conditions. *Earth and Planetary Science Letters*, *505*, 1–12. https://doi.org/10.1016/j.epsl.2018.10.007

Rust, A. C., & Cashman, K. V. (2011). Permeability controls on expansion and size distributions of pyroclasts. *Journal of Geophysical Research: Solid Earth*, *116*(B11). https://doi.org/https://doi.org/10.1029/2011JB008494

Saxby, J., Beckett, F., Cashman, K., Rust, A., & Tennant, E. (2018). The impact of particle shape on fall velocity: Implications for volcanic ash dispersion modelling. *Journal of Volcanology and Geothermal Research*, *362*, 32–48. https://doi.org/https://doi.org/10.1016/j.jvolgeores.2018.08.006

Saxby, J., Rust, A., Beckett, F., Cashman, K., & Rodger, H. (2020). Estimating the 3D shape of volcanic ash to better understand sedimentation processes and improve atmospheric dispersion modelling. *Earth and Planetary Science Letters*, *534*, 116075. https://doi.org/https://doi.org/10.1016/j.epsl.2020.116075

Schindelin, J., Arganda-Carreras, I., Frise, E., Kaynig, V., Longair, M., Pietzsch, T., … Cardona, A. (2012). Fiji: an open-source platform for biological-image analysis. *Nature Methods*, *9*(7), 676–682. https://doi.org/10.1038/nmeth.2019

Schipper, C. I., Castro, J. M., Tuffen, H., James, M. R., & How, P. (2013). Shallow vent architecture during hybrid explosive–effusive activity at Cordón Caulle (Chile, 2011–12): evidence from direct observations and pyroclast textures. *Journal of Volcanology and Geothermal Research*, *262*, 25–37.

Schwaiger, H. F., Denlinger, R. P., & Mastin, L. G. (2012). Ash3d: A finite-volume, conservative numerical model for ash transport and tephra deposition. *Journal of Geophysical Research: Solid Earth*, *117*(B4). https://doi.org/https://doi.org/10.1029/2011JB008968

Sigl, M., Winstrup, M., McConnell, J. R., Welten, K. C., Plunkett, G., Ludlow, F., … Woodruff, T. E. (2015). Timing and climate forcing of volcanic eruptions for the past 2,500 years. *Nature*, *523*(7562), 543–549. https://doi.org/10.1038/nature14565

Sparks, R. S. J., Wilson, L., Sigurdsson, H., & Walker, G. P. L. (1981). The pyroclastic deposits of the 1875 eruption of Askja, Iceland. *Philosophical Transactions of the Royal Society of London. Series A, Mathematical and Physical Sciences*, *299*(1447), 241–273. https://doi.org/10.1098/rsta.1981.0023

Tozer, B., Sandwell, D. T., Smith, W. H. F., Olson, C., Beale, J. R., & Wessel, P. (2019). Global Bathymetry and Topography at 15 Arc Sec: SRTM15+. *Earth and Space Science*, *6*(10), 1847–1864. https://doi.org/https://doi.org/10.1029/2019EA000658

Trafton, K. R., & Giachetti, T. (2021). The morphology and texture of Plinian pyroclasts reflect their lateral sourcing in the conduit. *Earth and Planetary Science Letters*, *562*, 116844. https://doi.org/https://doi.org/10.1016/j.epsl.2021.116844

Turcotte, D. L. (1992). Fractals, chaos, self-organized criticality and tectonics. *Terra Nova*, *4*(1), 4–12. https://doi.org/https://doi.org/10.1111/j.1365-3121.1992.tb00444.x

Turcotte, D. L. (1997). *Fractals and Chaos in Geology and Geophysics* (2nd ed.). https://doi.org/DOI: 10.1017/CBO9781139174695

Wadsworth, F. B., Vasseur, J., Schauroth, J., Llewellin, E. W., Dobson, K. J., Havard, T., … Heap, M. J. (2019). A general model for welding of ash particles in volcanic systems validated using in situ X-ray tomography. *Earth and Planetary Science Letters*, *525*, 115726. https://doi.org/https://doi.org/10.1016/j.epsl.2019.115726

Walker, G. P. L. (1980). The Taupo pumice: Product of the most powerful known (ultraplinian) eruption? *Journal of Volcanology and Geothermal Research*, *8*(1), 69–94. https://doi.org/https://doi.org/10.1016/0377-0273(80)90008-6

Walker, G. P. L. (1981). The Waimihia and Hatepe plinian deposits from the rhyolitic Taupo Volcanic Centre. *New Zealand Journal of Geology and Geophysics*, *24*(3), 305–324. https://doi.org/10.1080/00288306.1981.10422722

Walker, G. P. L. (1981). Characteristics of two phreatoplinian ashes, and their water-flushed origin. *Journal of Volcanology and Geothermal Research*, *9*(4), 395–407. https://doi.org/https://doi.org/10.1016/0377-0273(81)90046-9

Watkins, J. M., Gardner, J. E., & Befus, K. S. (2017). Nonequilibrium degassing, regassing, and vapor fluxing in magmatic feeder systems. *Geology*, *45*(2), 183–186. https://doi.org/10.1130/G38501.1

Watt, S. F. L., Pyle, D. M., Mather, T. A., Martin, R. S., & Matthews, N. E. (2009). Fallout and distribution of volcanic ash over Argentina following the May 2008 explosive eruption of Chaitén, Chile. *Journal of Geophysical Research: Solid Earth*, *114*(B4).

Wearn, K. M. (2002). *Pyroclastic obsidian from the Cleetwood and Rock Mesa eruptions, Central Oregon.* University of Oregon.

Wilson, L., Sparks, R. S. J., & Walker, G. P. L. (1980). Explosive volcanic eruptions — IV. The control of magma properties and conduit geometry on eruption column behaviour. *Geophysical Journal of the Royal Astronomical Society*, *63*(1), 117–148. https://doi.org/https://doi.org/10.1111/j.1365-246X.1980.tb02613.x

Young, S. R. (1990). *Physical volcanology of Holocene airfall deposits from Mt Mazama, Crater Lake, Oregon*. University of Lancaster.

Chapter III

Bacon, C. R. (1983). Eruptive history of Mount Mazama and Crater Lake Caldera, Cascade Range, U.S.A. *Journal of Volcanology and Geothermal Research*, *18*(1–4), 57–115. https://doi.org/10.1016/0377-0273(83)90004-5

Baines, P. G., & Sparks, R. S. J. (2005). Dynamics of giant volcanic ash clouds from supervolcanic eruptions. *Geophysical Research Letters*, *32*(24).

Baxter, P. J. (2005). Human impacts of volcanoes. *Volcanoes and the Environment*, 273-303.

Biass, S., Bonadonna, C., Connor, L., & Connor, C. (2016). TephraProb: a Matlab package for probabilistic hazard assessments of tephra fallout. *Journal of Applied Volcanology*, *5*(1), 1-16.

Biass, S., Bonadonna, C., & Houghton, B. F. (2019). A step-by-step evaluation of empirical methods to quantify eruption source parameters from tephra-fall deposits. *Journal of Applied Volcanology*, *8*(1), 1. https://doi.org/10.1186/s13617-018-0081-1

Blong, R. J. (1984). *Volcanic hazards: a sourcebook on the effects of eruptions*. Elsevier.

Blott, S. J., & Pye, K. (2006). Particle size distribution analysis of sand-sized particles by laser diffraction: An experimental investigation of instrument sensitivity and the effects of particle shape. *Sedimentology*, *53*(3), 671–685. https://doi.org/10.1111/j.1365-3091.2006.00786.x

Bonadonna, C., Ernst, G. G. J., & Sparks, R. S. J. (1998). Thickness variations and volume estimates of tephra fall deposits: the importance of particle Reynolds number. *Journal of Volcanology and Geothermal Research*, *81*(3-4), 173-187.

Bonadonna, C., & Phillips, J. C. (2003). Sedimentation from strong volcanic plumes. *Journal of Geophysical Research: Solid Earth*, *108*(B7).

Bonadonna, C., & Houghton, B. F. (2005). Total grain-size distribution and volume of tephra-fall deposits. *Bulletin of Volcanology*, *67*(5), 441–456. https://doi.org/10.1007/s00445-004-0386-2

Bonadonna, C., Connor, C. B., Houghton, B. F., Connor, L., Byrne, M., Laing, A., & Hincks, T. K. (2005). Probabilistic modeling of tephra dispersal: Hazard assessment of a multiphase rhyolitic eruption at Tarawera, New Zealand. *Journal of Geophysical Research: Solid Earth*, *110*(B3). https://doi.org/https://doi.org/10.1029/2003JB002896

Bonadonna, C., Connor, L., Connor, C. B., & Courtland, L. M. (2010). Tephra2.

Bonadonna, C., Genco, R., Gouhier, M., Pistolesi, M., Cioni, R., Alfano, F., ... & Ripepe, M. (2011). Tephra sedimentation during the 2010 Eyjafjallajökull eruption (Iceland) from deposit, radar, and satellite observations. *Journal of Geophysical Research: Solid Earth*, *116*(B12).

Bonadonna, C., Folch, A., Loughlin, S., & Puempel, H. (2012). Future developments in modelling and monitoring of volcanic ash clouds: outcomes from the first IAVCEI-WMO workshop on Ash Dispersal Forecast and Civil Aviation. *Bulletin of volcanology*, *74*, 1-10.

Brown, R. J., Bonadonna, C., & Durant, A. J. (2012). A review of volcanic ash aggregation. *Physics and Chemistry of the Earth, Parts a/b/c*, *45*, 65-78.

Buckland, H. M., Saxby, J., Roche, M., Meredith, P., Rust, A. C., Cashman, K. V, & Engwell, S. L. (2021). Measuring the size of non-spherical particles and the implications for grain size analysis in volcanology. *Journal of Volcanology and Geothermal Research*, *415*, 107257. https://doi.org/https://doi.org/10.1016/j.jvolgeores.2021.107257

Carey, S., & Sparks, R. S. J. (1986). Quantitative models of the fallout and dispersal of tephra from volcanic eruption columns. *Bulletin of Volcanology*, *48*(2), 109–125.

Castro, J. M., & Dingwell, D. B. (2009). Rapid ascent of rhyolitic magma at Chaitén volcano, Chile. *Nature*, *461*(7265), 780-783.

Connor, L. J., & Connor, C. B. (2006). Inversion is the key to dispersion: understanding eruption dynamics by inverting tephra fallout.

Constantinescu, R., Hopulele-Gligor, A., Connor, C. B., Bonadonna, C., Connor, L. J., Lindsay, J. M., ... & Volentik, A. C. (2021). The radius of the umbrella cloud helps characterize large explosive volcanic eruptions. *Communications Earth & Environment*, *2*(1), 3.

Costa, A., Pioli, L., & Bonadonna, C. (2016). Assessing tephra total grain-size distribution: Insights from field data analysis. *Earth and Planetary Science Letters*, *443*, 90–107. https://doi.org/https://doi.org/10.1016/j.epsl.2016.02.040

Draxler, R. R., & Hess, G. D. (1998). An overview of the HYSPLIT_4 modelling system for trajectories. *Australian meteorological magazine*, *47*(4), 295-308.

Elissondo, M., Baumann, V., Bonadonna, C., Pistolesi, M., Cioni, R., Bertagnini, A., ... & Gonzalez, R. (2016). Chronology and impact of the 2011 Cordón Caulle eruption, Chile. *Natural Hazards and Earth System Sciences*, *16*(3), 675-704.

Folch, A., Mingari, L., Gutierrez, N., Hanzich, M., Macedonio, G., & Costa, A. (2020). FALL3D-8.0: a computational model for atmospheric transport and deposition of particles, aerosols and radionuclides–Part 1: Model physics and numerics. *Geoscientific Model Development*, *13*(3), 1431–1458.

Freret-Lorgeril, V., Donnadieu, F., Eychenne, J., Soriaux, C., & Latchimy, T. (2019). In situ terminal settling velocity measurements at Stromboli volcano: Input from physical characterization of ash. *Journal of Volcanology and Geothermal Research*, *374*, 62-79.

Goode, L. R., Handley, H. K., Cronin, S. J., & Abdurrachman, M. (2019). Insights into eruption dynamics from the 2014 pyroclastic deposits of Kelut volcano, Java, Indonesia, and implications for future hazards. *Journal of Volcanology and Geothermal Research*, *382*, 6-23

Gouhier, M., & Donnadieu, F. (2008). Mass estimations of ejecta from Strombolian explosions by inversion of Doppler radar measurements. *Journal of Geophysical Research: Solid Earth*, *113*(B10).

Hargie, K. A., Van Eaton, A. R., Mastin, L. G., Holzworth, R. H., Ewert, J. W., & Pavolonis, M. (2019). Globally detected volcanic lightning and umbrella dynamics during the 2014 eruption of Kelud, Indonesia. *Journal of Volcanology and Geothermal Research*, *382*, 81-91.

Heiken, G. (1978). Plinian-type eruptions in the medicine lake highland, california, and the nature of the underlying magma. *Journal of Volcanology and Geothermal Research*, *4*(3), 375–402. https://doi.org/https://doi.org/10.1016/0377-0273(78)90023-9

Johnston, E. N., Phillips, J. C., Bonadonna, C., & Watson, I. M. (2012). Reconstructing the tephra dispersal pattern from the Bronze Age eruption of Santorini using an advection–diffusion model. *Bulletin of Volcanology*, *74*, 1485-1507.

Jones, A., Thomson, D., Hort, M., & Devenish, B. (2007). *The U.K. Met Office's Next-Generation Atmospheric Dispersion Model, NAME III BT - Air Pollution Modeling and Its Application XVII* (C. Borrego & A.-L. Norman, Eds.). Boston, MA: Springer US.

Kanamitsu, M., Ebisuzaki, W., Woollen, J., Yang, S.-K., Hnilo, J. J., Fiorino, M., & Potter, G. L. (2002). NCEP–DOE AMIP-II Reanalysis (R-2). *Bulletin of the American Meteorological Society*, *83*(11), 1631–1644. https://doi.org/10.1175/BAMS-83-11-1631

Kozono, T., Iguchi, M., Miwa, T., Maki, M., Maesaka, T., & Miki, D. (2019). Characteristics of tephra fall from eruptions at Sakurajima volcano, revealed by optical disdrometer measurements. *Bulletin of Volcanology*, *81*, 1-18.

Kristiansen, N. I., Prata, A. J., Stohl, A., & Carn, S. A. (2015). Stratospheric volcanic ash emissions from the 13 February 2014 Kelut eruption. *Geophysical Research Letters*, *42*(2), 588-596.

Kuehn, S. C. (2002). *Stratigraphy, distribution, and geochemistry of the Newberry Volcano tephras*. Washington State University.

Magill, C., Mannen, K., Connor, L., Bonadonna, C., & Connor, C. (2015). Simulating a multi-phase tephra fall event: inversion modelling for the 1707 Hoei eruption of Mount Fuji, Japan. *Bulletin of Volcanology*, *77*, 1-18.

Pioli, L., Bonadonna, C., & Pistolesi, M. (2019). Reliability of Total Grain-Size Distribution of Tephra Deposits. *Scientific Reports*, *9*(1), 1–15. https://doi.org/10.1038/s41598-019-46125-8

Pistolesi, M., Cioni, R., Bonadonna, C., Elissondo, M., Baumann, V., Bertagnini, A., … Francalanci, L. (2015). Complex dynamics of small-moderate volcanic events: the example of the 2011 rhyolitic Cordón Caulle eruption, Chile. *Bulletin of Volcanology*, *77*(1), 1–24.

Romero, J. E., Morgavi, D., Arzilli, F., Daga, R., Caselli, A., Reckziegel, F., ... & Perugini, D. (2016). Eruption dynamics of the 22–23 April 2015 Calbuco Volcano (Southern Chile): Analyses of tephra fall deposits. *Journal of Volcanology and Geothermal Research*, *317*, 15-29

Rose, W. I., & Durant, A. J. (2011). Fate of volcanic ash: Aggregation and fallout. *Geology*, *39*(9), 895-896.

Rossi, E., Bonadonna, C., & Degruyter, W. (2019). A new strategy for the estimation of plume height from clast dispersal in various atmospheric and eruptive conditions. *Earth and Planetary Science Letters*, *505*, 1–12. https://doi.org/10.1016/j.epsl.2018.10.007

Schindelin, J., Arganda-Carreras, I., Frise, E., Kaynig, V., Longair, M., Pietzsch, T., … Cardona, A. (2012). Fiji: an open-source platform for biological-image analysis. *Nature Methods*, *9*(7), 676–682. https://doi.org/10.1038/nmeth.2019

Schipper, C. I., Castro, J. M., Tuffen, H., James, M. R., & How, P. (2013). Shallow vent architecture during hybrid explosive–effusive activity at Cordón Caulle (Chile, 2011–12): evidence from direct observations and pyroclast textures. *Journal of Volcanology and Geothermal Research*, *262*, 25–37.

Schwaiger, H. F., Denlinger, R. P., & Mastin, L. G. (2012). Ash3d: A finite-volume, conservative numerical model for ash transport and tephra deposition. *Journal of Geophysical Research: Solid Earth*, *117*(B4). https://doi.org/https://doi.org/10.1029/2011JB008968

Scollo, S., Coltelli, M., Prodi, F., Folegani, M., & Natali, S. (2005). Terminal settling velocity measurements of volcanic ash during the 2002–2003 Etna eruption by an X-band microwave rain gauge disdrometer. *Geophysical Research Letters*, *32*(10).

Searcy, C., Dean, K., & Stringer, W. (1998). PUFF: A high-resolution volcanic ash tracking model. *Journal of Volcanology and Geothermal Research*, *80*(1-2), 1-16.

Sparks, R. S. J., Bursik, M. I., Ablay, G. J., Thomas, R. M. E., & Carey, S. N. (1992). Sedimentation of tephra by volcanic plumes. Part 2: controls on thickness and grain-size variations of tephra fall deposits. *Bulletin of Volcanology*, *54*, 685-695.

Sparks, R. S. J., Bursik, M. I., Carey, S. N., Gilbert, J., Glaze, L. S., Sigurdsson, H., & Woods, A. W. (1997). *Volcanic plumes*. Wiley.

Suzuki, T. (1983). A theoretical model for dispersion of tephra. *Arc volcanism: physics and tectonics*, *95*, 113.

Trafton, K. R., & Giachetti, T. (2022). The pivotal role of Vulcanian activity in ending the explosive phase of rhyolitic eruptions: the case of the Big Obsidian Flow eruption (Newberry Volcano, USA). *Bulletin of Volcanology*, *84*(12), 104.

Van Eaton, A. R., Amigo, Á., Bertin, D., Mastin, L. G., Giacosa, R. E., González, J., ... & Behnke, S. A. (2016). Volcanic lightning and plume behavior reveal evolving hazards during the April 2015 eruption of Calbuco volcano, Chile. *Geophysical Research Letters*, *43*(7), 3563-3571.

Volentik, A. C. M., Connor, C. B., Connor, L. J., & Bonadonna, C. (2009). Aspects of volcanic hazard assessment for the Bataan nuclear power plant, Luzon Peninsula, Philippines. *Volcanic and tectonic hazard assessment for nuclear facilities*, 229-256.

Volentik, A. C., Bonadonna, C., Connor, C. B., Connor, L. J., & Rosi, M. (2010). Modeling tephra dispersal in absence of wind: Insights from the climactic phase of the 2450 BP Plinian eruption of Pululagua volcano (Ecuador). *Journal of Volcanology and Geothermal Research*, *193*(1-2), 117-136.

Wiejaczka, J., & Giachetti, T. (2022). Using eruption source parameters and high-resolution grain-size distributions of the 7.7 ka Cleetwood Eruption of Mount Mazama (Oregon, United States) to reveal primary and secondary eruptive processes. *Frontiers in Earth Science*, 460.

Wilson, T. M., Stewart, C., Sword-Daniels, V., Leonard, G. S., Johnston, D. M., Cole, J. W., ... & Barnard, S. T. (2012). Volcanic ash impacts on critical infrastructure. *Physics and Chemistry of the Earth, Parts a/b/c*, *45*, 5-23.

Chapter IV

Adams, N. K., Houghton, B. F., Fagents, S. A., & Hildreth, W. (2006). The transition from explosive to effusive eruptive regime: the example of the 1912 Novarupta eruption, Alaska. *Geological Society of America Bulletin*, *118*(5–6), 620–634.

Bonadonna, C., Pistolesi, M., Cioni, R., Degruyter, W., Elissondo, M., & Baumann, V. (2015). Dynamics of wind-affected volcanic plumes: The example of the 2011 Cordón Caulle eruption, Chile. *Journal of Geophysical Research: Solid Earth*, *120*(4), 2242–2261.

Castro, J. M., & Gardner, J. E. (2008). Did magma ascent rate control the explosive-effusive transition at the Inyo volcanic chain, California? *Geology*, *36*(4), 279–282.

Castro, J. M., Bindeman, I. N., Tuffen, H., & Schipper, C. I. (2014). Explosive origin of silicic lava: textural and δD–H2O evidence for pyroclastic degassing during rhyolite effusion. *Earth and Planetary Science Letters*, *405*, 52–61.

Collini, E., Osores, M. S., Folch, A., Viramonte, J. G., Villarosa, G., & Salmuni, G. (2013). Volcanic ash forecast during the June 2011 Cordón Caulle eruption. *Natural Hazards*, *66*, 389–412.

Degruyter, W., Bachmann, O., Burgisser, A., & Manga, M. (2012). The effects of outgassing on the transition between effusive and explosive silicic eruptions. *Earth and Planetary Science Letters*, *349*, 161–170.

Eichelberger, J. C., & Westrich, H. R. (1981). Magmatic volatiles in explosive rhyolitic eruptions. *Geophysical Research Letters*, *8*(7), 757–760.

Eichelberger, J. C., Carrigan, C. R., Westrich, H. R., & Price, R. H. (1986). Non-explosive silicic volcanism. *Nature*, *323*(6089), 598–602.

Giachetti, T., Wiejaczka, J., Trafton, K. R., & Shea, T. Pulling the Plug: Do Silicic VEI 4-5 Eruptions Always Progress from Plinian to Vulcanian, and Finally to Effusive Activity? Poster presented at: the IAVCEI Scientific Assembly, February 2, 2023; Rotorua, New Zealand.

Heiken, G. (1978). Plinian-type eruptions in the Medicine Lake Highland, California, and the nature of the underlying magma. *Journal of Volcanology and Geothermal Research*, *4*(3–4), 375–402.

Kuehn, S. C. (2002). *Stratigraphy, distribution, and geochemistry of the Newberry Volcano tephras*. Washington State University.

Newman, S., Epstein, S., & Stolper, E. (1988). Water, carbon dioxide, and hydrogen isotopes in glasses from the ca. 1340 AD eruption of the Mono Craters, California: Constraints on degassing phenomena and initial volatile content. *Journal of Volcanology and Geothermal Research*, *35*(1–2), 75–96.

Pallister, J. S., Diefenbach, A. K., Burton, W. C., Muñoz, J., Griswold, J. P., Lara, L. E., Lowenstern, J. B., & Valenzuela, C. E. (2013). The Chaitén rhyolite lava dome: Eruption sequence, lava dome volumes, rapid effusion rates and source of the rhyolite magma. *Andean Geology*, *40*(2), 277–294.

Pistolesi, M., Cioni, R., Bonadonna, C., Elissondo, M., Baumann, V., Bertagnini, A., Chiari, L., Gonzales, R., Rosi, M., & Francalanci, L. (2015). Complex dynamics of small-moderate volcanic events: the example of the 2011 rhyolitic Cordón Caulle eruption, Chile. *Bulletin of Volcanology*, *77*, 1–24.

Schipper, C. I., Castro, J. M., Tuffen, H., James, M. R., & How, P. (2013). Shallow vent architecture during hybrid explosive–effusive activity at Cordón Caulle (Chile, 2011–12): evidence from direct observations and pyroclast textures. *Journal of Volcanology and Geothermal Research*, *262*, 25–37.

Silva Parejas, C., Lara, L. E., Bertin, D., Amigo, A., & Orozco, G. (n.d.). *The 2011-2012 eruption of Cordón Caulle volcano (Southern Andes): Evolution, crisis management and*.

Trafton, K. R., & Giachetti, T. (2022). The pivotal role of Vulcanian activity in ending the explosive phase of rhyolitic eruptions: the case of the Big Obsidian Flow eruption (Newberry Volcano, USA). *Bulletin of Volcanology*, *84*(12), 104.

Wadsworth, F. B., Llewellin, E. W., Castro, J. M., Tuffen, H., Schipper, C. I., Gardner, J. E., Vasseur, J., Foster, A., Damby, D. E., & McIntosh, I. M. (2022). A reappraisal of explosive–effusive silicic eruption dynamics: syn-eruptive assembly of lava from the products of cryptic fragmentation. *Journal of Volcanology and Geothermal Research*, *432*, 107672.

Wiejaczka, J., & Giachetti, T. (2022). Using eruption source parameters and high-resolution grain-size distributions of the 7.7 ka Cleetwood Eruption of Mount Mazama (Oregon, United States) to reveal primary and secondary eruptive processes. *Frontiers in Earth Science*, 460.